Andreia Cristina Jóia Araújo Cardoso

Mestre em Engenharia Física

Plasmonic Silver Nanoparticles by Dewetting process: Applications in SERS and Thin Film Solar Cells

Dissertação para obtenção do Grau de Doutor
em Nanotecnologias e Nanociências

Orientador: Doutor Rodrigo Ferrão de Paiva Martins, Professor Catedrático, Faculdade de Ciências e Tecnologia da Universidade Nova de Lisboa
Co-orientador: Doutor Hugo Manuel Brito Águas, Professor Auxiliar, Faculdade de Ciências e Tecnologia da Universidade Nova de Lisboa

Júri:
Presidente: Doutor José Julio Alferes
Vogais: Doutor Adélio Miguel Magalhães Mendes
Doutor Rodrigo Ferrão de Paiva Martins
Doutora Elvira Maria Correia Fortunato
Doutor Tito Da Silva Trindade
Doutora Eulália Fernanda Alves De Carvalho Pereira
Doutora Maria Goreti Ferreira Sales
Doutor Pedro Manuel Parracho Salomé
Doutor Manuel João De Moura Dias Mendes

FACULDADE DE
CIÊNCIAS E TECNOLOGIA
UNIVERSIDADE NOVA DE LISBOA

Março de 2018

Andreia Cristina Jóia Araújo Cardoso

Mestre em Engenharia Física

Plasmonic Silver Nanoparticles by Dewetting process: Applications in SERS and Thin Film Solar Cells

Dissertação para obtenção do Grau de Doutor
em Nanotecnologias e Nanociências

Orientador: Doutor Rodrigo Ferrão de Paiva Martins, Professor Catedrático, Faculdade de Ciências e Tecnologia da Universidade Nova de Lisboa
Co-orientador: Doutor Hugo Manuel Brito Águas, Professor Auxiliar, Faculdade de Ciências e Tecnologia da Universidade Nova de Lisboa

Júri:
Presidente: Doutor José Julio Alferes
Vogais: Doutor Adélio Miguel Magalhães Mendes
Doutor Rodrigo Ferrão de Paiva Martins
Doutora Elvira Maria Correia Fortunato
Doutor Tito Da Silva Trindade
Doutora Eulália Fernanda Alves De Carvalho Pereira
Doutora Maria Goreti Ferreira Sales
Doutor Pedro Manuel Parracho Salomé
Doutor Manuel João De Moura Dias Mendes

FACULDADE DE CIÊNCIAS E TECNOLOGIA
UNIVERSIDADE NOVA DE LISBOA

Março de 2018

Plasmonic Silver Nanoparticles by Dewetting process: Applications in SERS and Thin Film Solar Cells

Acknowledgements

People often say that scientific research is a lonely work but the way I see it, there are so many people around the laboratories that contributed to this work and to whom I want to thank to.

First I want to acknowledge my supervisors for their support, advice and guidance throughout this work. Their complementarity in scientific and teaching expertise and their shared enthusiasm for science contributed a lot to my professional and personal growth. Prof. Rodrigo Martins, for the opportunity to develop this work within the group, for his effort to provide all the necessary means for the success of this research investing in lab facilities and for helping me in all goals of this thesis. Thank you for the trust deposited in me and in my work. Dr. Hugo Águas, for his friendship, sharing information and kind observations along all these years. Thank you for believing in me and in my work. This work is also yours.

To Prof. Elvira Fortunato, for allowing the development of this work in the research facilities of CENIMAT/I3N and for all her help and friendship. Thank you for all the support you have given me writing scientific papers, I've learned a lot from you. Thank you for all the new equipment you have acquired for my PhD, they largely contributed for the results on this thesis.

To Dr. Manuel Mendes, for sharing his knowledge on plasmonics and metal nanoparticles. Thank you for the hours that we discuss the near and the far field. This work wouldn't be the same without you.

To MSc. Tiago Mateus, Dr. Ana Pimentel and Dr. Daniela Nunes friends and lab mates, group work makes a lot of difference, your contribution to this work was indispensable.

To former colleagues whose support and friendship surpassed distance; Dr. Raquel Barros, Dr. Lidia Santos, Dr. Sergej Filonovich and future Dr. Catarina Santos.

To all my colleagues in the MEON group that, direct or indirectly, contributed to this work: MSc. Diana Gaspar, Dr. António Vicente, MSc. João Costa, Dr. Bruno Viegas, MSc. Tomás Calmeiro, Dr. Joana Pinto, Dr. Pedro Barquinha, Dr. Luís Pereira, Dr. António Vicente, Dr. Rita Branquinho, MSc. Ana Rovisco, MSc. Jorge Martins, MSc. Ana Samouco, MSc. Maria Oliveira, MSc. Emanuel Carlos, MSc. Cristina Fernandes, Dr. Jonas Duermeier, Dr. Olalla Sanchez, Dr. Andrey Lyubchik, Prof. Rui Igreja and everybody else I don't have room to mention. Thank you all!

To Ricardo Ferreira for all the help in solving technical issues.

To Susana Mendes, Valéria Gomes, Sara Oliveira and Sónia Soares for their friendship and professionalism, making logistics a lot easier.

To Prof. Ricardo Franco for sharing his knowledge on SERS which was very helpful during this PhD.

To the Fundação para a Ciência e Tecnologia (FCT) for the fellowship and CENIMAT/ I3N- CEMOP/UNINOVA for the financial support for conferences attendance.

To all my friends for their comprehension and support. To MSc. Sónia Pereira, MSc. Alexandra Gonçalves, future Dr. Ana Marques, Dr. Daniela Nunes, Dr. Ana Pimentel (my scientific wedding) and future Dr. Daniela Salgueiro (you're up next!); companions during this years in the lab.

To my family: to my brothers Hélder, Sandra e José, my parents Antonieta e José and my nephews Nikole and Júnior, I wouldn't be who I am today without all of you. I want to thank my husband Bruno and my son James, thank you for all the patience and understanding my love for science.

I want to thank and dedicate this work to my brother Zézinho. I hope it to be worthy of the pride you had in me. Thank you for the strength that you gave me to write this thesis days after you left us. See you soon my love.

Finally, to all the people, I've mentioned here, thank you for all the love you gave me, because in the end, is what we take from this life.

Resumo

Em termos da exploração de materiais à nano escala, e sua integração em dispositivos optoelectrónicos, novas estratégias têm sido desenvolvidas na área da nanofotónica, baseadas em efeitos plasmónicos, consideradas como solução ideal para ultrapassar limitações importantes relacionadas com o desempenho dos dispositivos em diferentes tipos de aplicações. Os efeitos explorados ao longo deste trabalho estão relacionados com o aumento da eficiência de células solares de silício (Si) de filme fino e de sinais de Raman para deteção molecular, recorrendo à utilização de nanopartículas metálicas (MNP) de prata (Ag), que são as que proporcionam o melhor efeito plasmónico para estas aplicações (células solares e espectroscopia de Raman).

Na presente tese estes efeitos foram explorados recorrendo a filmes finos de Ag depositados utilizando a técnica de evaporação térmica assistida por feixe de eletrões. Os filmes foram depois sujeitos a um tratamento térmico de forma a induzir uma transformação morfológica - de filme fino (TF) para uma dispersão de nanopartículas (NPs), através do mecanismo de "solid-state dewetting" (SSD). Neste ponto, é apresentado um processo inovador que envolve apenas um passo na técnica de produção das nanoparticulas, sem que seja necessário tratamentos térmicos após a deposição. Este processo origina um rearranjo adequado das nanoparticulas que proporciona aumento do sinal Raman, sendo fácil o controlo do seu tamanho e forma. Relativamente às nanostruturas que necessitam de um tratamento térmico após deposição, estas foram essencialmente utilizadas em células solares para aprisionamento de luz (light traping). Neste caso, desenvolveu-se um processo de tratamento térmico rápido (RTA) que dá origem a superfícies plasmónicas uniformes, necessitando apenas de um tempo de tratamento térmico muito reduzido (<10 min), quando comparado com outros métodos convencionais (com tempos superiores a 1 h). Como resultado final, observou-se que células solares de silício microcristalino (μc-Si:H), produzidas sobre refletores à base de nanoparticulas de Ag com propriedades plasmonicas, e com diâmetros aproximados de 200 nm, apresentam um aumento de 11% na eficiência, correspondendo a uma densidade de corrente de 24.4 mA/cm^2 e uma eficiência de 6.78 %, que podem ser comparados com os valores de 21.79 mA/cm^2 e 6.12 % obtidos com uma estrutura de célula plana sem NPs. Para aplicações relacionadas com o aumento do sinal de Raman, obteve-se um aumento na ordem de 10^9 com a utilização de rhodamine 6G (10^{-8} M), que serve como analito de teste. Com este resultado, foi desenvolvido um novo substrato para SERS à base de celulose (papel) para ser utilizado em aplicações de baixo custo, descartáveis e flexíveis. Para além destas vantagens, estes substratos provaram também ser eficientes, estáveis e uniformes, quando utilizados em aplicações de SERS.

Palavras-chave: *plasmonica; nanoparticulas de prata; aprisionamento de luz em celulas solares de filme fino; SERS; solid-state dewetting; substratos à base de celulose.*

Abstract

The exploration of materials at the nanoscale, and their integration into optoelectronic devices, can be developed via new nanophotonic strategies based on plasmonic effects, which are nowadays regarded as the preferential solutions to overcome performance limitations in different types of applications. Those explored here concern the increase of efficiency of physically thin film silicon (Si) solar cells and of weak Raman signals for molecular detection (one scattered photon per million incident), employing metal nanoparticle (MNP) structures made of silver (Ag) which is the most effective material for plasmon-enhancement in solar cells and Raman Spectroscopy.

The present thesis explored these effects employing thermal evaporation assisted by electron beam (e-beam) to deposit uniform thin layers of Ag, which then underwent a thermally-induced morphology transformation from a thin film (TF) to an array of NPs by a solid-state dewetting (SSD) mechanism. A novel procedure, involving a one-step methodology, without any post-deposition thermal procedures, is presented. This resulted in the direct arrangement of individual nanoparticles suitable for Raman amplification, with good control of their size and shape. The nanostructures that require a post-annealing process were essentially used for light trapping in solar cells. In this case a rapid thermal annealing (RTA) method was developed that yields highly reproducible and uniform plasmonic surfaces within a very fast (<10 min) annealing time when compared to other commonly employed annealing processes (>1 hour).

The final results showed that microcrystalline silicon (μc-Si:H) solar cells deposited on improved ultra-fast plasmonics back reflectors (PBR), with Ag NPs with sizes of about 200 nm, exhibit an overall 11% improvement on device efficiency, corresponding to a photocurrent of 24.4 mA/cm^2 and an efficiency of 6.78 %; against 21.79 mA/cm^2 and 6.12 %, respectively, obtained on flat structures without NPs. For surface enhanced Raman spectroscopy (SERS) application, a remarkable 10^9 signal enhancement was obtained using rhodamine 6G (10^{-8} M) as the test analyte, and a new kind of cost-efficient SERS substrate (cardboard plates) was investigated for low-cost, flexible and disposable bio-detection devices. Besides such advantages, cardboard substrate proved to be a high-efficient, uniform and stable SERS substrate.

Keywords: *plasmonics; silver nanoparticles; light-trapping in thin film photovoltaics; SERS; solid-state dewetting; cellulose based substrates.*

Aim and outline of the thesis

The work presented in this thesis focuses mainly in the implementation of MNPs by dewetting processes for plasmon-enhancement in Si solar cells and Raman spectroscopy. The first part of the thesis focuses on the development of metallic nanostructures to achieve light trapping in thin Si photovoltaics (PV) cells, with the objective of reducing the absorber-layer thickness while improving cell performance.

Reducing the absorber-layer thickness not only reduces costs but also improves the electrical characteristics of the solar cell. By doing so, we can contribute to overcome today's efficiency limitations related to the use of physically thin silicon solar cells by making them optically thick. To reach this goal, we study the incorporation of a MNP plasmonics layer in μc-Si solar cells. On other hand, for SERS substrates, the optimal MNP sizes and inter-particle distances are much smaller than for Si cells, so a low-temperature nanoparticle formation method, largely applied to cellulose based substrates, was employed. Different types of cellulose substrates for SERS were investigated and their influence on the SERS signal, uniformity and stability was analyzed. Different strategies to enhance SERS signal were attempted, consisting in varying the inter-Ag-NPs gaps, sensing area, surface coverage (SC) of Ag NPs or employing new architectures, like 3D structures.

Within these broad themes, this study has a specific number of objectives: (1) Deposition and characterization of Ag nanoparticles for Si solar cells; (2) Development and characterization of plasmonic back reflector configuration to be integrated on solar cell devices; (3) – Optimization of plasmonic Ag NPs on cellulose based substrates to be used for SERS detection (4); SERS device fabrication.

In **chapter 1** an overview of topics from plasmonics, PV and SERS is presented, serving as a background for the experimental studies described in the following chapters. The plasmonics concepts are reviewed and the different aspects relating plasmonics NPs to PV and SERS are discussed.

Chapter 2 describes the production and characterization techniques used during the research work of this dissertation, mostly highlighting thermal evaporation, morphological and optical characterization of Ag NPs, solar cells and SERS substrates.

The experimental study begins with a systematic investigation, presented in **chapter 3**, of the correlation between the structural and the optical properties of self-assembled silver NPs fabricated on distinct surfaces (glass, zinc oxide (ZnO), aluminum zinc oxide (AZO) and gallium zinc oxide (GZO)) by RTA, which induced morphology transformation from a thin film to an array of islands or NPs. In order to do so, different mass thicknesses of Ag thin films were deposited on these substrates using the same deposition and post-deposition annealing conditions. The applicability of such Ag NPs in solar cells, in terms of light scattering, is discussed and their morphological and optical properties correlated with the substrate conductivity and roughness. Finally, the structural and optical properties of the best-obtained structures on AZO are analyzed. Next, the self-assembled Ag NPs are integrated in thin film silicon solar cells to form a PBR. First, the role of the RTA heating rate on the NPs production is studied, in order to understand the formation of Ag NPs with favorable monodispersed geometries and design routes to produce PBRs by an ultra-fast RTA process. After the establishment of the best conditions, we investigated the influence of the thicknesses of the AZO spacer/passivating layers between NPs and rear mirror, and between NPs and silicon layer, on the morphological and optical performance of the PBRs; and consequently on the performance of the solar cells. The performance of the PBRs was carefully adjusted, to yield maximum light trapping (low parasitic absorption and high near-infrared scattering) with minimum degradation of the cells' electrical properties.

The use of Ag NPs on cellulose based substrates, to be integrated in SERS devices, starts in **chapter 4.** The potential of a new kind of cost-efficient SERS substrate, called cardboard substrate (grammage exceeds 200–800 g m^{-2}, thickness above 300 µm), is evaluated. The morphology, size, and distribution of the Ag NPs are assessed, and their influence on the SERS signal is investigated by correlation with electromagnetic simulations and the measured optical properties. Strategies to increase the uniformity and reducing/suppressing instability of the substrates are also presented. Next, a simple strategy to enhance SERS signal on cellulose substrates is tested. We start the study with a standard cellulose substrate (grammage in the range of 80 g m^{-2} and 100 µm thick), with the particularity of the absence of a metal layer. Nanorods (NRs) of ZnO were directly grown on the raw substrates by a microwave heating technique and decorated with Ag NPs. In a separated experiment, a substrate without NRs was subject to the same NPs deposition. The size and distribution of the NPs as well as ZnO NRs sensing area and inclination are investigated, and their influence on the SERS signal is discussed. At the end, a pilot study on the best substrate will be done. The best substrates and configurations described in the previous sections were used for such tests.

Chapter 5 summarizes the findings and conclusions of this thesis and discusses the perspectives for further research on the topics of plasmonics for solar cells and SERS.

Publications during the thesis

As first author

[1] Araújo A, Mendes M J, Mateus T, Costa J, Nunes D, Água H and Martins R 2018 Ultra-fast plasmonic back reflectors production for light trapping in thin Si solar cells *Solar Energy, accepted for publication.*

[2] Pimentel A†, Araujo A†, Beatriz J, Coelho D N, Oliveira M J, Mendes M J, Águas H, Martins R and Fortunato E 2017 3D ZnO/Ag Surface-Enhanced Raman Scattering on Disposable and Flexible Cardboard Platforms *Materials* **10** 1351

[3] Araújo A, Pimentel A, Oliveira M J, Mendes M J, Franco R and Fortunato, Elvira, Águas, Hugo, Martins R 2017 Direct growth of plasmonic nanorod forests on paper substrates for low-cost flexible 3D SERS platforms *Flex. Print. Electron.* **2** 014001

[4] Araújo A, Mendes M J, Mateus T, Nunes D, Calmeiro T, Fortunato E, Hugo A and Martins R 2016 Influence of the Substrate on the Morphology of Self-Assembled Silver Nanoparticles by Rapid Thermal Annealing *J. Phys. Chem. C* **120** 18235–42

[5] Araújo A, Caro C, Mendes M J, Nunes D, Fortunato E, Franco R, Águas H and Martins R 2014 Highly efficient nanoplasmonic SERS on cardboard packaging substrates. *Nanotechnology* **25** 415202

[6] Araújo A, Barros R, Mateus T, Gaspar D, Neves N, Vicente A, Filonovich S a, Barquinha P, Fortunato E, Ferraria A M, Botelho do Rego A M, Bicho A, Águas H and Martins R 2013 Role of a disperse carbon interlayer on the performances of tandem a-Si solar cells *Sci. Technol. Adv. Mater.* **14** 045009–17

As co-author

[7] Vicente A T, Araújo A, Mendes M J, Nunes D, Oliveira M J, Sanchez-Sobrado O, Ferreira M P, Águas H, Fortunato E and Martins R 2018 Multifunctional Cellulose-Paper for Light Harvesting and Smart Sensing Applications *J. Mater. Chem. C* DOI: 10.1039/C7TC05271E

[8] Wannes H Ben, Zaghouani R B, Ouertani R, Araújo A, Mendes M J, Aguas H, Fortunato E, Martins R and Dimassi W 2018 Materials Science in Semiconductor Processing Study of the stabilizer influence on the structural and optical properties of sol-gel spin coated zinc oxide films *Mater. Sci. Semicond. Process.* **74** 80–7

[9] Pimentel A, Samouco A, Araujo A, Nunes D, Martins R and Fortunato E 2017 Ultra-Fast Microwave Synthesis of ZnO Nanorods on Cellulose Substrates for UV Sensor Applications *Materials* 4–10

[10] Sanchez-Sobrado O, Mendes M J, Haque S, Mateus T, Araujo A, Aguas H, Fortunato E and Martins R 2017 Colloidal-lithographed TiO2 photonic nanostructures for solar cell light trapping *J. Mater. Chem. C* **5** 6852–61

[11] Oliveira M J, Quaresma P, Almeida M P de, Araújo A, Pereira E, Fortunato E, Martins R, Franco R and Águas H 2017 Office paper decorated with silver nanostars - an alternative cost effective platform for trace analyte detection by SERS *Sci. Rep.* **7** 1–14

[12] Mendes M J, Araújo A, Vicente A, Águas H, Ferreira I, Fortunato E and Martins R 2016 Design of optimized wave-optical spheroidal nanostructures for photonic-enhanced solar cells *Nano Energy* **26** 286–96

[13] Vicente A, Águas H, Mateus T, Araújo A, Lyubchyk A, Siitonen S, Fortunato E and Martins R 2015 Solar cells for self-sustainable intelligent packaging *J. Mater. Chem. A* **3** 13226–36

[14] Gaspar D, Pimentel A C, Mendes M J, Mateus T, Falcão B P, Leitão J P, Soares J, Araújo A, Vicente A, Filonovich S A, Águas H, Martins R and Ferreira I 2014 Ag and Sn Nanoparticles to Enhance the Near-Infrared Absorbance of a-Si:H Thin Films *Plasmonics* **9** 1015–23

[15] Gaspar D, Pimentel A C, Mateus T, Leitão J P, Soares J, Falcão B P, Araújo A, Vicente A, Filonovich S a, Aguas H, Martins R and Ferreira I 2013 Influence of the layer thickness in plasmonic gold nanoparticles produced by thermal evaporation. *Sci. Rep.* **3** 1469–73

Book chapters

Vicente, A., **Araújo, A**., Gaspar, D., Santos, L., Marques, A. C., Mendes, M. J., Pereira, L., Fortunato, E., Martins, R., Optoelectronics and Bio devices on paper powered by solar cells. In: Nanostructured Solar Cells, 1st ed. InTech, 1–29, 2016 (ISBN: 978-953-51-4863-0).

Table of contents

List of Figures

List of Tables

Acronyms and Abbreviations

3D	Three-dimensional
AlGaAs	Aluminium gallium arsenide
AZO	Aluminum zinc oxide
AM	Air Mass coefficient
AFM	Atomic Force Microscopy
AC	Alternated contact
a-Si:H	Hydrogenated amorphous Silicon
B_2H_6	Diborane
B(CH3)3	Trimethylborane
BSE	Backscattered Electrons
c-Si	crystalline silicon
CdTe	Cadmium telluride
CIGS	Copper-indium-gallium selenide
CVD	Chemical Vapor Deposition
CEMOP	Centre of Excellence in Microelectronics Optoelectronics and Processes
CENIMAT	Centro de Investigação de Materiais
CE	Chemical Enhancement
EDS	X-ray Spectroscopy
EF	Enhancement Factor
EQE	External Quantum Efficiency
e-beam	Thermal evaporation assisted by electron beam
EM	Electromagnetic
FTO	Fluorine doped Tin Oxide
FIB	Focused Ion Beam
FF	Fill Factor

FET	Field Effect Transistors
GPD	Gross Domestic Product
GaAs	Gallium arsenide
GZO	Gallium zinc oxide
I3N	Instituto de Nanoestruturas, Nanomodelação e Nanofabricação
IZO	Indium zinc oxide
ITO	Indium tin oxide
InGaAs	Indium gallium arsenide
HW	Hotwire
HIT	Heterojunction
HDI	Human Development Index
IR	Infrared
LSP	Localized Surface Plasmons
LSPR	Localized Surface Plasmons Ressonance
LAFD	Laser Assisted Flow Deposition
LOD	Limit of detection
LOC	Limit of quantification
μc-Si	microcrystalline silicon
MNP	Metal Nanoparticle
MDR	Morphology Dependent Resonance
MD	Mean Diameter
MG	Malachite Green
NIR	Near-Infrared
NRs	Nanorods
NPs	Nanoparticles
NSs	Nanostars
nc-Si:H	Hydrogenated nanocrystalline silicon
pm-Si:H	polymorphous silicon

PEN	Polyethylene Naphthalate
PET	Polyethylene Terephthalate
PI	Polyimide
PH_3	Phosphine
PLD	Pulsed Laser
PVD	Physical Vapor Deposition
PECVD	Plasma-Enhanced Chemical Vapor Deposition
PBR	Plasmonics Back Reflectors
PV	Photovoltaic
PoC	Point of care
PDA	Post-Deposition Annealing
QE	Quantum Efficiency
RTA	Rapid Thermal Annealing
RF	Radio Frequency
R6G	Rhodamine 6 G
RE	Renewable Energy
RT	Room Temperature
SSD	Solid-State Dewetting
SC	Solar Cell
SERS	Surface Enhanced Raman Spectroscopy
SC	Surface Coverage
SPP	Surface Plasmon Polaritons
SE	Secondary Electrons
SR	Spectral Response
SiH_4	Silane
SQ	Shockley-Queisser
SEM	Scanning Electron Microscopy

TF	Thin Film
TFSC	Thin Film Solar Cells
TCO	Transparent Conductive Oxide
UV	Ultraviolet
VHF	Very High Frequency
Vis	Visible
XRD	X-Ray Diffraction
ZnO	Zinc oxide

Symbols

.	Scalar product
$\times$	Vector product
∇	Nabla operator
$\nabla \times$	Rotational
$\nabla \cdot$	Divergence
$\frac{\partial}{\partial t}$	Partial derivative
2θ	Peak orientation angle
α	Absorption coefficient
a.u.	Arbitrary units
Abs	Absorptance
A	Area
$\mathbf{B}$	magnetic induction field
c	Velocity of light in vacuum
C	Concentration
C_{sca}	Scattering cross sections
C_{abs}	Absorption cross sections
d	Particle size
D	Average NPs size
D	Grain size
$\mathbf{D}$	Displacement field
δ	Irradiance
$\mathbf{E}$	Electric field
e	Electronic charge (also denoted as q)
$\mathrm{E_{tauc}}$	Tauc’s optical gap
Eg	Bandgap

ε	Dielectric function
ε_0	Vacuum permittivity
η	Efficiency
f	Frequency
γ	Surface energy | Collision frequency
h	Planck’s constant
H	Magnetic field
θ	Contact angle | Bragg’s angle
I	Electrical current intensity | wave intensity
I_{SERS}	SERS intensity of a particular Raman vibrational line
I_{Raman}	Normal (not enhanced) Raman intensity
i	Imaginary number $\sqrt{-1}$
$\mathbf{J}$	Current density
J_{SC}	short circuit current density
$\mathbf{K}$	Wave vector
k_B	Boltzmann constant
κ	Extinction coefficient
λ	Wavelength
λ_{el}	Thermal conductivity via free electrons
$\mathbf{M}$	Magnetization
m	Mass of electrons
μ	Permeability
μ_0	Vacuum permeability
n	Refractive index; electron concentration
N	Absolute refractive index| free carrier concentration
N_{SERS}	Number of molecules contributing to the SERS signal
N_{Raman}	Number of molecules contributing to the reference Raman signal (from non-SERS surface)

N_A	Avogadro constant
$\mathbf{n}$	Unit vector
ν	Frequency
ω_p	Plasma frequency
ω	Angular frequency
Ψ	Sphericity
$\mathbf{p}$	Dipole moment inside the sphere
$\mathbf{P}$	Polarization
p	Deposition pressure
P	RF power density
R_{DIF}	Diffuse reflectance
R_{TOT}	Total reflectance
RMS	Root-mean-square roughness
R_S	Series resistance
R_{SH}	Shunt resistance
ρ	Charge density
ρ_0	Free charge density
σ	Electrical conductivity | Standard deviation
S	Spreading parameter
t	Time
τ	Relaxation time
T_{TOT}	Total transmittance
T_{DIF}	Diffuse transmittance
V	Volume
V_{OC}	Open-circuit voltage

Chapter 1

Introduction

In this chapter a broad overview of topics from Plasmonics, to Photovoltaics and Surface Enhanced Raman Spectroscopy is discussed, where emphasis is putting concerning to their exploitation using paper based substrates, providing so the background for the results presented in the thesis, where clear contributes for the science advances were achieved.

This chapter contains relevant information from the publication:

Vicente A T, **Araújo A**, Mendes M J, Nunes D, Oliveira M J, Sanchez-Sobrado O, Ferreira M P, Águas H, Fortunato E and Martins R 2018 Multifunctional Cellulose-Paper for Light Harvesting and Smart Sensing Applications *J. Mater. Chem. C* DOI: 10.1039/C7TC05271E

Vicente, A., **Araújo, A**., Gaspar, D., Santos, L., Marques, A. C., Mendes, M. J., Pereira, L., Fortunato, E., Martins, R., Optoelectronics and Bio devices on paper powered by solar cells. In: Nanostructured Solar Cells, 1st ed. InTech, 1–29, 2016 (ISBN: 978-953-51-4863-0).

1.1 Plasmonics

Plasmonics is a field of study that explores the interaction between electromagnetic radiation and collective oscillations of free electrons (a plasma oscillation) in metals. All metals can sustain plasmons, but the frequency at which it occurs depends on several aspects. For example, in a bulk metal (Figure 1.1 (a)) the plasmons that can be developed are mainly generated within the volume of the metal and can only be generated at very high frequencies ($\omega > \omega_p$). Metals have a shiny appearance, because at low frequencies the light cannot penetrate inside the metal, the metal electrons follow the field until they have compensated it. Above the plasma frequency, however, the external field oscillates too fast for the electrons to follow and the metal loses its reflectivity. However, other types of plasmons can be developed if the surface is in contact with a dielectric material (Figure 1.1 (b)), as propagating electromagnetic waves, called Surface Plasmon Polaritons (SPP) [1,2]. Surface plasmon polaritons are electromagnetic excitations propagating at the interface between a dielectric and a conductor, evanescently confined in the perpendicular direction. These electromagnetic surface waves arise via the coupling of the electromagnetic fields to oscillations of the conductor's electron plasma. The term "surface plasmon polariton" explains that the wave involves both charge motion in the metal ("surface plasmon") and electromagnetic waves in the air or dielectric.

When the size of the metal is reduced to the nano-scale, the plasmons are dominated by surface effects that are confined to the nanoparticle (Figure 1.1 (c)). Localized surface plasmons (LSP), unlike SPP, are non-propagating excitations of the conduction electrons of metallic nanostructures coupled to the electromagnetic field. We will see in the sub-section 1.4.3 that these modes arise naturally from the scattering problem of a small, sub-wavelength conductive nanoparticle in an oscillating electromagnetic field. The surface of the particle causes a restoring force on the displaced free electrons, which changes their plasma resonance relative to bulk. When such resonance (the LSP) occurs it leads to electromagnetic field amplification inside, in the near-field zone outside the particle, and in its propagating far-field scattered light. Another consequence of the effect of the nanoparticle surface is that the excitation of plasmon resonances can be driven solely by direct light illumination, in contrast to propagating SPPs, which require additional wavevector matching.

The absorption and scattering of photons by/from metal nanoparticles is strongly dependent on both real and imaginary components of the dielectric constants of the NPs. Therefore, in the next section the basic theory of Maxwell equations, behind the interaction of photons with metal nanoparticles, is discussed.

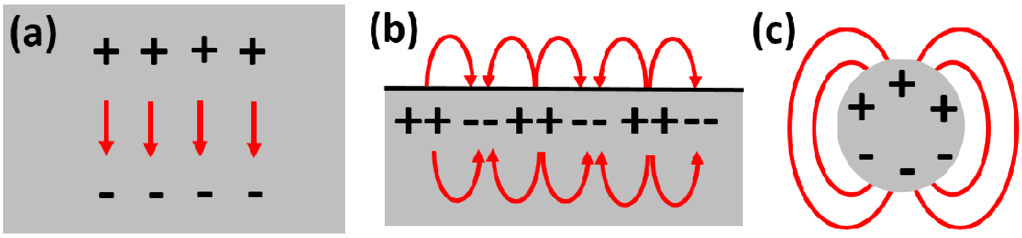

Figure 1.1 Schematic illustration of the different types of plasmons on metal materials with dimensions from macroscale to nanoscale. (a) volume plasmons in a bulk material, (b) bulk metal in contact with a dielectric, sustaining SPP and (c) LSPR, generated in metallic nanoparticles, dominated by surface effects.

1.1.1 Maxwell's equations and the dielectric function of the free electron

The interaction of metals (bulk or metallic nanostructures on the order of a few nanometres) with electromagnetic fields can be understood in a classical framework based on Maxwell's equations at macroscopic level. So, it is more convenient to include the charges fields and polarized currents in the atoms in two new fields $\mathbf{D}$ and $\mathbf{H}$. In function of these fields, the Maxwell's equations assume the following form [3]:

$$\nabla \cdot \mathbf{D} = \rho \tag{1. 1}$$

$$\nabla \times \mathrm{E} = -\frac{\partial \mathrm{B}}{\partial t} \tag{1. 2}$$

$$\nabla \cdot \mathrm{B} = 0 \tag{1. 3}$$

$$\nabla \cdot \mathbf{H} = \mathbf{J} + \frac{\partial \mathbf{D}}{\partial t} \tag{1. 4}$$

These equations link the four macroscopic fields $\mathbf{D}$ (the dielectric displacement), E (the electric field), H (the magnetic field), and B (the magnetic induction or magnetic flux density) with the external charge and current densities ρ_{ext} and J_{ext}. Where $\rho_{tot} = \rho_{ext} + \rho$ and $\mathbf{J}_{tot} = \mathbf{J}_{ext} + \mathbf{J}$.

The four macroscopic fields are further linked via the polarization $\mathbf{P}$ and magnetization M by:

$$\mathbf{D} = \varepsilon_0 \mathrm{E} + \mathrm{P} \tag{1. 5}$$

$$\mathrm{H} = \frac{1}{\mu_0} \mathrm{B} - \mathrm{M} \tag{1. 6}$$

where ε_0 and μ_0 is the electric permittivity and magnetic permeability of vacuum, respectively. Since these considerations can be limited to nonmagnetic media, we do not consider a magnetic response represented by $\mathbf{M}$. The response of the material can be described by the electric polarization $\mathbf{P}$, being the volume density of electric dipole moments inside the material caused by the alignment of microscopic dipoles with the electric field.

To solve Maxwell's equations it is necessary to relate the electric displacement to the electric field. The simplest case is the linear and isotropic media, in which the field $\mathbf{D}$ is parallel and directly proportional to E :

$$\mathbf{D} = \varepsilon_0 \varepsilon \, \mathrm{E} \qquad 1.7$$

where ε is called the dielectric constant or relative permittivity. Leading to the expression:

$$\mathbf{P} = \varepsilon_0 \, (\varepsilon - 1)\mathrm{E} \qquad 1.8$$

However, we have to point out that the statements (1.7) and (1.8) are only correct for linear media that do not exhibit temporal or spatial dispersion. Since the optical response of metals clearly depends on frequency (possibly also on wave vector) we must take account of the non-locality in time and space by generalizing the linear relationships. But, in the interaction of light with metals, the general form of the dielectric response ε (ω,K) can be simplified to the limit of a spatially local response via ε (K = 0, ω) = ε(ω). This simplification is valid as long as the wavelength λ in the material is significantly longer than all characteristic dimensions such as the size of the unit cell or the mean free path of the electrons.

In general, $\varepsilon(\omega) = \varepsilon_1(\omega) + i\varepsilon_2(\omega)$ is a complex function, where the real part (ε_1) describes the strength of the polarization induced by an external electric field and the imaginary part (ε_2) describes the losses encountered in polarizing the material. At optical frequencies, ε can be experimentally determined for example via reflectivity measurements at varying angles and polarizations (ellipsometry), linking the complex refractive index of the medium $\tilde{n}(\omega) = n(\omega) + i\kappa(\omega)$ with the complex dielectric response by $\tilde{n} = \sqrt{\varepsilon}$. Explicitly, this yields

$$\varepsilon_1 = n^2 - \kappa^2 \qquad 1.9$$

$$\varepsilon_2 = 2n\kappa \qquad 1.10$$

$$n^2 = \frac{\varepsilon_1}{2} + \frac{1}{2}\sqrt{\varepsilon_1{}^2 + \varepsilon_1{}^2} \qquad 1.11$$

$$\kappa = \frac{\varepsilon_2}{2n} \qquad 1.\ 12$$

κ is called the extinction coefficient and determines the optical absorption of electromagnetic field in the medium. The relation below links it to the absorption coefficient α of Beer's law $\mathrm{I(x) = I_0 e^{-\alpha x}}$ by the relation:

$$\alpha(\omega) = \frac{2\kappa(\omega)\omega}{c} \qquad 1.\ 13$$

1.1.2 The Drude theory of metals

The simplest realistic model for the dielectric constant of a metal is the Drude or free electron model. This model was proposed in 1900 [4] by Paul Drude to explain the transport properties of electrons in metals, applying the classical kinetic theory of gases (electrons are modelled as solid spheres and no forces act on them during the travel time) to the conduction electrons. In the Drude model the conduction electrons are treated as a free electron. Solving the equations of motion for a single electron, and multiplying them by the number of electrons per unit volume, we obtain their response to an electric field. The electrons oscillate in response to the applied electromagnetic field, and their motion is damped via collisions occurring with a characteristic collision frequency $\gamma = {}^{1}\!/_{\tau}$, τ is known as the relaxation time of the free electron gas (average time it travels before suffering collision).

For a harmonic time dependence of the driving field, the motion of electrons subjected to an external electric field E can be written as:

$$m\frac{\mathrm{d}^2x}{dt^2} + m\gamma\frac{dx}{dt} = -e\,\mathrm{E}_0\,e^{-i\omega t} \qquad 1.\ 14$$

and the solution is given by:

$$\mathrm{X}(t) = \frac{e}{m(\omega^2 + i\gamma\omega)}\mathrm{E}(t) \qquad 1.\ 15$$

The displaced electrons contribute to the macroscopic polarization by the relation $\mathbf{P} = -nex$, with n being the electron concentration and e the elementary charge, explicitly given by:

$$\mathrm{P} = -\frac{ne^2}{m(\omega^2 + i\gamma\omega)}\mathrm{E} \qquad 1.\ 16$$

Consequently, comparison with equation 1.8 yields the following expression for the dielectric constant [5,6]:

$$\varepsilon(\omega) = 1 - \frac{{\omega_p}^2}{\omega(\omega + i\gamma)} \qquad 1.\ 17$$

Where ω_p is the plasma frequency given by $\omega_p^2 = {ne^2}/{\varepsilon_0 m}$, where n is the electron density, ε_0 is the vacuum permittivity, and m_e is the effective mass of the electrons [5,6].

The real and imaginary components of the complex dielectric function ε(ω) = ε₁(ω) + i ε₂(ω) are given by:

$$\varepsilon_1(\omega) = 1 - \frac{{\omega_p}^2 \tau^2}{1 + \omega^2 \tau^2} \qquad 1.\ 18$$

$$\varepsilon_2(\omega) = \frac{\omega_p^2 \tau}{\omega(1 + \omega^2 \tau^2)} \qquad 1.\ 19$$

It is insightful to study (1.17) for a variety of different frequency regimes with respect to the collision frequency γ. For noble metals like Ag and gold (Au), the Drude model gives a good description of the dielectric constant in the near-infrared (NIR) region of the spectrum, but it starts to break down in the visible (Vis) to near-ultraviolet (UV) (specially with Au), because of the interband transitions [3,7–9]. Which for the case of Ag and Au, the two materials of highest importance for plasmonics, are 3.9 eV and 2.3 eV. In the case of Au, its validity breaks down already at the boundary between the near-IR and the Vis. So, the Drude model adequately describes the optical response of metals only for photon energies below the threshold of transitions between electronic bands.

In the case of noble metals (e.g. Ag, Au), the atoms consist of completely filled 3d-, 4d-, and 5d-shells having just a single electron in the 4s-, 5s-, and 6s-bands. Although, the optical response is essentially determined by the s-shell, the filled d-band close to the Fermi surface causes a residual polarization background due to ion cores. This effect can be described by adding a constant to the dielectric function, which leads to:

$$\varepsilon(\omega) = \varepsilon_{int} - \frac{{\omega_p}^2}{\omega^2 + i\gamma\omega} \qquad 1.\ 20$$

$$\varepsilon_1(\omega) = \varepsilon_{int} - \frac{{\omega_p}^2}{\omega^2 + \gamma^2} \qquad 1.\ 21$$

$$\varepsilon_2(\omega) = \frac{\omega_p^2 \gamma}{\omega(\omega^2 + \gamma^2)} \qquad 1.22$$

Figure 1.2 shows the real and imaginary components ε1 and ε2 for the dielectric function of silver, determined by Johnson and Christy [10] and a Drude model fit to the experimental data [10] according to the equations 1.20 with the following values of parameters $\varepsilon_{int} = 3.7$, $\omega_p = 9.2$ eV, $\gamma = 100$ THz.

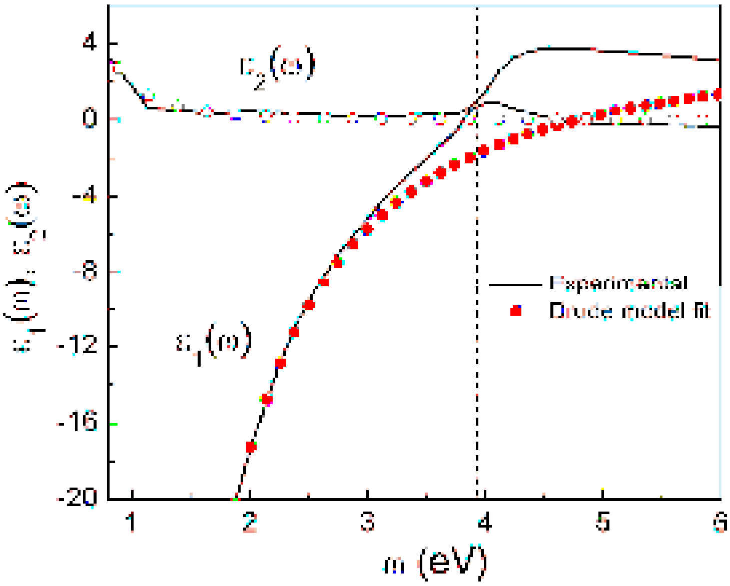

Figure 1.2 Drude model fit to the experimental data of Ag [40] according to the equations 1.20 with the following fitting parameters $\varepsilon_{int} = 3.7$, $\omega_p = 9.2$ eV, $\gamma = 100$THz. The dashed curve represents the threshold frequency for interband transition at 3.9 eV, indicating the limit for the validity of the free-electron model.

1.1.3 Localized Surface Plasmon Resonance

When light is incident on a metal nanoparticle, the oscillating electromagnetic field of the light leads to collective oscillations of the conducting electrons (plasmonics excitations). The subsequent polarization effects and restoring forces allow for the occurrence of a resonance behavior. In the wavelength region where the resonance occurs, light is most efficiently scattered at the nanoparticle. At the same time, also the parasitic absorption in the nanoparticle is enhanced. The beneficial feature is that light can be scattered in large angles outside the direction of the impinging light, in the so called 'forbidden zones'.

Figure 1.3 illustrates the distribution of the electric field inside and outside of an arbitrary nanoparticle. At resonance, MNPs can produce particularly intense localized near-field and propagating far-field scattering. The zone near the equator of the particle is where the electric field has greater intensity (near-field), being able to be ~ 100x higher than the intensity of the incident light. The MNP also produces far-field radiation that spreads away from it, in the form of spherical waves.

The MNPs far-field scattering has been considered as a promising light trapping mechanism, since it can improve the optical path length in photovoltaic devices [11,12]. SERS, on the other hand, takes advantage of the near–field, mainly associated to the enhanced local electric field intensity in the MNPs vicinity [13,14]. Such localized field enhancement can lead to highly amplified Raman scattering signals at the surface of the nanoparticles, resulting in an increase of Raman signals from molecules that have been adsorbed onto or are in the vicinity of nanometer-sized metallic particles [15].

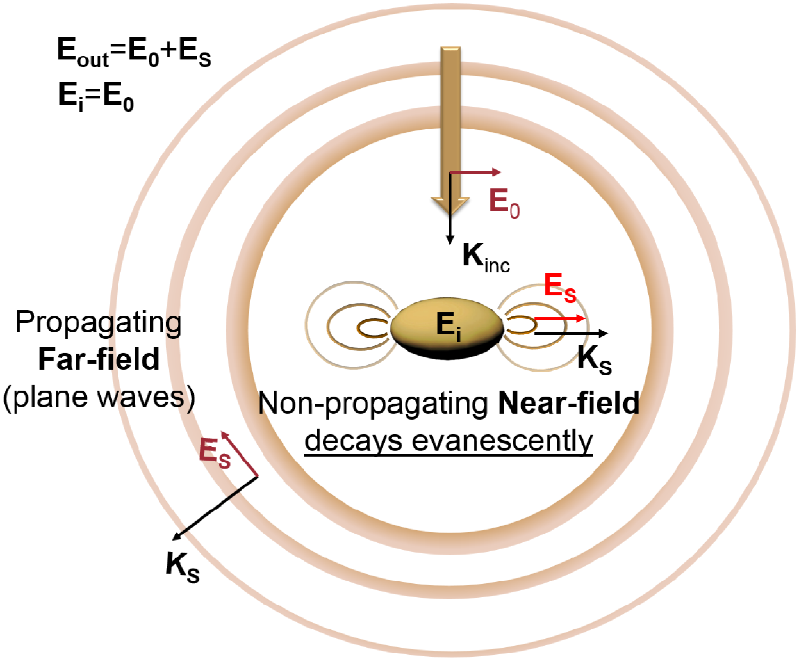

Figure 1.3 Schematic of the distribution of the electric field inside and outside of an arbitrary sized nanoparticle.

As previously mentioned, the maximum scattered field intensity is proportional to the polarizability of the particle [16]:

$$Max\,|\mathrm{E_S}|\propto\frac{\varepsilon_P(\omega)}{\varepsilon_m(\omega)+L_C\varepsilon_P(\omega)} \tag{1. 23}$$

Where $\varepsilon_p(\omega)$ and $\varepsilon_{\mathrm{m}}(\omega)$ are the dielectric functions of the particle and surrounding medium, respectively, and L_{C} is a geometric factor that dependents on the particle shape. Usually the surrounding medium is a dielectric material, so the $\varepsilon_m(\omega)$ has a positive value, as well as L_{C}. Since the material of the particle is metal, the $\varepsilon_p(\omega)$ has a negative value, which means that for a certain frequency the denominator in eq. 1.23 can be close to zero[1]. That situation corresponds to a resonance in the polarizability that occurs at the localized plasmon frequency of the particle and maximizes the field dispersed by the particle.

1.1.4 Sub-wavelength metal particles

When an electric plane-wave impinges on a particle (size *d*) much smaller than its wavelength ($d << \lambda$) the electric field induced inside the particle can be assumed uniform [17]. As such, the scattering problem can be simplified to a particle in an electrostatic field, known as quasi-static approximation [18].

We start with the most convenient geometry for an analytical treatment: a homogeneous, isotropic sphere with radius a, located at the origin in a uniform, static electric field $\mathrm{E} = \mathrm{E}_0 \hat{\mathbf{z}}$ as depicted in Figure 1.4. The surrounding medium is taken to be isotropic and non-absorbing with dielectric constant ε_m and the sphere is described by a complex dielectric function $\varepsilon(\omega)$. The electric field is parallel to the z-direction at sufficient distance from the sphere. Solving the Maxwell equations in this regime, we obtain that the nanoparticle responds as a dipole, creating around it a dipolar-like electric field distribution [19].

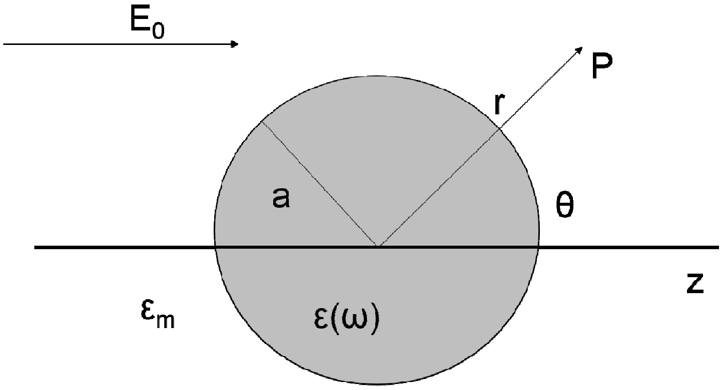

Figure 1.4 Sketch of a spherical particle with radius a and complex dielectric function $\varepsilon(\omega)$ placed in homogeneous medium ε_m.

The distribution of the electric field inside ($\mathrm{E}_{\mathbf{in}}$) and ($\mathrm{E}_{\mathbf{out}}$) outside the particle is given by [18]:

---

[1] Note that the quantity in the denominator of eq. 1.23 never really reaches zero due to the imaginary components of the dielectric functions

$$\mathbf{E_{in}} = \frac{3\varepsilon_{\mathrm{m}}}{\varepsilon_{\mathrm{p}} + 2\varepsilon_{\mathrm{m}}}\mathbf{E_0} \qquad 1.\ 24$$

$$\mathbf{E_{out}} = \mathrm{E}_0 + \frac{3\mathbf{n}\,(\mathbf{n}\cdot\mathbf{p}) - \mathbf{p}}{\varepsilon_{\mathrm{p}} + 2\varepsilon_{\mathrm{m}}}\frac{1}{\mathrm{r}^3} \qquad 1.25$$

Where $\mathbf{E_0}$ is the incident electric field, ε_{p} the dielectric function of the sphere, ε_m the dielectric constant of the isotropic and non-absorbing surrounding medium, **p** the dipole moment inside the sphere, *r* is the radial distance to point P and **n** the unit vector in the direction of the point P.

The radiation of the dipole leads to scattering of the plane wave by the sphere. The corresponding cross sections for scattering and absorption, C_{sca} and C_{abs} determined via the Poynting-vector of such an oscillating electric dipole, are given by [16]:

$$C_{\mathrm{sca}} = \frac{k^4}{6\pi}\left|\alpha\right|^2 = \frac{8\pi}{3}ka^6\left|\frac{\varepsilon - \varepsilon_{\mathrm{m}}}{\varepsilon + 2\varepsilon_{\mathrm{m}}}\right|^2 \qquad 1.\ 26$$

$$C_{\mathrm{abs}} = k\mathrm{Im}\left[\alpha\right] = 4\pi ka^3\ \mathrm{Im}\left|\frac{\varepsilon - \varepsilon_{\mathrm{m}}}{\varepsilon + 2\varepsilon_{\mathrm{m}}}\right| \qquad 1.\ 27$$

Where α is the (complex) polarizability of a small sphere of sub-wavelength diameter in the electrostatic approximation.

It is important to note that, for small particles with $a \ll \lambda$ the efficiency of absorption, scaling with a^3, dominates over the scattering efficiency, which scales with a^6. Therefore, the optical response of small particles is dominated by absorption, while due to the rapid increase of C_{sca} with NP size, the response of big particles is chiefly driven by scattering.

Though the theory of dipolar particles outlined above is valid only for small sub-wavelength particles, it assures a reasonably good agreement for spheres with dimensions below 100 nm illuminated with visible or near infrared radiation, and is adequate for the purpose of the chapters 4 related with SERS. For particles of larger dimensions (>100 nm, as those used for solar cell light trapping), where the quasi-static approximation is not justified due to significant phase-changes of the driving field over the particle volume, a rigorous electrodynamic approach is required.

In 1908 Mie [20] developed a complete theory of the scattering and absorption of electromagnetic radiation by a sphere, in order to understand the colors of colloidal Au particles in solution. The approach of what is now known as *Mie theory* is to expand the internal and scattered fields into a set of normal modes described by vector harmonics. The formalism allows the calculation of the electric and magnetic fields inside and outside a spherical object and it is generally used to calculate either how much a plane electromagnetic wave is scattered or absorbed by uniform isotropic particles of the simplest form (sphere or infinite cylinder with arbitrary radius) which are in a uniform, isotropic dielectric infinite medium.

In the Mie regime, morphology dependent resonance (MDR) of a metal particle has been reported for example in refs. [12,17,21,22]. As seen in the previous section, particles much smaller than the wavelength scatter in the electrostatic regime as dipoles. The amount of light that they radiate through scattering is low (as mentioned previously), since most of the impinging light is absorbed inside the particle material (parasitic absorption). With larger particles, superposition of multiple reflections within the sphere leads to enhanced modes. Specially, 100 nm or higher NPs sizes lead to the appearance of a quadrupole mode and to a red-shift and increase in the scattered intensity at the dipolar mode. These MNP sizes exhibit pronounced scattering cross sections that are much higher than their absorption cross sections, so their light scattering performance exceeds their parasitic light losses in the wavelength range of interest for thin film Si solar cells [23,24]. Therefore, such size range is the one selected for light trapping in solar cells (Chapter 3).

1.2 Si solar cells enhanced by plasmonics

1.2.1 Energy challenge

Energy is universally acknowledged to be the bastion of an industrial society. Any interruption in the path of supply of energy jeopardizes the stability of the social and economic order, as well as the political structure of a society. Electrical energy is the most versatile and flexible form of energy that we use for an ever growing number of applications at the present time. Human well-being is a direct function of power consumed, or the rate at which work is done. The relationship between rate of energy consumption and rate of wealth production should not surprise anyone. The faster the work is done (more power consumed), more wealth that is produced. The great increase in the world's wealth since the Industrial Revolution is the obvious outcome of using fossil fuels to provide the energy for machines to do work. We got richer in the last couple of centuries in large measure because we used so much fossil energy. If we are not able to maintain high-energy consumption rates, the data summarized below strongly suggest that we will get poorer, sicker and less educated. This is well demonstrated in the Figure 1.5. About 93% of the variation in per capita wealth production ((GDP per capita) between different countries can be explained simply by how fats they use energy [25].

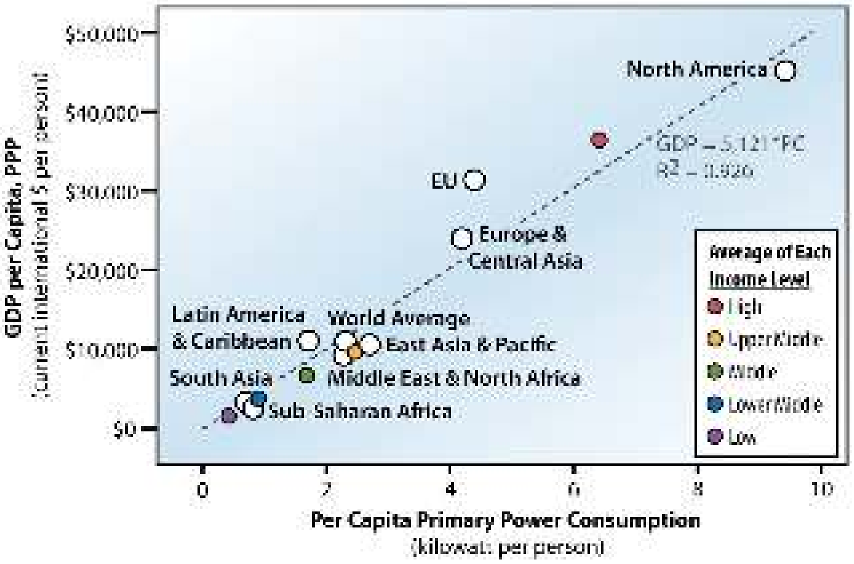

Figure 1.5 Relationship between GDP per capita and primary power consumption per capita for world regions [25].

In Figure 1.6 we see how the quality of life of any country, usually evaluated by the human development index (HDI), a composite measure of life expectancy, education and gross domestic product (GDP)[2], depends significantly on the consumption of electricity (kWh/annum) by that particular country [26]. HDI rises rapidly with increased power consumption and levels off at about 2-4 kilowatts (kW) per capita. Apparently we need about 2-4 kW per capita to achieve good levels of health, education and wealth [25]. But the rate at which world supplies of inexpensive fossil energy sources (coal, oil and natural gas) are being consumed exceeds the rate of replenishment, and the depletion of oil resources is expected in the not-too-distant future. These are non-renewable resources. When they are exhausted, the wealth they produce will likewise disappear. Further, burning of fossil fuels is arguably one of the contributors to global warming, and hence the effect of human activities on global climate change demands efforts to be directed towards energy conservation and developing renewable technologies.

Thus, very large-scale renewable energy (RE) systems are not just a “good idea”; they are essential. If we do not implement large-scale renewable energy systems now, we can count on being much poorer in the future.

---

[2] Gross domestic products accounts for the total output of goods and services from a nation and is a measure of the economic growth of the nation

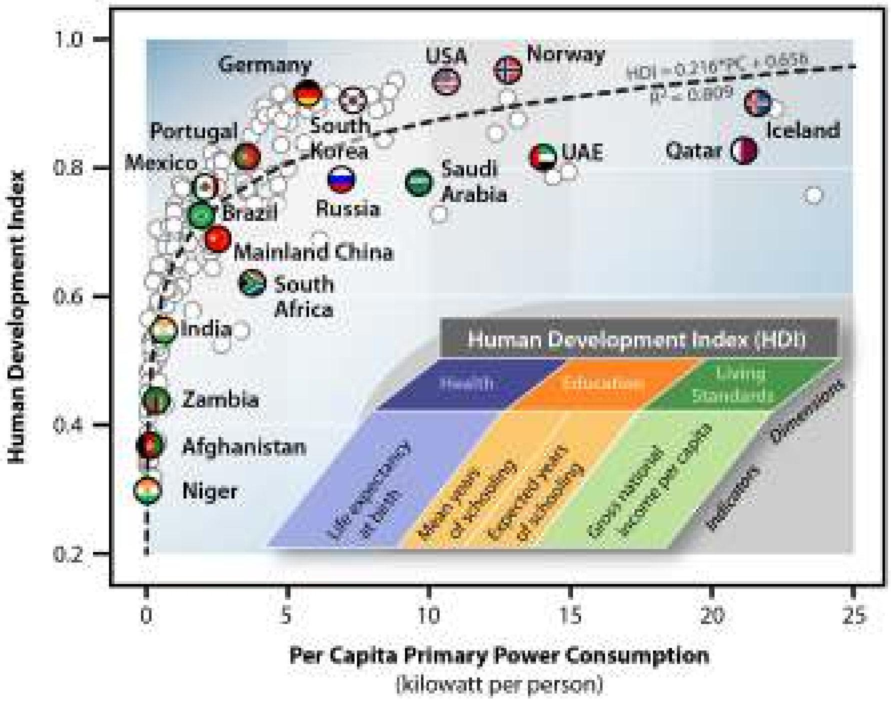

Figure 1.6 Human Development by Country versus Per Capita Power Consumption [25].

1.2.2 Renewable Energy

To keep the momentum of development alive, we have only three choices: we continue applying the answers of the last century such as burning more fossil fuels, building more nuclear plants (despite having no method of safely disposing of the high-level radioactive waste) or to apply the new millennium's answer of renewable, sustainable, non-polluting, widely available clean energy like photovoltaics and wind. Currently, non-renewable, finite fossil fuels – petroleum, natural gas, and coal – contribute over 85% of the 16.3 TW of global power consumption (annual average).

The statistics shown in Figure 1.7 indicates that the electricity investment has been broadly stable since 2011 after a period of rapid growth over the previous seven years. The slowdown reflects fewer fossil fuel generation capacity additions and falling costs for solar PV and wind [27]. For the first time, investment in renewables-based capacity generates enough power to cover global electricity demand growth in 2015. New renewables commissioned in 2015 had the capacity to generate 350 terawatt hours (TWh), against an increase in demand of less than 250 TWh. This means all other capacity brought online in 2015 was effectively surplus to requirements.

Rapid cost deflation in wind and solar PV, technology progress and more widespread deployment have led to a 40% jump in capacity additions and a one-third increase in annualise output since 2011.

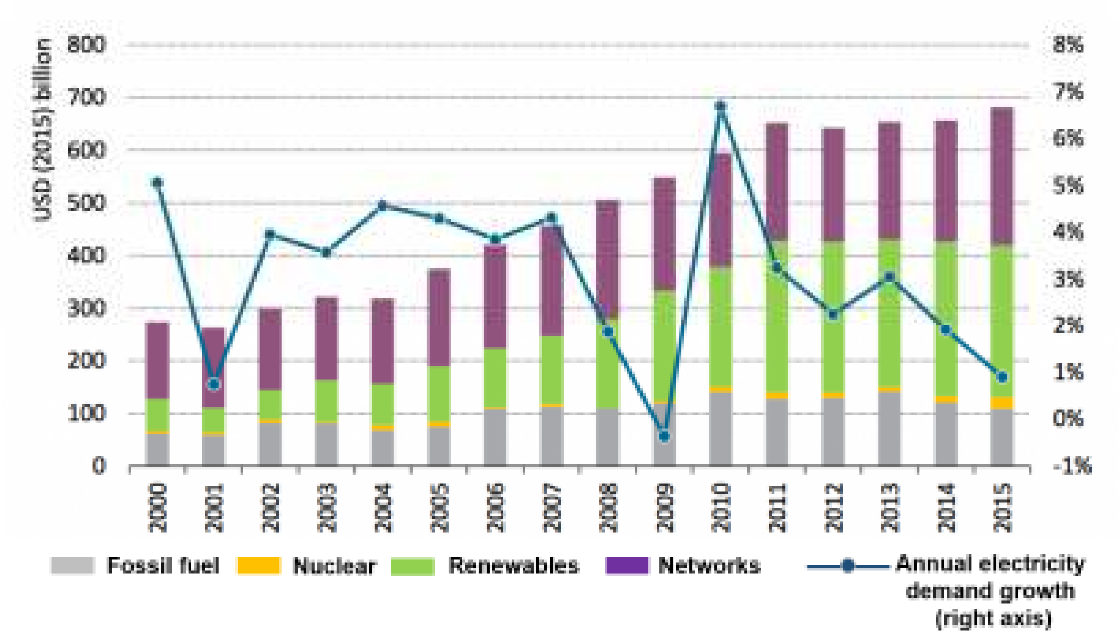

Figure 1.7 Global investment in power generation and electricity networks (coloured bars, left axis) and electricity demand growth (line, right axis). Source: World Energy Investment 2016, IEA.

1.2.3 Photovoltaics

Human life-style being related to energy is a well-documented fact. The poor and developing countries (ironically blessed with copious sun power) with limited conventional energy sources, particularly in remote areas, are increasingly turning to PV energy for enhancing their development index [28,29]. Photovoltaics is an empowering technology that has a potential of long-term substitute for today's conventional electricity production but in a sustainable, pollution-free, equitable fashion [30]. A large number of countries, developing and developed, are seriously involved in creating and nurturing PV industries. No other renewable energy technology receives such a strong appreciation by the public, and to an increasing extent also by the politicians and the industrial and financial sectors. However, the future trend for PV is to be able to supply energy at a lower cost [see Figure 1.8].

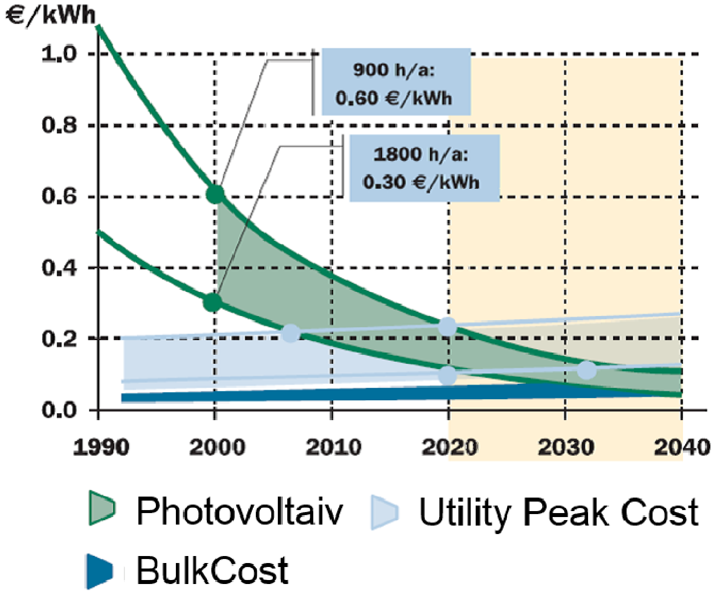

Figure 1.8 Cost projections for photovoltaic electricity. The upper boundary of photovoltaic costs reflects the situation of Germany, the lower boundary that of Southern Europe [31].

PV technologies are generally classified based on their efficiency and price per watt peak, and can be categorized in three groups, following the suggestion of M. Green [32]: first-, second-, and third generation.

First generation solar cells are mainly based on wafer-based materials (single/multicrystalline Si, gallium arsenide (GaAs), and other III-V semiconductors such as indium gallium arsenide (InGaAs) and aluminum gallium arsenide (AlGaAs)). Recent developments over single p-junction, antireflection coatings, surface passivation and heavily doped contact regions demonstrate a maximum performance (under the global AM1.5 spectrum (1000 W/m^2) at 25°C) of a HIT (Heterojunction) c-Si (crystalline Si) solar cell by Kaneka group, of about 26.7 % for cell (n-type rear) and 24.4 % for modules (108 cells) [33]. So far, the highest efficiencies of 28.8% for single-junction solar cell were achieved with GaAs in 2011 by Alta devices [34]. The benefits of this solar cell technology lie in their good performance, as well as their high stability. However, they are rigid and require a lot of energy in production.

The second generation solar cells are based on thin films hydrogenated amorphous and microcrystalline Si (a-Si:H, μc-Si:H), cadmium telluride (CdTe), and copper-indium-gallium selenide (CIGS), with maximum reported cell efficiencies of 10.2 % , 11.9%, 21.0%, and 21.7%, respectively [32]. Since the second generation solar cells avoid the use of Si wafers and have a lower material consumption it has been possible to reduce the production costs of these types of solar cells compared to the first generation. Furthermore, this second generation of solar cells allows the deposition on cheap substrates, like glass, stainless steel, even plastic and cellulose based substrate.

The third generation solar cells ought to combine the advantage of high efficiency and low production cost and are potentially able to overcome the Shockley–Queisser limit [35] for single bandgap solar cells. This generation of solar cells includes organic cells, multi-layer cells, and other innovative concepts such as: frequency conversion, (i.e. changing the wavelength of light that the cell cannot use to light wavelength that the cell can use - thus reaching higher efficiencies) [36], hot-carrier effects and other multiple-carrier ejection techniques, spectral splitting, photon up- and down-conversion, III-V multi-junction cells, intermediate bandgap cells, extraction of hot carriers and thermal photovoltaics.

1.2.4 Silicon photovoltaic technology

Si constitutes about 26% of the Earth's crust and is the second most abundant element in weight, oxygen being the largest one. At present, the solar-cell market is dominated by c-Si solar cells with thicknesses between 180–300 µm. A high percentage of the price of solar cells is due to the costs of Si (50% of the total cost) and processing. However, one of the reasons why crystalline Si solar cells dominate the market, is that the life time of c-Si modules is as long as 25 years and it does not have a significant degradation effect over the years. Wherever, some concerns exist regarding a shortage of the purified Si for the PV industry. Consequently, low-cost alternatives and high-efficiency novel concepts, many already in development, are needed.

Thin-film cells can offer a direct cost advantage associated with the use of less Si and by employing thin-film technologies that are deemed to be low-cost methods [37–39] when compared with Si wafers technology. Besides that, thin-film solar cells, with film thicknesses in the range 1–2 µm, can be deposited on cheap module-sized substrates such as glass, plastic or stainless steel [40].

For a given thin film Si material, a reduction in the cell thickness can result in improving the open-circuit voltage (V_{OC}) and the fill factor (FF) of the solar cell. However, as the cell thickness is reduced, the absorption, and thus, the photocurrent of the solar cell reduces. At the same time, the surface recombination becomes an increasingly important component of the total recombination [41]. In particular, surface recombination can severely degrade the V_{OC}. However, if the surface recombination problem is solved, the loss in photocurrent and optical losses associated with thickness reduction can be compensated through superior light-trapping design, allowing thinner cells to yield higher voltages and higher fill factors and thus can be more efficient than their thicker counterparts [37,40,42,43].

Si, when deposited in thin film form by the decomposition of silane (SiH_4) and H_2 (Hydrogen) mixture using CVD (Chemical Vapor Deposition) methods, can lead to a variety of structures with different bandgaps and optoelectronic properties ranging from a-Si:H, nanocrystalline Si (nc-Si:H), μc-Si:H, polymorphous Si (pm-Si:H) and protocrystalline Si depending on the deposition condition [44]. Besides that, the possibility of shifting the Fermi level in the gap state of these materials by using dopant gases like phosphine (PH_3) and diborane (B_2H_6) or Trimethylborane (TMB) during deposition is also one of the attractive features of Si thin film based devices. An effective approach to increase solar cell efficiency is by covering the maximum range of solar spectrum through multijunction thin film solar cell architectures combining different bandgap (Eg) materials [45,46]. The feasibility of fabrication of different bandgap refers to the energy difference (in electron volts) between the top of the valence band and the bottom of the conduction band, and defines the value of the energy photon that can be absorbed within the material, determining what portion of the solar spectrum a photovoltaic cell absorbs) Si thin films in the same deposition system by tuning the deposition conditions offers a cost effective industrially feasible solution for photovoltaic industry. That is the reason why Si still remains the most common material used in thin film solar cells. Several possible CVD techniques are today employed to deposit these materials like RF (radio frequency) plasma-enhanced (PE) CVD [47,48], very high frequency (VHF)-PECVD [49,50] and hotwire (HW)-CVD [51]. So far most of the industries are adopted the use RD PECVD and some of them are now using VHF PECVD also.

1.2.5 Fundamentals of solar cell operation

Solar spectrum

The intensity of solar irradiation directly outside the earth's atmosphere is almost constant and estimated at 1,367 Wm^{-2}. In general, the various layers of the atmosphere attenuate this value. The sun light gets reflected back outside, absorbed and scattered and as such it depends on the time of the year, latitude, processes in the atmosphere and also the geometry of the surface [52].

In order to be able to benchmark PV products, standard test conditions have been designed. These conditions include spectrum, intensity and temperature. They are prefixed "AM", which stands for "Air Mass" (commonly used to refer the sun spectrum at different latitudes) and followed by a number. The entry point into the atmosphere is called "AM0", where "0" points out that there is no air mass, indicating the pathlength of extraterrestrial light through the atmosphere. AM1.5 defines spectral irradiances and photon fluxes on tilted surface (37°) with zenith angle of 48.2 ° facing south, albedo 0.3, turbidity 0.29 and 20°C ambient temperature. The distinction between the total radiation (AM 1.5 Global) and the direct component only (AM1.5 Direct) is depicted in

Figure 1.9. The AM1.5 Direct solar spectrum is measured at the surface of the Earth with a surface element perpendicular to the Sun, considering only the radiation coming from small surroundings of the sun disc (5.8° aperture angle); while the AM1.5 Global spectrum considers the skylight coming from the full hemisphere. The AM1.5 G spectrum entails a power flux of about 963.8 Wm^{-2} while the AM1.5 D has the value of 768.3 Wm^{-2}.

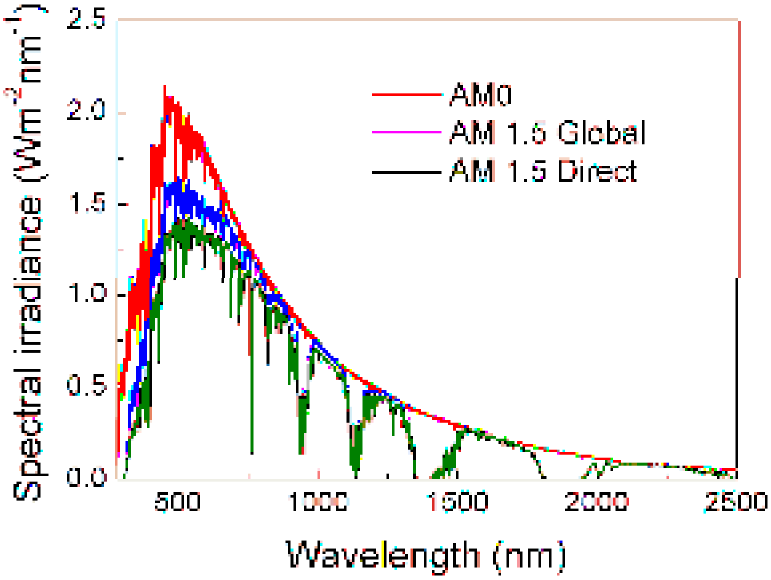

Figure 1.9 The spectral irradiance for extraterrestrial (AM0), terrestrial global (AM 1.5G) and direct (AM 1.5D) solar radiation defined in the standard ASTM G173-03.

Optimal bandgap for a solar cell and usable part of solar spectrum

As previous mentioned, only photons with an energy higher than the bandgap energy can produce electron and hole carriers and generate electricity, so the maximum current obtainable from the incident radiation and the maximum voltage of a solar cell depends on this value.

At a low Eg, the open circuit voltage is low, as all the energy of electrons excited with photo-excited electrons higher than Eg is lost. For example, if a photon has 1.7 eV and falls onto a 1.1 eV cell, the excess energy (0.6 eV) will be lost in the form of heat. At the same time, with lower bandgap it is possible to obtain higher short circuit current (because they absorb larger parts of the spectrum). At higher bandgap the opposite happens. The clear trade-off between the two effects is limiting the maximum efficiency of a one bandgap material and is called the Shockley-Queisser (SQ) limit [35]. Shockley and Queisser have shown in a detailed balance that the efficiency for a single bandgap semiconductor, has a maximum value of 33% with an optimum bandgap material for AM1.5 solar spectrum [35,53]. But, The SQ formulation idealizes a solar cell to have no imperfections or defects, like small deviations in material quality or optical design [53]. This limit was later modified by M.A. Green to be 31%, when considering the Auger recombination effect which would convert the recombined energy into an electron instead of giving off a photon [11].

Design concepts of thin film Si solar cell

Two different designs for Si thin film solar cells have been developed compatible with transparent or opaque substrates (Figure 1.10) [54–56]. In the superstrate design, sunlight enters through the transparent substrate, which is usually glass or a transparent plastic. The insulating substrate needs a conducting layer, which is typically a “transparent conductive oxide” (TCO) such as, fluorine-doped tin oxide (FTO)[12], zinc oxide-doped indium oxide (IZO) [57,58], indium tin oxide (ITO) [39,59] or gallium-doped zinc oxide (GZO) [60,61]. Later, different p, i and n Si layers are consecutively deposited. In thin film Si solar cells, the Si layers and the metal rear contact are usually separated with a 30–60 nm aluminum-doped zinc oxide (AZO) thin film [39,62]. The TCO layer acts as a barrier, which not only inhibits charge carrier recombination but also prevents the migration of metallic impurities from the particles to the photovoltaic material. Finally, the “back” metallic reflector is deposited, which also acts as an electrode to the n-layer. In the substrate design, sunlight enters the cell before it reaches the substrate. Starting with the substrate, the cell is fabricated in the reverse order compared to the superstrate design: first a back reflector, TCO, then different n, i and p layers (starting with an n-type layer) are deposited and finally a TCO layer to act as an electrode to the topmost, window layer of the cell. These two designs permit a very wide range of applications for Si thin film solar cells. The superstrate design is particularly suited to building-integrated solar cells in which a glass substrate can be used as an architectural element [43,45]. The substrate design has generally been applied to solar cells using flexible opaque substrates [57,63].

To use a broader part of the solar spectrum efficiently, solar cells with different bandgaps can be stacked on top of each other, are called tandem cells [50,64]. In multi junction solar cells, the voltage over the whole stack is equal to the sum of the voltages over the different sub cells, whereas the current through the stack is determined by the current in the sub cell with the lowest generated current. The cell with the lowest current is said to be current-limiting. Because the current-limiting cell determines the current through the whole stack, therefore it is important to match the currents in the different sub cells as much as possible. The highest efficiency of a double junction of a-Si/nc-Si (cell) , and triple junction of a-Si/nc-Si/nc-Si (cell) was achieved by AIST institute, with remarkable values of about 12.7 % and 14.0 %, respectively [32].

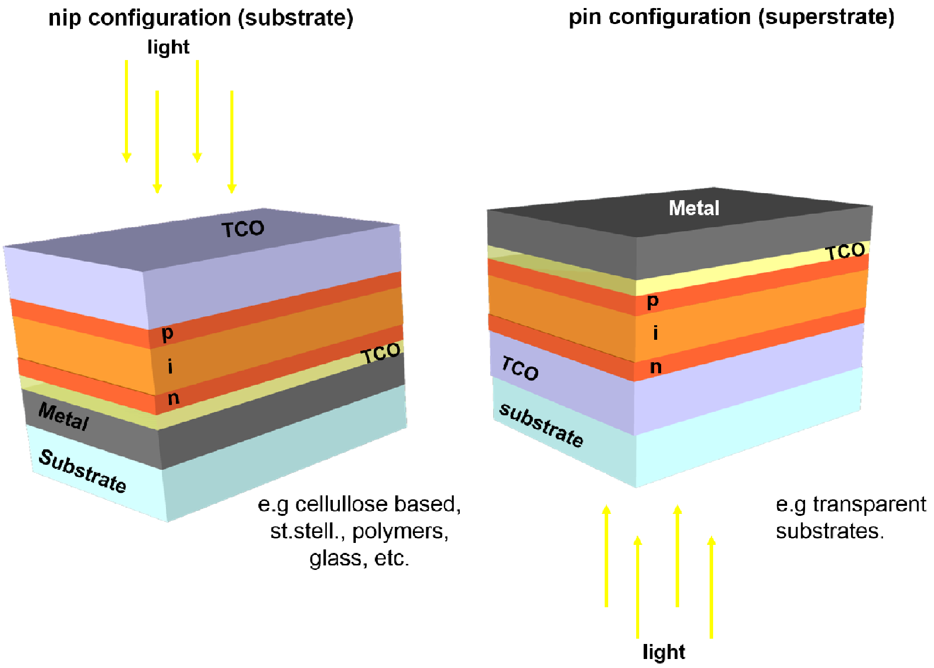

Figure 1.10 nip and pin designs in thin film Si solar cells

Essential parameters of a solar cell

Since a solar cell is essentially a diode, it is useful to create a model which is electrically equivalent (inset of Figure 1.11), consisting of a current source, due to light generated current, in parallel with a diode. When there is no light present to generate any current, the PV cell behaves like a diode. As the intensity of incident light increases, the PV cell generates current.

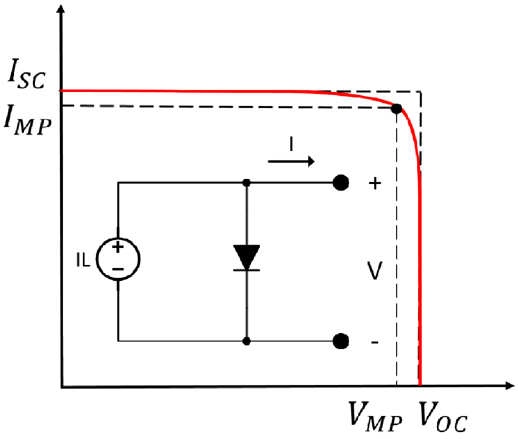

Figure 1.11 The current-voltage (I-V) characteristics of illuminated solar cell showing the operating parameters, short-circuit current (I_{SC}) and open-circuit voltage (V_{OC}). Inset: equivalent circuit of an ideal solar cell.

The I-V curve of a solar cell depicted in Figure 1.11 is a combination of the I-V curve of the solar cell diode in the dark with the light-generated current. In an ideal cell, the total current I is equal to the current generated by the photoelectric effect I_L minus the diode current, according to the equation:

$$I = I_L - I_D = I_L - I_0 \left(e^{\frac{qV}{n\kappa_B T}} - 1 \right) \qquad 1.31$$

where I_L is the maximum current produced by the cell, I_0 is the dark saturation current, q is the elementary electronic charge (1.602 × 10^{-19} C), κ_B is the Boltzmann constant (8.617 × 10^{-5} eVK^{-1}), T is the temperature and n is the diode ideality (quality) factor. The n factor has typical values between 1 and 2, with n ≈ 1 for diode dominated by recombination in the quasi-neutral regions and n → 2 when recombination in the depletion region dominates.

Several important parameters, which are used to characterize solar cells are discussed below. The short-circuit current (I_L), the open-circuit voltage (V_{OC}), the fill factor (FF) and the efficiency (η) are all parameters determined from the I-V curve.

The short-circuit current corresponds to the short circuit condition when the impedance is low and is calculated when the voltage equals 0. For an ideal device without parasitic resistances the I_{SC} equals the total current produced by photon excitation I_L .

The open-circuit voltage occurs when there is no current passing through the cell ($I = 0$). In other words, high V_{OC} is obtainable when, in open circuit condition, all non-radiative recombination paths are suppressed and all photo-generated carriers recombine radioactively.

The maximum power (P_{max}) produced by the cell in watts can be easily calculated from the I-V plot by the equation $P_{max} = V_{MP} I_{MP}$, plotted in Fig. 1.11. At the I_{SC} and V_{OC} points, the power will be zero and the maximum value for power will occur between the two. The voltage and current at this maximum power point are denoted as V_{MP} and I_{MP} respectively. The two rectangular areas defined by $V_{OC} I_{SC}$ and $V_{MP} I_{MP}$ provide a convenient way of characterizing the maximum power point, by the fill factor parameter:

$$FF = \frac{V_{MP} I_{MP}}{V_{MP} I_{SC}} \qquad 1.32$$

The FF is also interpreted as a measure of the squareness of the I-V curve. A larger fill factor is desirable, and corresponds to an I-V sweep that is more square-like. Typical fill factors range from 0.5 to 0.82 and have values lower than 1.

The power conversion efficiency, is the most commonly used parameter to compare the performance of solar cells, which is defined as the ratio of the maximum electrical power output P_{max}, to the solar power input, P_{in}, into the PV cell, and is defined as:

$$\eta = \frac{P_{max}}{P_{in}} = \frac{V_{OC} I_{SC} FF}{P_{in}} \qquad 1.33$$

Terrestrial solar cells are measured under AM1.5 conditions and irradiance of 1 kWm^{-2}, in ambient temperature of 25°C.

During operation, the efficiency of solar cells is reduced by the dissipation of heat across internal resistances. These parasitic resistances can be modeled as a parallel shunt resistance (R_{SH}) and series resistance (R_S). Expanding the equation 1.31 gives the simplified circuit model shown in Figure 1.12 and the following associated equation:

$$I = I_L - I_0\left(\exp\left(\frac{qV}{n\kappa_B T}\right) - 1\right) - \frac{V + IR_S}{R_{SH}} \qquad 1.34$$

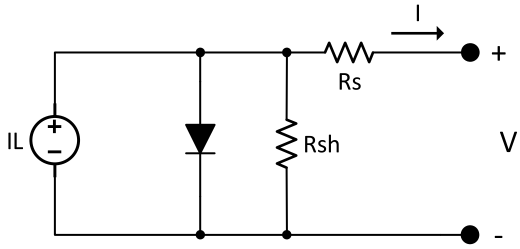

Figure 1.12 Simplified Equivalent Circuit Model for a Photovoltaic Cell with parasitic resistances.

The presence of parasitic resistances results in a significant decrease of the fill factor, and hence the efficiency. For an ideal cell, R_{SH} would be infinite whereas R_S would be zero giving no voltage drop before the load. However, decreasing R_{SH} and increasing R_S of will decrease the FF, and hence the efficiency. In general, decline of shunt resistance has no impact on the I_{SC}, the V_{OC} will drop. On the contrary, the incline of series resistance has no effect on the V_{OC}, but reduces the I_{SC}.

1.2.6 Light trapping

A limitation in TF solar cell technologies (e.g. Si, GaAs, CdTe) is that the absorbance of near-bandgap light is small [43], due to the fact that the absorption coefficient decreases abruptly with increasing illumination wavelength and to their reduced material thicknesses, in particular for indirect-bandgap semiconductors as Si. For example, in nc-Si the absorption coefficient drops quickly below 1000 cm^{-1} for wavelengths above 800 nm [46]. Since the absorption of photons to produce electron-hole pairs is an essential step, enhancement of light absorption by light trapping is crucial to obtain highly efficient TF-Si solar cells. This enables the long-wavelength photons to travel in the solar cell distances much longer than the device thickness, increasing the probability of their absorption. Light trapping is usually achieved by the scattering of incident light at the interfaces, either in transmission at the front surface or in reflection at the rear one. In addition, when the angle at which light is scattered is equal or greater than the critical angle for total internal reflection ($\theta c \approx 16°$ for the Si/air interface), the light can be coupled to the waveguide modes [24] and trapped within the absorber, unless a re-scattering event at an angle within the escape cone occurs before absorption.

In conventional TF Si solar cells, light trapping is typically achieved using random texturing of either the front contact (TCO), in superstrate cell configurations [43,65,66], or textured mirrors in substrate configurations [67–69]. However, the texturing approach means a high surface roughness, which contributes to the creation of defects, and as a consequence, increases recombination in the bulk and surface of the Si layers, which degrades the electrical performance of the device [70]. Furthermore, the ideal interface morphology for the ideal scattering has not yet been identified to date. A recent alternative solution to texturing is to use metal nanoparticle structures with low surface roughness to scatter light [23,37,59,71]. Noble metal (e.g. Au, Ag) nanoparticles have been the most studied type of MNPs, since it has been possible to produce them with good control of size and shape [12,40,72], as the particles are resistant to oxidation, and have strong plasmon resonances in the visible to near-IR region of the spectrum that can be easily tuned [9,16,73]. The optimized solution should provide effective light trapping keeping the cell film as flat as possible, in order to maximize both the photo-generated current and the operating voltage.

1.3 Surface enhanced Raman spectroscopy

1.3.1 Background

Surface Enhanced Raman Spectroscopy is a nanoscale phenomenon relying in relatively simple principles. The original substrates for SERS were electrochemically roughened metal electrodes such as reported by Fleischmann *et al.* in 1974 [74]. The interest of Fleischmann, Hendra and McQuillan in the study of species adsorbed on large-area oxide catalysts, led to the discovery of unusually strong and potential-dependent signals on electrochemically roughened silver electrodes, they attributed the observed effect to the increased surface coverage of pyridine on the electrode which seemed an appealing explanation for its simplicity [74,75]. However, the subsequent publications in 1977 by Jeanmire and Van Duyne [76] on one side, and Albrecht and Creighton [77] on the other, simultaneously clarified that the Raman cross-section *per* molecule oversized by far the one from the same molecule in solution, so the large intensity could not be accounted only for the increase in surface area. As a result, both groups proposed enhancement mechanisms based on electromagnetic and chemical effects, respectively, and Van Duyne coined the SERS acronym [76]. The understanding of electromagnetic effect in metallic surfaces was later (1979) established by Moskovits [78].

In the mid-1980s the SERS field witnessed a drawback due to the irreproducibility of substrates, which resulted in significant variations in SERS performance. A great review from Moskovits in 1985 offered the summary of the work developed at the time [79]. Thus, for the following years, SERS reached a *plateau*, and was not until 1997 that two independent works of Nie and Emory [80], and Kneipp *et al.*[81] gave renewed interest to the SERS research field. They proved the possibility, first suggested by Pettinger *et al.* in 1988 [82] (by demonstrating that rhodamine 6G (R6G) cross-section was competitive with that of an allowed electronic transition when adsorbed on silver), that single-molecule detection was possible by SERS. Hence, both groups reported a SERS spectra of individual molecules in specific conditions, isolating light emissions from a single nanoparticle aggregate (which the instrumental resolution prior to 1990s did not allowed) [81,83].

The improvements in Raman spectrometers with background light rejection based on filters instead of gratings, allowed researchers to work with reduced laser excitation intensities. In pair to Raman equipment improvements, the advances in nanoscience were equally important and catalyzed an explosion of new possibilities regarding SERS substrates design and fabrication. These developments led to an extension of SERS from a stimulating physical phenomenon to a robust and effective analytical technique available for scientists from various backgrounds such as physics, chemistry, materials science, biology and engineering, among others [84,85].

1.3.2 Basic principles of SERS detection

Raman scattering [86] is based on the inelastic scattering of a photon from a molecule which is excited to higher vibrational or rotational energy levels, resulting in a spectrum that reflects the energy differences between the incident and inelastically-scattered photons, allowing the unique identification of one or multiple “fingerprints” from molecular bonds. One of the difficulties associated with Raman spectroscopy is the small scattering cross section of many materials and, consequently, Raman signals can be inherently weak (one scattered photon per million incident) [87]. SERS is a surface-sensitive technique that enhances the Raman signal by molecules adsorbed on metal nanostructured substrates [75]. This technique has attracted intense interest since 1977 because it could produce 3 to 14 orders of magnitude enhancement in Raman signals [88,89]. The exact mechanism of the enhancement effect of SERS is still a matter of debate in the literature, however two mechanisms have been theoretically accepted to explain this effect: the electromagnetic (EM) [90] enhancement associated with LSPR and the so-called chemical enhancement (CE) [91] due to charge transfer mechanisms. The former arises from the interaction between an exciting light and metal nanostructures, leading to enhance local EM fields due to the resonant excitation of surface plasmon oscillations in the nanostructures (Figure 1.13). The resulting localized electric-field enhancement can lead to highly amplified Raman scattering signals at the surface of the nanostructures, resulting in an increase of the signals from molecules that have been adsorbed onto or are in the vicinity of the nanometer-sized metallic particles [92]. The local field enhancement is higher at the overlap of the near-field regions between adjacent nanoparticles, creating the so-called ‘*hot-spots*’[93], where usually the ideal spacing is in the range of 1–10 nm [94,95]. The latter mechanism can be attributed to charge transfer induced by the molecule-metal interaction [96,97]. Generally, its contribution to the enhancement factor (EF) is of the order of one to three orders of magnitude [98] and significantly smaller than the EM contribution, being the electromagnetic enhancement the common dominant mechanism for SERS. An in-depth review of the SERS mechanisms is beyond the scope of this thesis and can be found elsewhere [91,96–98].

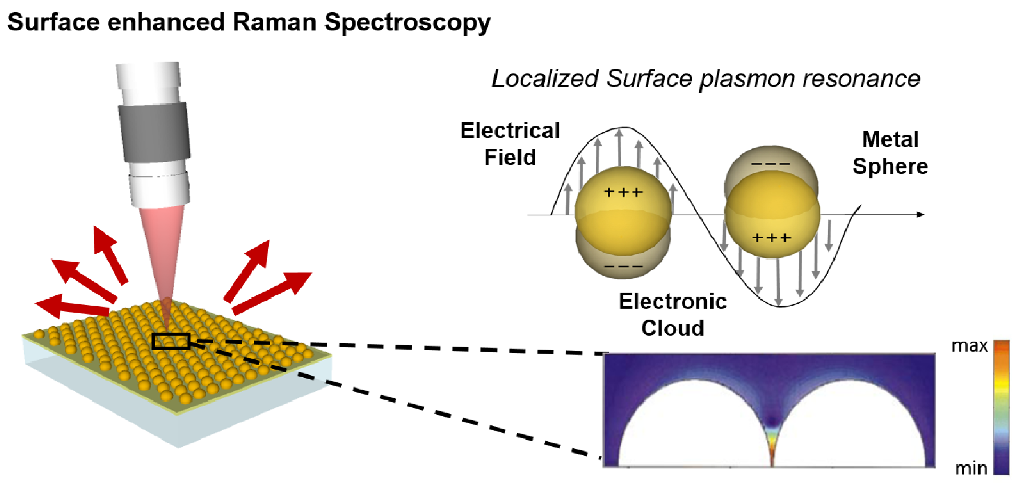

Figure 1.13 Illustration of SERS and of the LSPR effect. This consists in the collective oscillation of the conduction electrons in a MNP in resonance with the frequency of incident light. The colour plot at the bottom corresponds to the electric field intensity profile in the inter-space of a dimer with two Au nanospheres having a separation of 1 nm. The colour scale is logarithmic [99].

1.3.3 Cellulose based substrates

Cellulose is the most abundant biopolymer on Earth and is nowadays envisaged for several opto-electronic applications due to its unique set of advantages. Cellulose is biocompatible, biodegradable, 100% recyclable, lightweight, flexible, foldable and low cost (~10^{-3} cent/m^2) when compared with the most common flexible substrates (e.g. PET, PI) used in electronics which are above one order of magnitude more expensive [86,100,101].

Cellulose, mainly obtained from the skeletal component of plants, is an almost inexhaustible green material with an annual production of about 1.5 trillion tons [102]. The molecular structure of cellulose, $(C_6H_{10}O_5)_n$, is a polysaccharide consisting of a linear chain of glucose units linked together through β 1,4 glyosidic bonds by condensation reaction [103]. The cellulose chains are then organized into elementary fibrils (nanosized fibers), which aggregate into larger microfibrils and microfibrillar bands [104,105]. In microfibrils, the multiple hydroxyl groups on the glucose form hydrogen bonds with each other, holding the chains firmly together and contributing to their high tensile strength [106,107]. An in-depth review of cellulose materials, and fabrication methods, can be found in the work of Moon *et al* [108].

The area of bio-devices/sensors ascribes a high importance to paper substrates. From the healthcare perspective, point-of-care (PoC) tests, which are performed at or near the site of clinical care, provide unique opportunities for addressing healthcare issues in developing countries. The strengths of paper-based microfluidics and sensors are their low-cost, disposability and minimal external equipment requirements [109].

In the packaging area, the food and beverage industry are aligning their strategy with the consumers demands of more natural products with less additives, higher regulation, and quality control, to assure food safety. Intelligent sensors can impart packages with the capability to acquire, store and transfer data, communicate and carry out logic functions. Thereby contributing to increase consumer confidence in the products they eat and drink [110].

In view of the aforementioned exciting applications of paper materials for bio-detection, this thesis demonstrates the most researched technologies that allow such detection, using light-induced optical signals given by the analytes (probe molecules), based in SERS.

1.3.4 Cellulose based SERS substrates

The performance of the SERS technique strongly depends on the choice of the materials and structure of the SERS-active substrate. Ideal SERS platforms should not only exhibit strong signal enhancement with multiple electric-field *hot spots*, but should also present a uniformly distributed signal along the surface. With the advances of nanotechnology in the last decades, there are applications of SERS branched to new fields from environmental to medical care, art, clothing, security, among others [111–113]. The design of effective SERS substrates needs to cover many aspects besides having high SERS enhancement, which are intrinsically related to all sensor requirements for PoC applications such as: uniformity, reproducibility, shelf life, scalability and cost. SERS studies have largely benefited from the recent advances in the understanding of plasmonic concepts [114,115]. NPs made of noble metals, such as Ag or Au, became the most studied materials for SERS because of their stronger LSPR relative to other metals [92,116–118]. The research on nanostructures for SERS is mainly focused in improving the correlation between the NPs' properties and the resulting SERS signal intensities, since both the frequency and magnitude of the maximum field enhancement are strongly dependent on the shape, size and structure of the metallic material [12,92,119,120]. Generally, two typical routes have been pursued to improve SERS platforms, targeting single molecule detection: The most common approach is the optimization of the morphological properties of the self-assembled MNPs structures [92,101,121,122]. The other one is the development of their supporting material (i.e. the substrate).

The surface onto which the nanomaterials are placed can vary from rigid [e.g. glass, Si wafers (>~200 μm thick) and porous alumina] to flexible substrates (e.g. paper, cardboard substrate, cotton, plastic, silica sheets and tape) [92,113,123,124]. The traditional rigid substrates have several drawbacks as practical SERS substrates, since the collection efficiency and manipulation of solid samples is difficult. Flexible 3substrates for SERS can present several advantages over conventional rigid substrates, in terms of cost and processability, achieving Raman signal enhancements (EF ≈ 10^5-10^7) comparable with the conventional rigid planar supports [92,113,124–135]. Such substrates have the advantage of being able to collect analytes by soaking, which allow them to be used for example in contact with the human body and food in packaging, as they can be wrapped around curved surfaces [136,137], opening doors for the next generation of bio-medical optical sensing. Table 1.1 presents a summary of the principal features of the main SERS platforms.

Table 1.1- Advantages and disadvantages of main SERS substrates [112,138–142]·

Surfaces	Advantages	Disadvantages
Silicon Wafer	• Low background within the Raman fingerprint region (only the characteristic peaks associated with the Si crystal vibrations appear).	• Expensive; • Fragile (need to be handled with care); • Rigid (thickness >~200 µm).
Glass	• Very low SERS background; • Readily integrated into other analytical systems; • Less expensive than Si substrates.	• Fragile; • Rigid.
Paper based	• Available; • Inexpensive; • Made of renewable resources; • Thinness, lightweight; • Biodegradability; • Abundant storage capability; • Flexible (wipe over a surface to collect the analyte); • Cellulose fibres are compatible with biomolecules (important for biosensing).	• Analyte solution spreads out over a large area due the wicking ability of cellulose, so the paper needs to be modified to have varied degrees of hydrophobicity; • Dispersion of the NPs presents difficulties for controlled array formation; • Fragile.

Among all the flexible substrates, there is a currently growing interest towards paper-based SERS substrates, mainly due to the paper composition and cost, which provides flexibility, portability and biodegradability. In fact, paper has already been widely used as a low-cost platform for bio-analytical devices such as colorimetric, biochemical fluorescence electrochemical sensors, among others [127,129,130,143–151]·

1.3.5 Solution processed cellulose SERS substrates

The fabrication methods of paper-based SERS substrates can be divided in two classes: chemical methods via patterning from a colloidal solution of metal NPs (e.g. inkjet and screen printing [127,143,145,146,152–154], deposition by drop-casting [155,156], filtration [157], in-situ growth [158–161]) or physical methods via material deposition under vacuum (e.g. vapor deposition of ultra-thin metallic layers [117], laser induced annealing method [162]). We start here by overviewing the first class of solution-based processes.

Inkjet and screen printing technologies are probably two of the most popular methods to fabricate plasmonic devices on paper, just by direct printing nanoparticle colloidal solutions [127,143,145,146,152–154]. Their major advantage is the ability for printing arrays of SERS-active regions of any shape, which makes these techniques simple and affordable [112]. White's group reported the preparation of SERS-active substrates [127,153,154,157] on chromatography paper prepared by inkjet printing using a low-cost commercial piezo-based inkjet printer. By printing Ag NPs onto one end of the paper, the remaining part of the paper was used as a swab to collect the analyte's molecules directly from a large-area surface, enabled by the flexible nature of the paper-based SERS device (Figure 1.14 1). Using these novel lateral-flow paper SERS devices, they achieved detection limits as low as 95 fentograms of R6G[154]. More recently, Zhigao Dai *et al.* [131] presented a study using an inkjet printing technique to fabricate a SERS substrate based on Au NRs inks on printed paper. The neighbouring nanoclusters of Au NRs, aligned side-to-side, were formed on office paper with favourable SERS properties [131].

Screen printing is another printing technique that has been used to fabricate SERS substrates by printing SERS active nanoparticles arrays on filter paper using colloids solutions [146]. However, the SERS signal of 5 µL R6G (1×10^{-9} M) recorded on paper was weaker than those from the glass and glass fibre plate (Enhancement factor (EF) = 4.4×10^{6}). Sample delivery was not well controlled on filter paper, thus diluting the sample and resulting in weak SERS enhancements. Although the printing method offers interesting features for the fabrication of flexible plasmonic devices, it requires agents for the viscosity control of the nanoparticles' ink [146]. Hence, printing can promote aggregation and background signals reducing the capability of detecting the analyte. Moreover, it is generally changeling to achieve simultaneously a good uniformity and high concentration of NPs deposited on paper when they come from solution phase.

An innovative method reported by Polavarapu *et al.* [128] was the development a "*pen on paper*" approach to produce efficient and reproducible SERS substrates in a highly versatile way. With this method, a fountain pen filled with metal NPs ink was used to directly write plasmonic SERS areas on paper, made of Au or Ag nanospheres and Ag nanorods, without the need of any special training or equipment (Figure 1.14 2). The EF of the Ag NPs substrates was calculated using 10 µL droplet of malachite green (MG) as Raman active probe (1×10^{-6} M) and the obtained values were 2×10^{5} and 1.5×10^{5} at 532 nm and 785 nm, respectively.

Nevertheless, possibly an even simpler approach is the drop-casting method. This type of process generally requires lower energy consumption and amount of material. When drop-casting the NPs the wicking ability of cellulose causes the liquid to spread over a large area, which reduces the SERS signal and reproducibility. Limiting the hydrophilicity of the paper to a defined area, making it possible to concentrate the NPs over a pre-patterned area and consequently to obtain high SERS enhancements, surpasses this drawback. Oliveira *et al.* [156] reported the fabrication of office paper SERS substrates using Ag nanostars (NSs) drop-casted in wells patterned in the paper using printed wax. These substrates exhibited a high reproducibility with good uniformity and high SERS enhancement (EF~10^7). Furthermore, contrary to other methods that require a high concentration of nanoparticles to achieve a high density of near-field *hot spots*, the tip-shaped anisotropic morphology of Ag NSs avoids the need of high NP's concentration (Figure 1.14 3)).

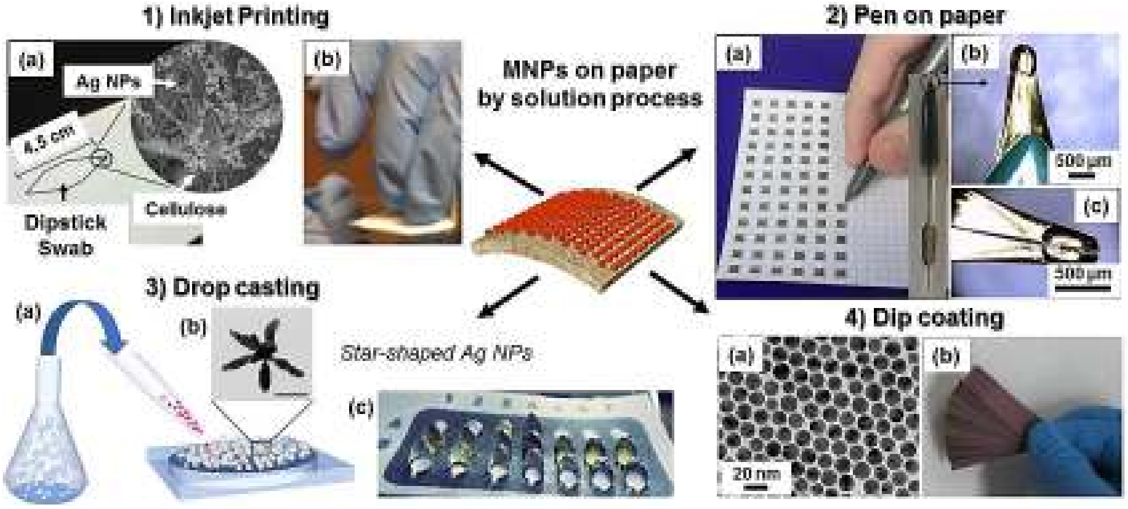

Figure 1.14 Methods for decoration of paper substrates with plasmonic nanoparticles by solution processes. 1) Ag NPs printed onto paper by inject printing technology [154]. 2) Impregnation of Au nanospheres, Ag nanospheres and Au nanorods, using a pen filled with a colloidal solution to directly write SERS arrays on paper substrates [128]. 3) Schematic representation of the fabrication process of the plasmonic SERS paper substrates by drop-casting colloidal solutions of Ag nanostars (inset shows the TEM of a single nanostar) [156]. 4) (a) TEM image of oleylamine-capped Au NPs, (b) Photograph of Au NP doped filter papers by the dip coating method [135].

Another simple process that has been applied to fabricate paper coated with metal NPs is by *dip-coating* (i.e. "soaking") paper substrates into solutions having colloidal metal nanostructures with different morphologies (e.g. nanoparticles, nanorods, bipyramids) [113,142,143,160]. Using this method, nanoparticles are uniformly deposited onto the paper by simply dipping the substrate into the nanoparticle's solution of interest, followed by drying. This process provides high sample collection efficiency, does not require complex fabrication methodologies and allows the tunability of the NPs morphology that are deposited on the substrate. However, most of these approaches involve the attachment of NPs from aqueous dispersions, which requires either nanoparticle's solutions in a rather high concentration, like for the printing method, or long dipping times (typically 24–48 hours) to obtain a sufficiently high loading [126,163]. Zheng *et al.* [135] developed a fast fabrication based on a robust and recyclable dip-catalyst. The Au NPs were impregnated into a filter paper by simply dipping the paper into a concentrated NP colloidal dispersion in toluene, followed by drying using a hair-dryer (see Figure 1.14 4). This process was repeated five times in order to achieve a close packed Au NP assembly [135].

Other methods explore the modification of cellulose with different functional groups [164]. For example, the aldehyde groups can be used to help the synthesis of metallic Ag. These types of paper-based substrates are included in the category of *in-situ* growth [158,160,161,165,166]. Other examples use reductive agents such as glucose to produced 3D SERS paper strips containing Ag NPs. Although an adequate concentration of NPs for SERS signals can be obtained, the background signal of residues from the reagents used for the *in-situ* growth of Ag NPs, and the fast NPs oxidation rate, have quenched the interest for these types of solution methods.

1.3.6 Physically processed cellulose SERS substrates

The physical methods typically employed for the patterning of metal NP arrays on paper are sputtering, pulsed laser (PLD) and e-beam deposition [92,130]. However, there are still few contributions investigating deposition by PLD and laser induced annealing, because generally they require high power lasers [162], elevated temperatures for fine control of the shape and organization of the nanoparticles, which are incompatible with paper-based substrates. Although lithographic methods also can be used to precisely define the morphologies and sizes of NPs, this approach has major drawbacks, such as a high patterning time and elevated costs, which limit its extensive use in macroscopic scale systems [167,168].

The work developed in this thesis has pioneered a simple, uniform, reproducible and large scale one-step method to deposit metal NPs on cellulose-based substrates [92,101]. Despite the many advantages of using paper as SERS substrate, the most challenging requirement is the need to obtain a uniform and controlled distribution of plasmonic nanostructures on these substrates. The uniformity of the nanostructures on paper substrates produced by thermal evaporation greatly contributes to the high reproducibility of SERS, as the Raman laser spot covers a range of tens of microns that contains several thousands of particles. Thus, a large ensemble of NPs affects the resulting signal.

Paper-based SERS platforms are easily fabricated and present numerous opportunities to integrate with PoC applications. As previously mentioned, these diagnostic assays are associated with specific requirements such as low-cost, robustness, portability, requirement of few reagents and ease of use.

Chapter 2

Fabrication and Characterization Techniques

Chapter 2 summarizes the procedures and processes involved in the production and characterization of nanostructures composed of Ag NPs. The fabrication focus is given to the thermal evaporation assisted by electron beam, where a thin layer of metal is deposited directly on the substrate. This process is followed by a solid-state dewetting process, which consists in a thermally-induced morphology transformation from a thin film to an array of NPs. A novel procedure, involving a one-step methodology resulting in the direct arrangement of individual nanoparticles, with good control of their size and shape, without any post-deposition thermal procedures is presented. In addition, for structures that require a post-annealing process, a rapid thermal annealing method is employed that yields highly reproducible and uniform plasmonic surfaces within a very fast annealing time when compared to other commonly employed annealing processes.

Afterwards, other fabrication conventional techniques are described, namely sputtering and Plasma-enhanced chemical vapour deposition, to produce thin oxide and Si layers, respectively, both used in Si solar cell devices. The applicability of such Ag NPs in SERS and Si solar cells is then presented.

This is accomplished by brief introduction to set of equipment's used to perform the structure, morphology and optical and electrical characterizations of the nanoparticles, films and layers structures and devices fabricated along this thesis.

2.1 Nanoparticles fabrication

Currently, the most frequent method for producing MNPs with nanoscopic controlled geometry and inter-particle distance is employing advanced lithographic processes, such as e-beam litrography [167]. However, this method has crucial drawbacks such as high patterning time and elevated costs, which limits its extensive use in macroscopic scale systems. Alternative large scale processes such as chemical synthesis [143,169,170], physical deposition with post-deposition annealing (PDA) [12] or template and electrodeposition [89] are also commonly applied. With these latter techniques, several processing steps are required, despite the fact that PDA, for example, requires elevated temperature conditions. In this study, e-beam evaporation was used as the principal technique to deposit thin metal layers to produce MNP structures. This physical process allows a uniform, reproducible and large scale deposition of ultra-thin layers on the entire surface of substrates with virtually any area. *In situ* or with a post-annealing process, the MNPs formed by thermal evaporation assisted by electron beam result in a dense array of individual nanoparticles with good control of their size and shape.

2.1.1 Metal thin films deposition by electron-beam evaporation

Thermal evaporation assisted by electron beam is one of the most widely used methods to deposit metallic TFs. This deposition technique was used to deposit thin layers of silver to form the metal nanoparticles, as well as for the deposition of the back metal contacts used in the TF silicon solar cells. The technique consists essentially on heating (by the electron bombardment) a material up to its vaporization point, allowing the deposition of the evaporated material onto a substrate placed close to the source material (see Figure 2.1). The electron beam is generated in an incandescent filament by thermoionic emission. The electrons are accelerated by a potential difference (in the order of kilovolts) towards the crucible containing the material to evaporate. Since the electron beam can be focused in to a point, it can reach a very high temperature, while the crucible is water cooled, allowing the deposition of materials with very high melting points such as ceramics. The electron beam is deflected towards the surface of the source material by a magnetic field. The heating process is performed under high vacuum to increase the mean free path of vaporized molecules and reduce contamination of the deposited TF. Besides, since the crucible is cooled with water, the contamination is very low.

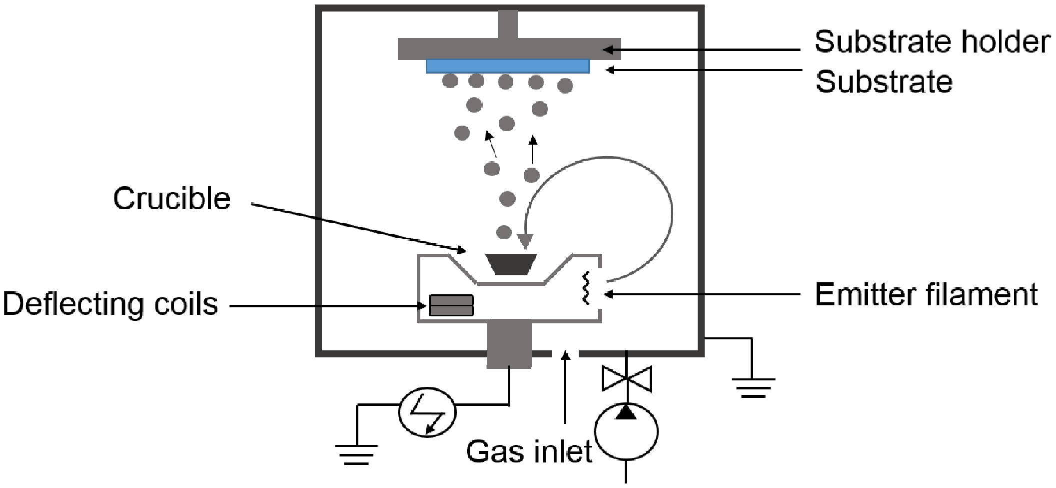

Figure 2.1 Schematic of a thermal evaporation system assisted by electron beam.

Ag films were deposited using a home-made e-beam system existent in the clean room facilities of CENIMAT (Figure 2.2). Silver was the material of choice for MNPs fabrication, due to its high radiative (scattering) efficiency and the lowest imaginary permittivity in the Vis and NIR range, among the noble metals commonly used in plasmonics [40]. For all the samples presented in this study, the evaporation of the Ag TF was carried out with a base pressure (p) of 10^{-6} mbar, a working pressure of 10^{-5} mbar, and a deposition rate of 0.07 nm/s. A calibrated quartz crystal sensor inferred the thicknesses and growth rate of the films.

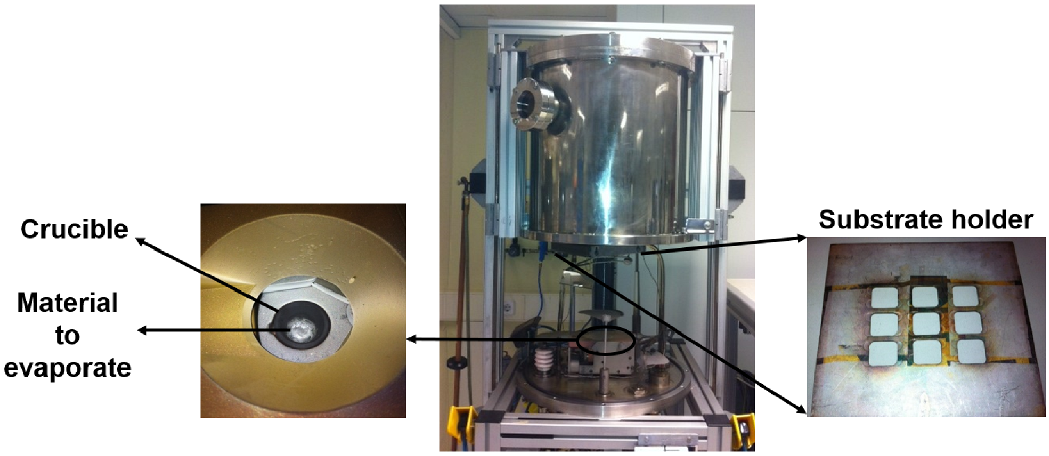

Figure 2.2 Homemade thermal evaporator assisted by electron beam used for the deposition of silver thin layers.

2.1.2 Solid-state dewetting

Solid-state dewetting is a simple and industrially scalable process capable of morphologically transform (by self-assembly) a continuous TF in islands or droplets due to a thermal treatment (see Figure 2.3). Dewetting can occur at temperatures well below the melting point of a material, since films with thickness of a few nanometers are generally metastable in the as-deposited state, and will spontaneously dewet when heated to temperatures at which the mobility of the constituent atoms is sufficiently high to provide effective mass transport. The threshold temperature at which dewetting is observed decreases with decreasing film thicknesses and with the material melting point temperature [62].

The driving force for dewetting arises from the minimization of the total free energy of the interfaces between air, film, and substrate. The energy minimization condition for an island with an isotropic surface energy per unit area, γ_{LG}, supported on a rigid substrate with surface energy per unit area γ_{SG}, gives an equilibrium shape of a spherical cape with contact angle θ, defined by the Young equation:

$$\gamma_{SG} = \gamma_{SL} + \gamma_{LG} \cos\theta \tag{2.1}$$

where γ_{SL} is the surface energy of the island-substrate interface. A useful parameter for gauging wetting is the spreading parameter S,

$$S = \gamma_{SG} - \gamma_{SL} - \gamma_{LG} \tag{2.2}$$

In general, if $S > 0$ the film is stable and will not dewet; otherwise, the film is metastable and will dewet when the kinetic processes are sufficiently high.

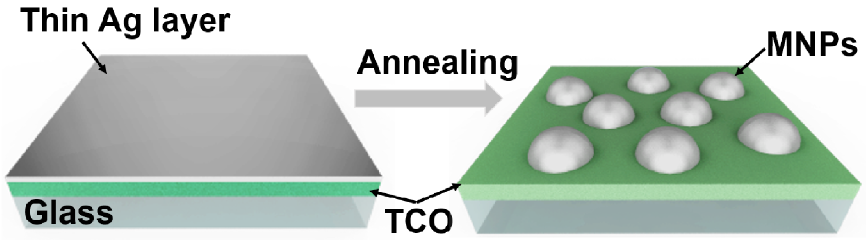

Figure 2.3 Schematic drawing of the solid-state dewetting process on a TCO-coated glass substrate.

2.1.3 Thermal treatment for Ag NPs formation

The thermal annealing, in which self-assembled MNPs are formed by SSD from an Ag layer, was varied depending on the substrate, desired shape and size, as well as the application of the Ag NPs. Nevertheless, suitable substrate heating is imperative to favor material surface diffusion during or after the deposition, to avoid worm-like metal structures [12,171]. In this study, two different thermal annealing processes were employed. For light trapping applications in solar cells, we are interested in forming large (>100 nm) and uniformly shaped Ag nanoparticles, which requires elevated annealing temperatures (~500 °C) to enable the surface diffusion of the Ag material, and the formation of more energetically favored large particles by coalescence of smaller ones [12,172]. For this purpose, RTA experiments were carried out. On other hand, for plasmonic SERS substrates the required sizes and inter-particle distances are much smaller than for Si cells, so a low-temperature *in-situ* nanoparticle formation method was applied without post-annealing [173]. The low-temperature nanoparticle formation method developed in this study is largely applicable to thermal-sensitive substrate materials, for instance cellulose-based substrates which would not be compatible with standard post-annealing dewetting methods carried out at high temperatures (300–500 °C) [12,39].

2.1.3.1 Thermal treatment for Ag NPs formation to plasmonic cellulose SERs devices

CENIMAT/i3N group has recently developed a simple, uniform, reproducible and scalable one-step method to deposit metal nanoparticles on thermal-sensitivity (e.g. polymeric) substrates [117,171,173]. The methodology employed (thermal evaporation assisted by an electron beam, section 2.1.3) results in the direct arrangement of individual nanoparticles, with good control of their size and shape, without any post-deposition thermal procedures [92]. Metal nanoparticles are formed *in situ* during the thermal evaporation of the metallic material onto the substrates, with up to 20 x 20 cm^2 area, heated at only 150 °C. The uniformity of the nanostructures produced by the thermal evaporation greatly contributes to the high reproducibility of SERS, which will be further discussed in chapter 4.

2.1.3.2 Thermal treatment for Ag NPs formation for light trapping in Si solar cells

The post-deposition annealing, in which self-assembled MNPs are formed by SSD from an ultra-thin Ag layer, was performed using a Rapid Thermal process (AS-One 100) (Figure 2.4). This system is a high-speed furnace which allows heat treatments up to 1500 °C with a heating rate up to 200 °C/s. The system includes a processing chamber with vacuum capability and allows annealing from vacuum to atmospheric pressure. The annealing atmosphere can be air, nitrogen, forming gas or argon. The halogen tubular lamp furnace is installed on the topside of the reactor and anneals the substrate through the quartz window.

RTA is an advantageous method to yield highly reproducible and uniform plasmonic surfaces in few minutes, which is a short annealing time when compared with that (~1 h) commonly employed annealing processes (e.g., using a tube furnace) [174,175]. It is known that the rate of NP formation decreases with the increase of the precursor film thickness, but can it be accelerated by increasing the annealing temperature [176,177]. For light trapping applications in SC, we are interested in forming large (>100 nm) and uniformly shaped Ag NPs, which requires elevated annealing temperatures (~500 °C) to enable the surface diffusion of the Ag material, its migration and the formation of more energetically favored large particles by coalescence of smaller ones [12]. The produced Ag NPs used in the silicon solar cells were annealed at 500 °C in an nitrogen (N_2) atmosphere with a heating rate of 150 °C/s, maintaining the annealing temperature for 10 min. Wherever, a systematic study of the temperature, time and heating rate was discussed in the chapter 3.

Figure 2.4 As-One 100 rapid thermal process existent in CEMOP/CENIMAT.

2.2 Ag NPs characterization techniques

The Ag NP structures were characterized using a broad range of techniques to study their morphological and optical properties. Relevant details about the characterization techniques used throughout this work are given below.

2.2.1 Morphological characterization

2.2.1.1 Scanning electron microscopy (SEM)

Scanning electron microscopy (SEM) can provide high-resolution images of the material surface at the nanometre scale. The microscope includes a source of high-energy electrons (thermoionically emitted from a tungsten or lanthanum hexaboride cathode or, alternatively, generated via field emission) which are accelerated towards an anode; and a condenser system, composed by electromagnetic lenses to focus the electron beam into a fine probe (sized 1 nm to 5 nm) that impinges on the specimen. To obtain an image by SEM, a highly energetic electron beam is directed at the sample and several interactions will occur, i.e. absorption of electrons by the sample, reflection of primary (backscattered) electrons, emission of secondary electrons and emission of electromagnetic radiation. The conventional SEM image is formed by the detection of the secondary electrons emitted by the sample. However, different detectors can be used to make the analysis. When the primary electron beam is focused on the material, the electrons lose energy by recurrent scattering and absorption within a teardrop-shaped volume of the specimen known as the interaction volume, which extends from less than 100 nm to around 5 µm into the sample. The size of the interaction volume depends on the beam accelerating voltage, the atomic number of the specimen and its density. Secondary electrons (SE) are defined as electrons emitted from the specimen with energy less than 50 eV, and are generally produced due to interactions between energetic primary electrons and weakly bound conduction electrons in the sample. An important characteristic of secondary electrons is their shallow sampling depth, a direct consequence of the low kinetic energy that they have. Backscattered electrons (BSE) are high-energy electrons and can escape from a much larger volume than SE. The signal intensity will depend on the average atomic number of the specimen but is almost independent of topography.

Surface and cross-section SEM images observations produced in this study were performed using a SEM focused ion beam (FIB) Cross-Beam Auriga system equipped with energy dispersive X-ray spectroscopy (EDS) measurements, from Carl Zeiss existent in CENIMAT (Figure 2.5). The samples were mounted on aluminum stubs with carbon tape and coated with a 10 nm thick Au/Pd film in a Quorum Q150T ES sputtering system. For the cross-section analysis, a focused ion beam (FIB) of Ga^+ ions was accelerated to 30 kV at 50 pA at a 54 º, with the samples previously coated with a sacrificial layer of Au/Pd (30 nm), achieving an etching depth round 1 µm.

The statistical parameters of the NPs (size and surface coverage (SC)) were derived from the digital analysis of the SEM-based images, which was conducted using the ImageJ [178] software package. The crucial point of the analysis was the determination of the contrast threshold that defines the distinction between the particles and the background. The accuracy of this approach was estimated at two pixels. The longest in-plane axis of the MNPs is called particle size (D), for simplicity.

Figure 2.5 Zeiss Auriga CrossBeam system – SEM-FIB in CENIMAT.

2.2.1.2 Atomic force microscopy (AFM)

Atomic force microscopy, or AFM, is a high-resolution three-dimensional imaging technique that can, under some conditions, achieve atomic resolution, with the advantage that it requires less sample preparation than SEM and measurements can be performed in air or liquid environment. In AFM, a nano-metric probe is approached to a surface and used to scan it. The position of the probe is monitored using a detection system (commonly, a beam of light reflected by the probe to a position sensitive photodiode) and forwarded to a feedback system, which can raise or lower the probe in order to assure that the distance probe-sample is constant. Each time the probe encounters an obstacle – a change in topography – its behavior or position is affected, and the AFM will record that change, allowing to map a surface. In fact, the majority of AFMs function in a ‘tapping’ mode also named alternated contact (AC) mode, a mode that the probe, instead of being deflected against a surface, is oscillating above it, with the alterations in the oscillation generated by the surface, helping to create surface images of the object of study.

The AFM analysis of surface morphology and calculation of root-mean-square roughness (RMS) on the different substrate surfaces (prior to NPs deposition), and the average height of the subsequent self-assembled MNPs, was performed using an Asylum MFP-3D AFM system in CENIMAT (Figure 2.6). Measurements were performed in alternate contact mode in air, using commercially available silicon AFM probes (Olympus AC160TS; k = 26 N/m, f0=300 kHz). Images were acquired at a scan rate of 1 Hz and plane fitted. The same sample was scanned at least in three different regions to confirm that the NP distribution is homogeneous throughout the film.

The software Gwyddion to access the height distributions of the Ag MNPs in each sample was used to analyze the images. The nanoparticles were marked by threshold using the grain analysis tool of the software.

Figure 2.6 Asylum MFP3D atomic force microscope system existent in CENIMAT.

2.2.2 Optical characterization

Optical characterization can be used to assess the NPs physical properties (size, shape and medium) and their optical performance. Particularly, it is used to measure the LSPRs' spectral positions of the structures and, hence, the wavelength range in which they can be of use either in the solar cells or the matching with the laser in SERS measurements. Another important parameter determinant to the optical performance of a sample, in terms of light trapping in solar cells, is the diffuse reflection which indicates the amount of scattered photons that has an increased probability to be absorbed in the solar cell, due to their enhanced optical path length.

The optical properties of the Ag NPs were measured using a Lambda 950 double beam UV–Vis-NIR spectrometer (Figure 2.7) equipped with a 5.9-inch integrating sphere. Integrating spheres are essential accessories for measuring the transmittance or reflectance of any sample that scatters light.

This system has two radiation sources, a deuterium lamp (DL) for the UV range and a halogen lamp (HL) for the Vis and NIR ranges, with wavelength range extending from 175 to 3300 nm. The spectral bandwidth in the UV/Vis range is from 0.05 to 5.00 nm, and from 0.2 to 20.00 nm in the NIR range. A photomultiplier type R 6872 is used as a detector for the UV/Vis range. For applications in the NIR range the system is automatically switched over to a PbS detector type OTC-21-73.

This technique was mainly used to obtain the integrated measurements of the total and diffuse reflectance (R_{TOT} and R_{DIF}, respectively) as well as the total and diffuse transmittance (T_{TOT} and T_{DIF}). The parasitic light absorption within the NPs (*Abs*) was calculated as:

$$\mathrm{Abs} = 100\% - T_{TOT} - R_{TOT} - \mathrm{Abs}_{Substrate} \tag{2.3}$$

Figure 2.7 Lambda 950 double beam UV–Vis-NIR spectrometer system existent in CENIMAT.

2.3 Oxide thin films deposition

A variety of deposition techniques can be used to fabricate oxide TF. In this study, sputtering was used as the main technique. Sputtering deposition is a widely used technique for the deposition of oxide materials, with no intentional heating. An extremely important advantage of this technique is the fact that the TF ensues a composition very close to the used target, besides the good uniformity, reproducibility and adhesion.

2.3.1 Magnetron sputtering

Sputtering is a physical vapor deposition (PVD) technique where atoms or molecules are removed from a “target" that is a source onto a "substrate". Essentially, sputtering consists on the bombardment of a target with highly energetic ions created due to ionization of gaseous species, which by transfer of momentum remove atoms from its surface. The sputtered species are directed through vacuum to a substrate by an electric field. To generate the electric field, the target (cathode) is connected to the external source of excitation (in this case the generator R.F.), while the chamber (including the substrate) is connected to the ground. The highly energetic species needed for target bombardment are obtained by ionization of an inert gas, typically argon due to its low cost and high impact section (high ionic radius). In order to increase the erosion efficiency of the target, and consequently the rate of deposition, the plasma can be confined to the latter by the effect of magnetic fields, using magnets (magnetron), thus creating a higher density of ionized species.

In magnetron sputtering, the plasma is confined to a region close the target surface by a magnetic field, which is created due to strong magnets placed behind the target. This simultaneously reduces the substrate bombardment by electrons and increases the probability of ionization of neutral gaseous molecules, which is transduced in higher sputtering and growth rates.

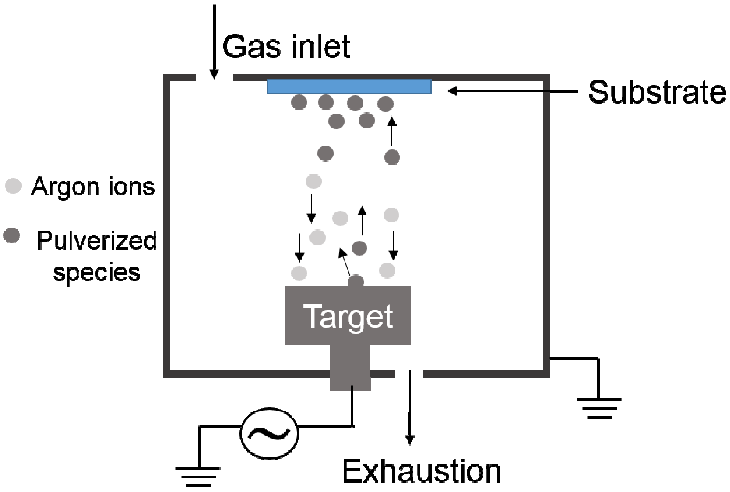

Figure 2.8 Schematic of a sputtering deposition system.

The RF magnetron sputtering system used in this work is a homemade system (Figure 2.9). In this system, different thin oxide films [ZnO, AZO (ZnO:Al2O3; 98:2 wt %), GZO ($ZnO:Ga_2O_3$; 98:2 wt %) and IZO ($In_2O_3:ZnO$; 98:2 wt %] were deposited by RF magnetron sputtering (P = 13.56 MHz) at room temperature. Prior to deposition, pre-sputtering (sputtering with the shutter closed to prevent deposition) was performed for 15 min to assure TF reproducibility. The exploratory work of these types of oxides was made and published previously by our laboratory [58,61,179,180].

Figure 2.9 Homemade magnetron sputtering system used for the deposition of oxide thin layers.

2.4 Complementary characterization

2.4.1 X-ray diffraction (XRD)

XRD is a non-destructive powerful characterization technique to determine a material's structure; whether it is amorphous or polycrystalline, which phases are present and if any preferential crystallographic orientations exist. When a monochromatic x-ray beam is directed at a material its photons can be either absorbed or dispersed by the atoms. For certain directions the dispersed waves are in phase, that is these interfere constructively, resulting in a diffracted beam with a direction that is dependent on the structural properties of the material. For a given x-ray radiation of wavelength (λ), with a value close to the inter-planar spacing (d_{ip}), that reaches the material with a certain incident angle (θ); constructive interferences occur when the phase difference between the waves dispersed by the distinct atomic planes are multiples (n) of the wavelength (λ). This phenomenon can be described by Bragg's law : $n\lambda = 2d_{ip}\sin\theta$. By varying 2θ (the diffraction angle) and measuring the diffracted beam intensity, which depends on the number of atomic planes equally spaced, a difractogram is obtained and it can be compared with a database to identify the sample's structure.

In this work XRD was used to analyze the paper substrates and the crystallinity of the ZnO seed layer and ZnO NRs produced on glass and cellulose substrates. The measurements were performed using a Panalytical X'Pert PRO MRD X-ray diffractometer (Figure 2.10) diffractometer existent in CENIMAT, in Bragg-Brentano ($\theta/2\theta$ coupled) geometry with Cu Kα line radiation (λ=1.5406 Å) and varying 2θ between 10 and 90°(and in a higher magnification from 30° to 40°), with a scanning step size of 0.016 º.

Figure 2.10 Panalytical X'Pert PRO diffractometer system existent in CENIMAT.

2.4.2 Simultaneous Thermal Analysis (STA)

STA (Simultaneous Thermal analysis) refers to the simultaneous thermogravimetric (TGA) and differential scanning calorimetric (DSC) measurements of a sample in a single instrument. In this system it's possible to test conditions perfectly identical for the TGA and DSC signals (same atmosphere, gas flow rate, vapor pressure on the sample, heating rate, thermal contact to the sample crucible and sensor, radiation effect, etc.). Furthermore, sample throughput is improved as more information can be gathered from each test run.

DSC is a technique that can be used to demonstrate the energy phenomena produced during heating (or cooling) of a substance (or a mixture of substances) and to determine the changes in the enthalpy and specific heat and the temperature at which these occur. For cellulose analysis is used an aluminum crucible that is placed in the DSC system together with an empty reference crucible. By applying a controlled temperature program (heating or cooling at constant rates), caloric changes can be measured. DSC measures the change of the difference in the heat flow rate to the substance and to a reference material when they are subject to a controlled temperature program. In TG technique the mass of a sample of a substance is recorded as a function of temperature according to a controlled temperature program.

In this work DSC and TGA were used to analyse the material stability of the cellulose based substrates during the nanostructures formation process. The measurements were performed using a simultaneous thermal analyzer (TGA-DSC - STA 449 F3 Jupiter) from Netzsch (Figure 2.11). Approximately 5 mg of sample was loaded into a closed aluminum crucible and heated from room temperature to 550 °C with a heating rate of 5 °C min^{-1}, in air.

Figure 2.11 TGA-DSC - STA 449 F3 Jupiter system existent in CENIMAT.

2.5 Fabrication and characterization of SERS devices

2.5.1 Raman measurements

Raman spectroscopy is a technique based on the inelastic scattering of monochromatic light, usually from a laser source, which provides chemical information. When light interacts with a sample, it excites its atoms/molecules, inducing oscillating dipoles and it is usually scattered without any change in energy, which is known as elastic or Rayleigh scattering. However, usually for 1 in each 10^6 reemitted photons, the frequency is shifted, known as inelastic or Raman scattering. The shift in frequency can be a consequence of part of the photon's energy transferred to the Raman-active vibrational mode, being the resulting frequency of scattered light reduced – Stokes scattering. In other cases, a photon is absorbed by a Raman-active molecule which is already in the excited vibrational state. Consequently, the excessive energy of this excited Raman-active mode is released, and the resulting frequency of scattered light increases – Anti-Stokes scattering (see Figure 2.12).

Because molecules vibrate at a particular set of frequencies, these changes provide information about vibrational, rotational and other low frequency transitions in molecules. Hence, they are specific to the individual molecules, giving a *fingerprint* Raman spectrum of the material.

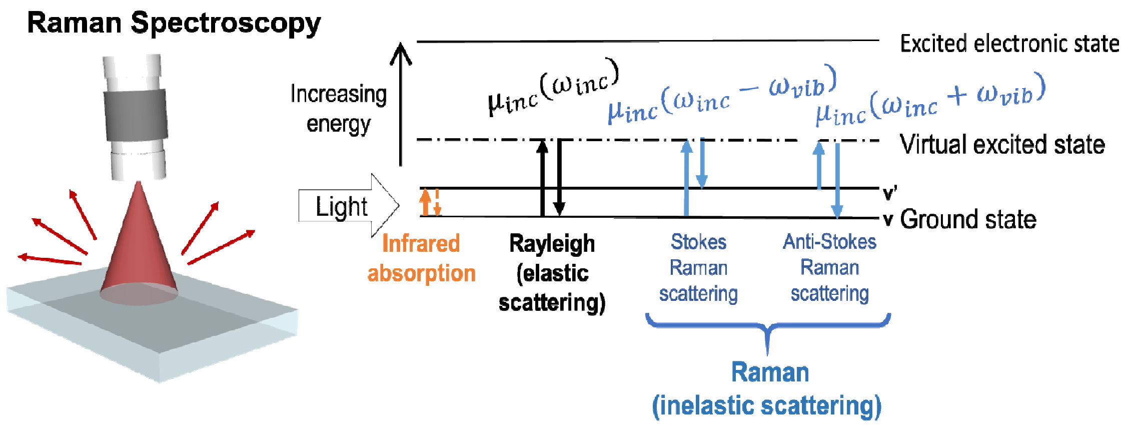

Figure 2.12 Schematic of Raman spectroscopy and energy diagram representing (*from left to right*) the infrared absorption, elastic Rayleigh scattering and the inelastic anti-Stokes (*left*) and Stokes (*right*) Raman scattering with $\boldsymbol{\omega}_{\mathbf{inc}}$, $\boldsymbol{\omega}_{\mathbf{inc}}\pm\boldsymbol{\omega}_{\mathbf{vib}}$ and $\boldsymbol{\omega}_{\mathbf{vib}}$ referring to the frequencies of the incident light, the Raman scattered light, and the molecular vibration, respectively.

Micro-Raman spectrometers, were non-destructive, microscopic, chemical analysis and/or imaging is required, can rapidly characterize the chemical composition and structure of a sample, whether solid (particles, pellets, powers, films, fibers), liquid (gels, pastes) or gas. Little or no sample preparation is required, and it is a label-free technique, which reduces the potential for artifacts. It is possible to analyze samples multiple times and to generate correlative and complementary information using downstream techniques.

In this work, Raman measurements were carried out in a Horiba - Jobin Yvon Labram 300 Raman Microscope located at REQUINTE and a Renishaw InVia Qontor Confocal Micro-Raman Microscope located at CEMOP (Figure 2.13), both equipped with an air-cooled CCD detector and a HeNe laser operating at 17mW and at 632.81 nm. The scattered light is passed through a solid edge filter (Horiba) for the removal of Rayleigh-scattered light in the region observed and provides a high throughput (90%–95%) for Raman lines. The spectral resolution of the spectroscopic system is 4 cm^{-1} and the wavenumber for each point is 0.5 cm^{-1}. The laser beam was focused with a 50× Leica objective lens (N10.6 LMPLAN FL N). The laser power at the surface of the samples was fixed with the aid of a neutral density filter (660 μW) incident laser power on the surface of the sample). All measurements were performed with a sampling of 5 scans and an integration time of 25 s, to reduce the random background noise from the detector, without contributing to the acquisition time. Triplicates were taken of all spectra. The 521 cm^{-1} peak of a silicon wafer was used between the different Raman sessions to calibrate the spectrograph for possible fluctuations of the Raman systems. All SERS spectra were recorded at room temperature. After measurement and data accumulation, a linear baseline subtraction and Lorentzian decomposition of the spectra was performed to identify the parameters of the peaks (height, area, center and width) associated with selected Raman vibrational lines (e.g. 1360 and 1509 cm^{-1} when using Rhodamine 6G as analyte).

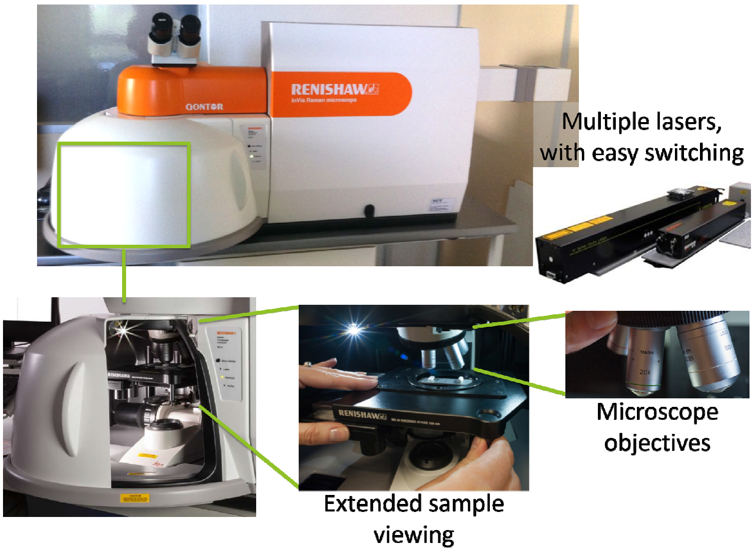

Figure 2.13 Renishaw InVia Qontor Confocal Micro-Raman microscope –existent in CEMOP.

2.5.2 Preparation of samples for SERS measurements

To characterize the SERS activity of the substrates, a drop of R6G was cast onto the plasmonic substrates. R6G was chosen as a non-resonant model analyte to investigate the performance of the SERS substrates since R6G has been extensively studied and well characterized by SERS [92,181,182]. Rhodamine 6G were purchased from Sigma Aldrich. R6G were used as received without further purification. Distilled water passed through a Millipore system (ρ =18.2 MΩ) was used in all experiments.

Several solutions of R6G with Milli-Q water as solvent were tested. The samples were prepared by dropping 2 μL of R6G solutions with different concentrations, 10^{-6}, 10^{-7}, 10^{-8} and 10^{-9} M (9.58×10^{-1}, 9.58×10^{-2}, 9.58×10^{-3}, 9.58×10^{-4} nanograms of R6G, respectively), on the SERS substrates. A 10^{-3} M (1.5 nanograms) R6G solution (2 μL volume) was used on glass substrate as the control reference. These solutions were dispersed on the samples in a drop radius of 1 mm and dried at room conditions. The areas of the vibrational lines at 1360 and 1509 cm^{-1} were used to calculate the spectral intensity.

The average SERS enhancement factor (*EF*) is calculated according to the equation 2.4 [168]:

$$EF = \frac{I_{SERS}}{I_{Raman}} \times \frac{N_{Raman}}{N_{SERS}} \tag{2.4}$$

Where, I_{SERS} is the SERS intensity of a particular Raman vibrational line of the analyte (in this case R6G) and I_{Raman} is the normal (not enhanced) Raman intensity of the R6G measured over a non-plasmonic reference substrate. The Raman signal of the reference is, in most cases, too weak to be detected when measuring small analyte concentrations on the surface. Therefore, the analyte concentration applied to measure the reference Raman spectra are usually higher than that used in the SERS spectra, so a correction factor (N_{Raman} / N_{SERS}) is introduced in the *EF* expression to take that into account. In the present measurements, N_{SERS} corresponds to the estimated number of molecules contributing to the SERS signal, while N_{Raman} is the number of molecules contributing to the reference Raman signal (from non-SERS surface). Both values are related to the available area of the SERS substrate and the laser spot focus. They are determined by the relation:

$$N_{SERS} = \eta \times N_A \times V \times C_{SERS} \times \frac{A_{laser}}{A_{SERS}} \ ; \ N_{Raman} = N_A \times V \times C_{Raman} \times \frac{A_{laser}}{A_{Raman}} \tag{2.5}$$

where N_A is the Avogadro number, V is total volume of solution spread on the substrate (2 μL), A_{Laser} is the area of the laser spot (8.32×10^{-7} mm^2), A_{SERS} and A_{Raman} are the total area of the SERS and non-SERS reference substrate respectively, covered by the drop of analyte solution. C_{SERS} and C_{Raman} are the concentrations of analyte applied over the SERS and non-SERS substrates, respectively. Since the same volume of solution was applied in both substrates, $A_{SERS} \approx A_{Raman} = 3.14$ mm^2. The dimensionless adsorption factor, η, is taken to be 0.3 in accordance with previous reports that use similar types of substrates [183]. This adsorption factor is based in Langmuir isotherm, and can be expressed in the form: $\eta = 1/(1+Kc_o)$; where c_o is the initial concentration of the analyte at saturation level and K the equilibrium binding constant.

2.6 Solar cell fabrication and characterization

2.6.1 Implementation of Ag NPs in the PBR configuration

In solar cell applications, the Ag MNP arrays are usually embedded in a thin TCO layer [37,39,62,184], located between the silicon absorbing material and a flat silver mirror, in a configuration known as plasmonic back reflector (PBR) [40,59,176,185]. The structure of the PBR is shown in Figure 2.14. The PBRs were fabricated on corning glass substrate with the structure: glass/Ag mirror (120 nm)/AZO/Ag NPs/AZO. The planar Ag layer on glass was deposited by electron beam-assisted thermal evaporation technique (described in section 2.1.1) and the AZO layers were deposited by RF magnetron sputtering (described in section 2.3.1). To investigate the plasmonic-based light trapping in TF silicon solar cells, several PBRs with distinct optical properties were selected as substrates for the fabrication of nip μc-Si:H solar cells. The PBRs were characterized morphological and optically prior to the deposition of silicon, and their influence on the solar cell performance was studied.

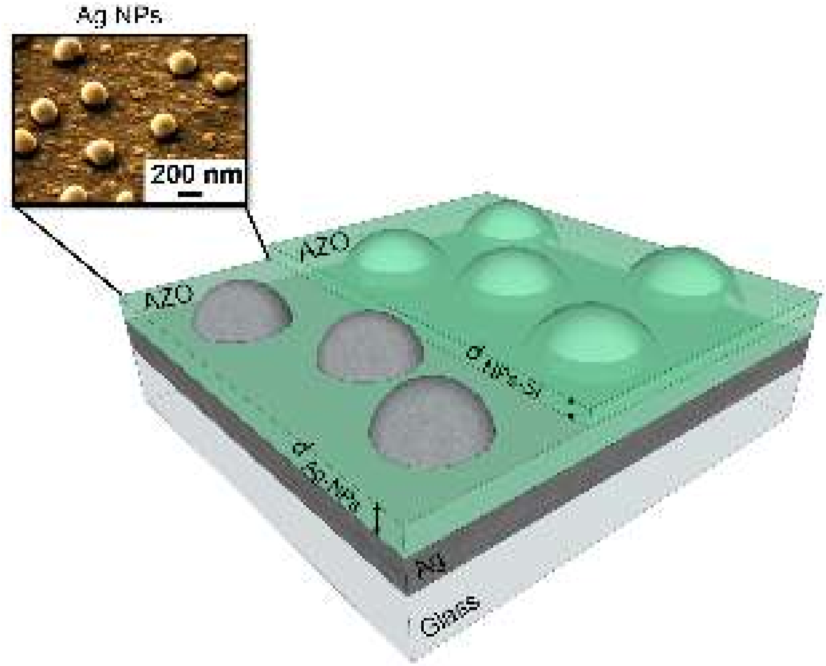

Figure 2.14 Schematic structure of a PBR consisting of the following layers stack: glass/Ag/AZO/Ag NPs/AZO. There are two AZO layers in a plasmonic BR: One layer goes below the Ag NPs, separating the Ag planar film from the Ag NPs, with a thickness $d_{\text{Ag-NPs}}$, and the other layer is above the Ag NPs, separating the Ag NPs from the Si cell layers (not shown) deposited on top, with a thickness $d_{\text{NPs-Si}}$. The inset shows an SEM close-up image of the Ag NPs on an uncoated PBR.

2.6.2 Solar cell fabrication by PECVD

The nip μc-Si:H solar cells were deposited on the PBRs at a temperature of 160 °C using an ELECTTRORAVA (Figure 2.15, also known as MIR) Plasma Enhanced Chemical Vapor Deposition system. The MIR system contains 4 satellite chambers connected to a central load-lock chamber. Three satellite chambers (DPC1-3) are used for the deposition of, respectively, intrinsic (i), p-doped and n-doped Si; while the fourth chamber (DPC4) is reserved for sputtering of AZO. The substrates are loaded in the load-lock chamber and then transferred to the deposition chambers (DPCs) by dragging them with the side arms. Such arms have hooks on the ends which attach to side holes in the substrate holder.

Figure 2.15 ELECTTRORAVA PECVD system existent in CEMOP used for the deposition of the Silicon thin layers.

The structure of the μc-Si:H nip solar cell deposited on the PBRs consists of a stack of 54 nm n-type microcrystalline, 1.5 μm intrinsic microcrystalline a 20 nm p-type μc-Si:H. This was followed by the application of a Kapton mask with circular holes, 3 mm in diameter, on the cell's front surface and by the deposition of the 200 nm IZO front electrode via RF magnetron sputtering [43]. After removing the masks, reactive ion etching with SF6 plasma using a Trion Phantom III RIE ATCH system was applied to remove the Si material left uncovered by the IZO layer, thereby defining circular devices with 3 mm in diameter. Finally, to improve the electrical performance, all the cells were annealed in low vacuum at 150 C° for 2 h.

The intrinsic layer of μc-Si cells is relatively thick (~1.5 μm) compared to that of a-Si cells (~300 nm). Therefore, the process time required to fabricate μc-Si is much longer. Increasing the frequency of the power generator allows faster deposition without requiring a higher power (which can damage the pre-deposited material due to the strongly accelerated impinging species). So, to grow the intrinsic layer of this type of cells it is essential to use the VHF generator instead of the standard RF. The VHF is solely used for the intrinsic layer of μc-Si cells, since the doped layers are quite thin, allowing the deposition at a slower speed with the RF power. The intrinsic μc-Si is usually deposited with the VHF generator at an operating frequency of 75 MHz.

2.6.3 Solar cell characterization

The solar cell devices are characterized by measuring the I-V curves and by evaluating the external quantum efficiency (EQE). The optical performances of the device structures were also measured via spectrophotometry in order to understand the enhancements in the EQE.

2.6.3.1 I-V CURVES

The I-V characteristic curves are a graphical representation of the operation of a solar cell, summarizing the relationship between the current and voltage at the existing conditions of irradiance and temperature, and necessary to determine the device's output performance and light-to-electricity conversion efficiency. In this work, the silicon solar cells are characterized by measuring the I-V curves, under one sun illumination (AM 1.5G, 100 mWcm^{-2}) in a Spire Sun Simulator 240A (Figure 2.16). This system tests photovoltaic devices under Air Mass 1.5 Global terrestrial conditions, using a filtered pulsed Xe light source that closely matches the solar spectrum avoiding excessive device heating associated with continuous sources.

The SUN SIMULATOR provides an I-V curve display, from where the open-circuit voltage V_{OC} (V), short-circuit current density J_{sc} (mA/cm^2), efficiency η (%), fill factor FF (%), series resistance R_s *(Ω)* and shunt resistance R_{sh} (Ω) of the cells are extracted.

Figure 2.16 Spire Sun Simulator 240A existent in CENIMAT.

2.6.3.2 Spectral response and quantum efficiency

The Spectral response (SR) is defined as the ratio of the short-circuit current density (J_{SC} in A/cm^2) generated by the solar cell, to the irradiance (δ in W/cm^2), as indicated in equation 2.6:

$$SR(\lambda) = \frac{J_{SC}}{\delta(\lambda)} \tag{2.6}$$

While the quantum efficiency (QE) is the number of electron-hole pairs generated by each incident photon, and is a function of the spectral response. This quantity relates the number of incident photons in the cell to the number of electrons in the external circuit:

$$QE(\lambda) = \frac{hc}{q\lambda} \cdot SR = 1.24 \cdot \frac{SR}{\lambda} \tag{2.7}$$

where, c and h are, respectively, the speed of light and the Planck constant, λ the wavelength (in the equation λ is in µm) and *q* the electron charge.

The SR and QE of the Si solar cells were measured using a homemade system (Figure 2.17) in short-circuit condition, in the 200-1100 nm wavelength range with a 10 nm wavelength interval between each measured data point. In this analysis, the sample is exposed to a monochromatic electromagnetic radiation, and its short-circuit current is being registered as function of the incident light wavelength.

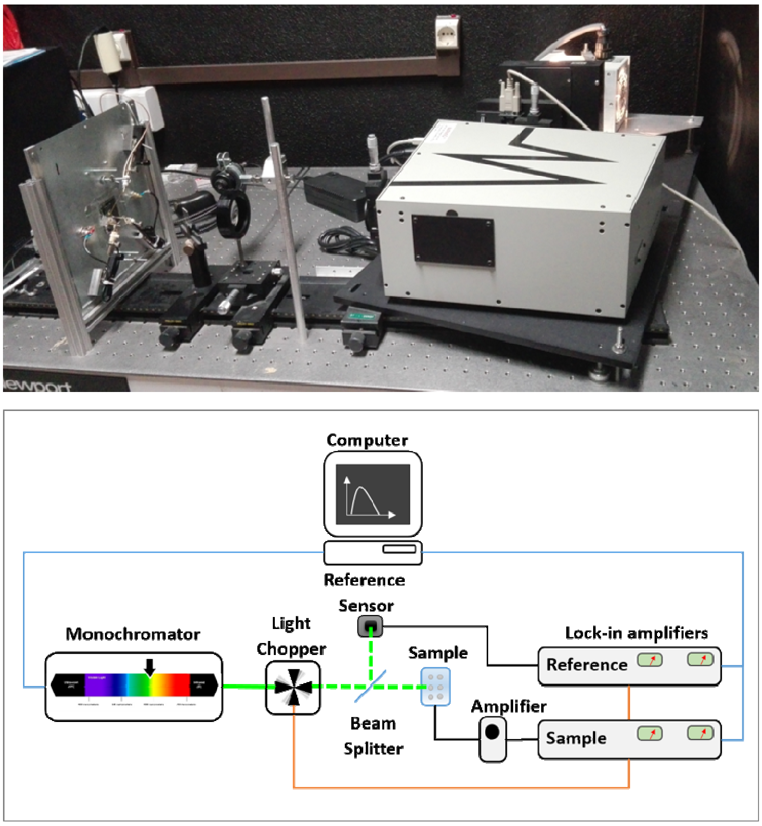

Figure 2.17 Homemade Spectral Response and Quantum Efficiency system (Top) and schematic representation of the Spectral Response and Quantum Efficiency Setup (Bottom).

Chapter 3

Silver Nanoparticles by Dewetting Process for Thin Film Si Solar Cells Application

This chapter reports a successful implementation of a plasmonic light trapping scheme implemented in a thin film (TF) microcrystalline silicon (μc-Si:H) solar cell in PBR configuration. The morphological and optical properties of Ag nanoparticles structures produced on distinct surfaces by a simple, fast and highly reproducible method employing rapid thermal annealing, are systematically investigated. The results indicate that both the thermal conductivity and roughness of the surface play a determinant role on the morphology of the nanostructures formed.

After the establishment of the best conditions, the self-assembled Ag NPs are implemented in TF μc-Si:H solar cells with PBR configuration. First, the role of the RTA heating rate on the NPs production is studied, the results indicate that Ag NPs with favourable monodispersed geometries can be produced by an ultra-fast RTA process (>5× faster than the present state of art), with excellent light scattering properties. In the second part an attempt on implementation of the plasmonic light trapping in μc-Si:H solar cells is presented. The effect of the AZO spacer layer between NPs and rear mirror, and between NPs and silicon layer, on the morphological and optical performance of the PBRs, and consequently on the performance of the solar cells, is tested. The performance of the PBRs was carefully adjusted, to yield maximum light trapping (low parasitic absorption and high near-infrared scattering) with minimum degradation of the cells' electrical properties. The best spacer thicknesses were found to be 100 and 60 nm, respectively, for Ag NPs with preferential sizes of about 200 nm. The microcrystalline silicon (μc-Si:H) solar cells deposited on such improved PBR demonstrate an overall 11% improvement on device efficiency, corresponding to a photocurrent of 24.4 mA/cm^2 and an efficiency of 6.78 %, against 21.79 mA/cm^2 and 6.12 %, respectively, obtained on flat structures without NPs.

This chapter contains relevant information from the publications:

Araújo A, Mendes M J, Mateus T, Nunes D, Calmeiro T, Fortunato E, Hugo A and Martins R 2016 Influence of the Substrate on the Morphology of Self-Assembled Silver Nanoparticles by Rapid Thermal Annealing *J. Phys. Chem. C* **120** 18235–42.

Araújo A, Mendes M J, Mateus T, Costa J, Nunes D, Água H and Martins R 2018 Ultra-fast plasmonic back reflectors production for light trapping in thin Si solar cells *Solar Energy, accepted for publication.*

3.1 Introduction

TF PV technology is one of the candidates to take over from the current commercial-dominant Si wafer-based technology in the long-term, as it has potential for higher performance/cost ratio due to the use of less amount of Si and by employing CVD methods which are deemed to be more cost-effective than the traditional c-Si ingot cutting [37,39,59]. Moreover, solar cells with film thicknesses in the 1–2 μm range can be deposited on cheap module-sized substrates which can be rigid, such as glass, or mechanically flexible, such as plastic [186], stainless steel foils [40] or even paper-based [55,57]. A common limitation to many TF PV technologies is their low light absorbance for energies near the bandgap (the absorption coefficient decreases significantly with increasing illumination wavelength) [43], due to their reduced absorber thicknesses, in particular for the indirect-bandgap semiconductor Si. For example, although the Si bandgap lies at ~1120 nm, in nc-Si TFs, the absorption coefficient drops quickly below 1000 cm^{-1} for wavelengths above 800 nm [45,46].

Enhancement of optical absorption by LT is crucial to obtain high efficient TF Si solar cells. LT structures makes the long-wavelength photons travel in the solar cell distances much longer than the device thickness, increasing the probability of their absorption. This can achieved by the scattering of light at the cell's interfaces, either by transmission at the top interfaces or by reflection at the rear ones. In conventional TF Si solar cells, LT is typically achieved using random texturing of either the front transparent contact, in superstrate cell configurations [43,65,66], or of the rear contact/mirror in substrate configurations [67–69]. However, the texturing approach produces high surface roughness which contributes to the creation of bulk and surface defects (charge carrier traps) and, as a consequence, increases recombination in the silicon layers which degrades the electrical performance of the device [70]. A recent alternative solution consists in the use of MNPs with strong LT, via light scattering [23,37,59,71], keeping the PV film as flat as possible, to maximize both the photo-generated current and the operating voltage and fill factor. Ag NPs have been applied mostly due to their strongest plasmon resonances in the visible to NIR spectral region [9,16,73], and due to the fact that they can be fabricated with high control of size and shape by various methods [12,40,72].

When MNPs are excited by electromagnetic radiation, their free electrons collectively oscillate and localized surface plasmon resonances can occur at the appropriate photon energies. At the LSPR, the MNPs can produce a particularly intense localized scattered near-field and propagating far-field [13,56,92]. The MNPs far-field scattering has been considered a promising light trapping mechanism, since it can boost the optical path length of the near-bandgap photons that are weakly absorbed by TF SC [11,12], thus increasing their absorption and conversion efficiency. The resonant optical properties of the MNPs depend strongly on the geometry of the particles, as well as on their material and surrounding media [73,119,171]. Thus, the MNPs size, shape, and distribution must be well designed to maximize scattering and minimize the parasitic losses (light absorption within the MNPs) across the wavelength range of interest, which for TF Si SC corresponds to the near infrared (600–1100 nm range) [39].

Solid-state dewetting is a well-known industrially-scalable process capable of morphologically transforming (by self-assembly) a continuous thin film in islands or droplets due to a thermal treatment. This technique is commonly used for the fabrication of metallic nanostructures [39,62,71], with advantages of low-cost, simplicity, direct scalability and compatibility with industrial manufacturing processes. However, most of the typically employed annealing processes (e.g. using a tube furnace) require annealing times of one or more hours [12,176,187] to form the preferential morphologies composed of individual 100-300 nm semi-ellipsoidal MNPs. The RTA [187] process optimized in this work is an advantageous method to yield such plasmonic surfaces with high reproducibility and large-area uniformity within just a few minutes of annealing time [72], when compared with other commonly employed annealing processes (e.g., using a tube furnace) [188,189], bringing industrial benefits in terms of time and energy.

It is important to point out that, with this approach, the volume of Ag used in the NPs deposition (equivalent to a 6-10 nm film) is negligible compared to the volume of the ~120 nm thick Ag film that is typically used for the back contact of commercial TF Si solar cells. Therefore, this is a really cost-efficient process since it does not imply any significant increase in the material expenses.

In solar cell applications, the Ag MNP arrays are usually embedded in a thin TCO layer [37,39,62,184], located between the silicon absorbing material and a flat Ag mirror (rear contact), in a configuration known as PBR [40,59,176,185]. The TCO layer acts as a barrier, which not only inhibits charge carrier recombination at the MNPs surface but also prevents the migration of metallic impurities from the particles to the photovoltaic material. Despite the strong efforts taken to optimize the Ag MNPs morphology in order to maximize the SC efficiency [39,119,171,175], most works focus in structures tested on glass substrates which are of little interest for SCs since we have observed that the MNPs morphology drastically changes when they are formed on TCOs. So far, little attention has been given to the role of the physical properties of the underlying TCO layer on the dewetting mechanism. In the first part of this chapter, we investigate the role of the TCO layer's properties (conductivity and roughness) on the morphology of MNP arrays produced by thermal evaporation followed by RTA. To the best of the author knowledge, previous reports have only analyzed distributions of the MNPs' in-plane dimensions [12,176]. Here, not only the Ag MNPs formation mechanism is described for different TCOs substrates, but we also correlate their morphological and optical properties with the substrate conductivity and roughness. In addition, for the best-obtained structure for SC application (i.e., with highest light scattering and lowest parasitic absorption), a complete study of the particles geometry, including the height distribution, is presented. Next, the self-assembled Ag NPs are incorporated in a PBR configuration and integrated in thin film silicon solar cells. The first part of the study concerns the investigation of the effect of the RTA heating rate on the morphological properties of Ag NPs, which revealed to be the key parameter that enabled a dramatic decrease in the annealing process time. By increasing the heating rate, PBRs with pronounced light diffusion and reflection properties, comparable to the best in the state-of-the-art, have been formed in only 10 minutes of RTA. Besides, we show that the position of the MNPs array within the TCO in also of crucial importance to optimize the distance-dependent near-field optical interaction (parasitic absorption and scattering) with both the silicon layer and the mirror [23,59], as has been studied theoretically [190].

Here, we study the design routes of PBRs, produced by ultra-fast RTA processes, applied to hydrogenated μc-Si:H solar cells. It was found that both the thickness of AZO spacer layer between Ag film and Ag NPs and the thickness of AZO spacer between Ag NPs and n-doped μc-Si:H layer have a significant influence on the performance of solar cells with PBRs. We experimentally also demonstrate that the thickness of the bottom AZO layer is crucial on the morphological and optical performance of the PBR, and consequently on the optical performance of the solar cell.

3.2 Influence of the substrate on the morphology of self-assembled Ag nanoparticles

Metal nanoparticles are of great interest for light trapping in photovoltaics. They are usually incorporated in the rear electrode of solar cells, providing strong light scattering at their surface plasmon resonances. In most cases, the nanoparticles are self-assembled by solid-state dewetting over a TCO layer incorporated in the cell's rear electrode. Up to now, this process has been optimized mainly by tuning the thermal annealing parameters responsible for dewetting, or the thickness of the precursor metallic layer; but little attention has been paid to the influence of the underlying TCO layer properties on the morphology of the nanoparticles formed, which is the focus of the present chapter. This work investigates Ag nanoparticles structures produced on distinct surfaces by a simple, fast and highly reproducible method employing rapid thermal annealing. The results indicate that both the thermal conductivity and surface roughness of the TCO layer play a determinant role on the morphology of the nanostructures formed. This is of particular relevance, since we show in the study performed that the parasitic absorption of these Ag nanostructures is reduced, while the scattering is enhanced when the Ag nanostructures are formed on TCO layers with the highest conductivity and the lowest surface roughness (~1 nm).

These results unveil novel possibilities for the improvement of plasmonic nanostructures fabricated by thermal dewetting, via the careful adjustment of the physical properties of the underlying surface.

3.2.1 Sample preparation

A set of degenerated (free carrier concentration, $n > 10^{19}$ cm^{-3}) polycrystalline TCO films of different materials [ZnO, AZO, GZO] was deposited by RF magnetron sputtering (See chapter 2, section 2.3.1), Table 3.1 shows the thickness, the RMS surface roughness, and the electrical conductivity of the TCO films obtained. Two sets of samples were used. In the first set, the TCO material was varied and the thicknesses was fixed at 30 nm, which is the thickness typically used in plasmonic back reflector structures of TF Si SC [40,59,176,185]. This allowed us to obtain TCOs having approximately the same roughness (determined by AFM) but with a range of conductivities. In order to analyze the effect of the roughness in the MNPs morphology, a second set of experiments were performed. In this second set the TCO material was kept constant (AZO) but two more thicknesses were produced, 90 and 120 nm, in order to achieve surfaces with higher roughness. This allowed us to separate the influence of the TCOs electrical conductivity from the roughness on the morphology of the Ag NPs formed.

Table 3.1 Summary of the properties of the TCO films deposited on glass substrate [thickness, RMS roughness, electrical conductivity (σ), estimated thermal conductivity via free electrons (λ_{el}) and refractive index (N)], determined with the techniques described in sub-section 2.3.

Substrate material	Thicknesses (nm)	RMS (nm)	σ (S cm^{-1})	λ_{el} [1] (W cm^{-1} K^{-1})	N $\lambda = 635$ nm
Glass	-	0.19 ± 0.01	~ 0	~ 0	1.5
ZnO	30	1.26 ± 0.16	1.77	0.13	1.9
GZO	30	0.70 ± 0.35	14.47	1.06	2.1
AZO	30	0.90 ±0.24	59.52	4.35	2.1
AZO	90	2.02 ± 0.11	71.43	5.22	2.0
AZO	120	4.76 ± 0.57	83.33	6.01	1.9

[1] approximate thermal conductivity values inferred by the Wiedemann–Franz law [191].

Ag precursor films with thickness of 2–8 nm were thermally evaporated on the different substrates prepared. The 6 nm thickness was observed to be favorable for the formation of self-assembled Ag MNPs with the adequate sizes for effective light scattering, as discussed below [56,120]. Therefore, for the observation of the Ag NPs formation as a function of the TCO surface roughness and applications in TF Si solar cells the Ag film thickness was fixed at 6 nm. The evaporation of the Ag thin films was carried out in an e-beam system (Chapter 2, section 2.1.1). The thermal annealing of the ultrathin Ag films coated on the different substrates was carried out in N_2 atmosphere at a temperature of 500 °C for 20 min by RTA with a heating rate of 16 °C/s.

3.2.2 Morphological and optical properties of Ag NPs deposited on glass and oxides surfaces

Figure 3.1 depicts the SEM images of Ag NPs formed on different surfaces after annealing of 2, 4, 6 and 8 nm thick precursor film for 20 minutes at 500 °C. This matrix of SEM images maps out the influence of the underlying surface on the morphology of the Ag NPs formed. Each row in the matrix corresponds to the same substrate surface while each column corresponds to the same Ag precursor film thickness.

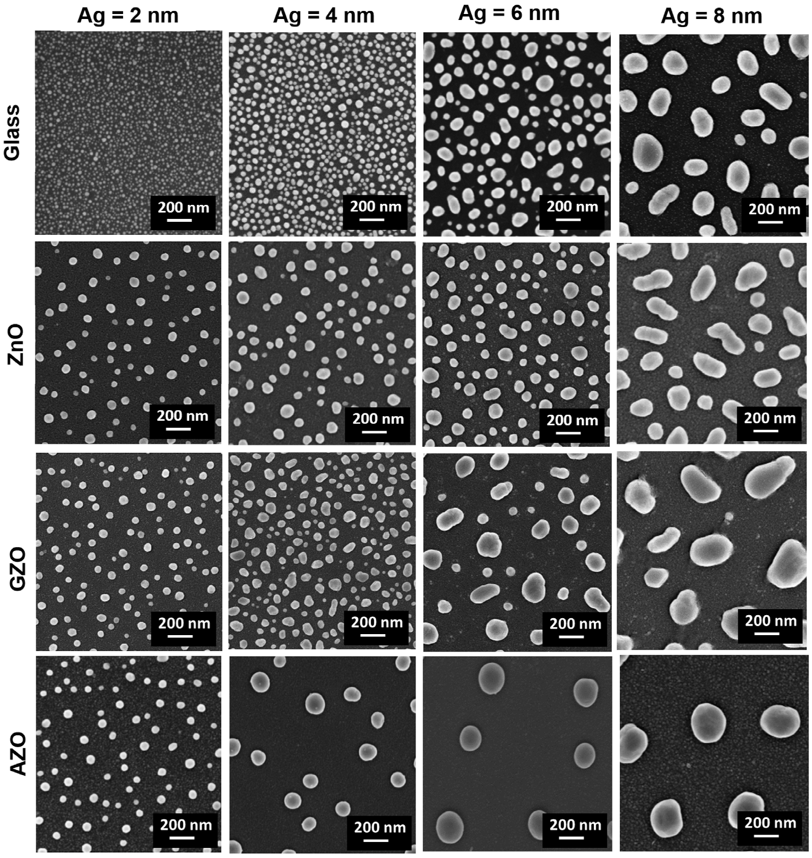

Figure 3.1 Matrix of SEM images showing the Ag NPs obtained via dewetting of ultrathin films at 500 °C, deposited on distinct surfaces. The Ag precursor film thickness is indicated at the top

and the different surface materials are shown on the left. The thickness of the TCO layers (ZnO, GZO, AZO) beneath the MNPs is 30 nm for all cases.

For all substrate surfaces, as the precursor film the Ag layer increases, the NPs become bigger and the distribution of sizes broadens significantly. Morawiec *et al.* [12] reported a similar dependence for nanostructures fabricated by thermal evaporation with a post annealing process (400 °C for 1 h).

Figures 3.2 (a) and (b) display, respectively, in-plane size distribution histograms and the corresponding optical spectra of the Ag MNPs formed on the different substrates by thermal dewetting of 6 nm Ag precursor films. Such precursor film thickness is the one selected for further analysis since it is sufficient to form well-distributed Ag MNPs arrays with a size distribution within the appropriate range (~100-300 nm) for lower parasitic absorption and strongest far-field light scattering, as commented below [56,120]. Thicker precursor films could result in bigger and more irregularly-shaped MNPs, thereby broadening the plasmonic response of the particles ensemble and decreasing its resonant effect.

The optical properties of the nanostructures are shown in Figure 3.2 (b). Two main peaks are present in the reflectance spectra: a broad peak at longer wavelengths corresponding to the dipolar LSPRs of the Ag MNPs and a narrower peak at shorter wavelengths corresponding to the quadrupole resonance [119]. The increase in the average particle size results in both a red shift and broadening of the LSPR peaks, and also in an increase of the amount of scattered light as can be seen from the R_{DIF} and T_{DIF} curves. A higher refractive index of the media surrounding the particles can also contribute to such effects, but the small differences in the effective medium among the TCO-coated samples ($N \approx 2$ for ZnO, AZO and GZO – see Table 3.1) should not provide significant changes to the scattering spectra of the nanostructures. The main distinctions are therefore attributed to the MNPs sizes; but it is also important to consider the changes in NPs shape. When comparing the optical spectra on GZO and AZO, the dipolar LSPR is located at approximately the same wavelength despite the fact that the average MNP size on AZO is clearly higher. This occurs because the particles on AZO are less elongated, i.e. more spherical (as demonstrated below), which blue-shifts the resonance and thereby counter-balances the effect of the size increase.

It is interesting to observe that the highest amount of light scattering (measured by R_{DIF} and T_{DIF}) is obtained for the Ag MNPs array with the lowest surface coverage (8%) formed on AZO, because such nanostructure is composed of more monodispersed large (> 100 nm) sizes that have better scattering efficiency [56]. The presence of small (<100 nm) particles and shorter inter-particle distances (higher SC) on the other substrates cause higher parasitic absorption (due to higher absorption cross sections and dispersive MNP interactions) and lower light scattering performance. MNPs with sizes above 100 nm exhibit pronounced scattering cross sections that are much higher than their absorption cross sections, so their light scattering performance exceeds their parasitic light losses in the wavelength range of interest [174]. This is seen in the optical results of Figure 3.2 (b), since only the bigger particle structures formed on GZO and AZO yield light diffusion peaks (R_{DIF} and T_{DIF}) above the absorption throughout the NIR wavelength range of interest for TF Si SC (600-1100 nm). The scattering cross sections of such large Ag MNPs can be up to ~10 times higher than the particles' cross sectional area at their plasmonic resonances. So, the MNPs can interact with light in their surroundings within a nearby region much larger than their physical volume. Therefore, low surface coverages of ~8-10% are preferential to high coverages (>20%, as those obtained here on GZO and ZnO or usually formed with conventional thin film annealing processes) [12,184] in order to avoid parasitic inter-particle effects while still allowing full interaction of the MNPs array with the incoming light.

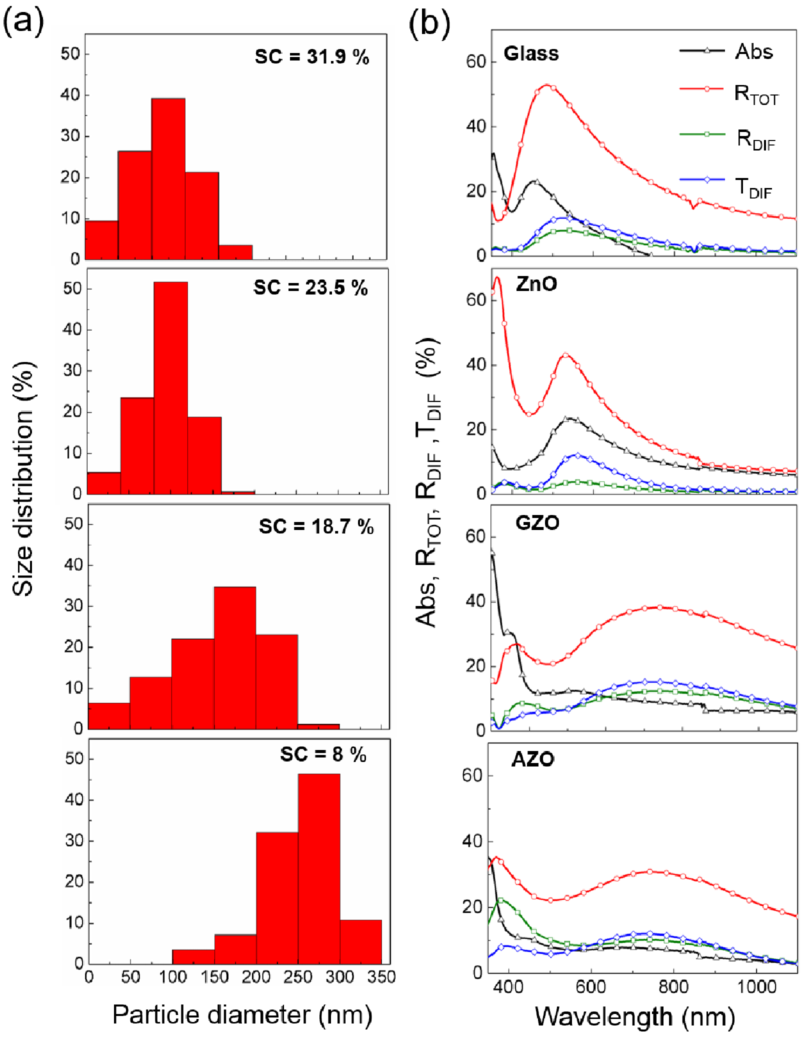

Figure 3.2 Morphological and optical properties of the MNP arrays of Figure 3.1, formed from 6 nm Ag precursor films deposited on glass, ZnO, GZO and AZO (displayed respectively from top

to bottom). (a) Histograms of the size distribution with the indication of the surface coverage (SC). (b) Optical properties of the nanostructures, showing the LSPRs spectral extension.

Comparing the Ag MNPs array on AZO with the other substrate surfaces, it is shown that on AZO the Ag MNPs become more round, larger in size, and the total surface coverage (SC) decreases monotonically from 31.9% on glass to 8.0% on AZO. Since no noticeable Ag remains on the TCOs surface between the particles, as confirmed by Energy Dispersive Spectroscopy (EDS, see Figure 3.3), neither is lost during the annealing process, a SC reduction implies that the height of the particles increases, so the MNPs become less flat and more spherical as mentioned before.

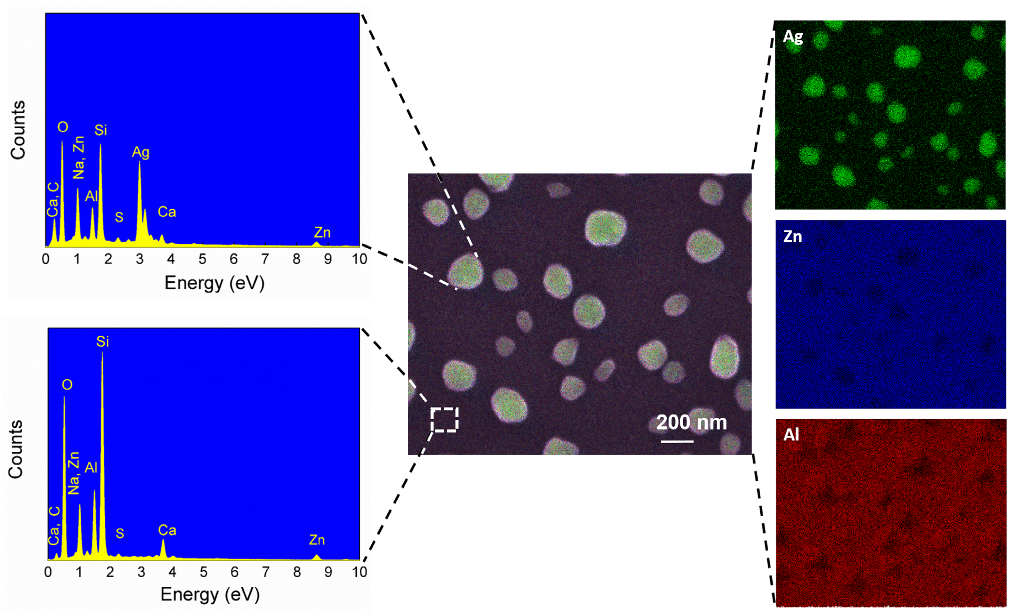

Figure 3.3 EDS point analyses (left side) and EDS X-ray maps of Ag, Zn and Al (right side) obtained on the AZO substrate and Ag MNPs formed. This analysis reveals that there are no traces of Ag material remaining in the inter-particle spaces after annealing.

Figure 3.4 analyzes the cross-sectional geometry of the preferential self-assembled Ag MNPs array, formed from the 6 nm Ag precursor film on the surface of 30 nm of AZO. The SEM images of Figure 3.4 (a) confirm that the NPs are uniformly distributed on the surface and no aggregation is observed. Figures 3.4 (b) and (c) show, respectively, the height distribution of the sample and the vertical profile of a single Ag MNP extracted from the AFM scan presented in the inset. It is shown that 70% of the NPs have a height of 140 ± 20 nm, which is slightly above their average radius (~125 nm, see bottom histogram of Figure 3.4 (a). Therefore, the average sphericity (Ψ = 0.86) is close but slightly above that of a semi-sphere (Ψ = 0.84); being the sphericity calculated using $\Psi = \pi^{1/3}\left(6\,V_P\right)^{2/3}/A_p$, where V_P is the volume of the particle and A_P is its surface area.

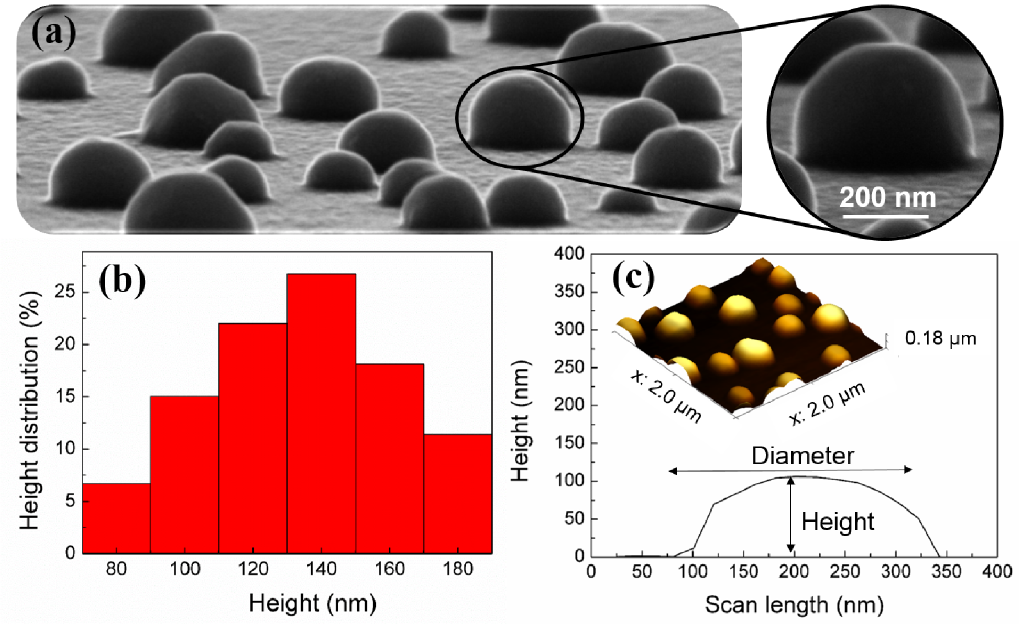

Figure 3.4 Morphology of self-assembled Ag MNPs formed from 6 nm of Ag at 500 °C on AZO substrate. (a) Cross section SEM tilted by 90°, showing close-up images of the Ag NPs and the equilibrium contact angle. (b) Histogram of the height distribution measured by AFM analysis. (c) AFM height profile of an Ag MNP across the center; inset: AFM scan on a 2 × 2 µm² area.

3.2.3 Correlation between contact angle and morphological properties

As-deposited thin films of Ag with nanoscopic thickness do not actually form a continuous layer, instead small worm-like islands are formed which transform upon annealing [12]. When sufficiently high temperatures (>300 °C) are used, two transformations can occur simultaneously: 1) the nano-islands diffuse along the surface and merge (coalesce) with each other, forming bigger particles and 2) the shape of the particles is altered to minimize their surface energy, thus becoming more semi-spherical [192]. These are thermally activated kinetic processes that reduce the total free energy of the system by rearranging the Ag material distributed on the surface [193].

In particular the coalescence process, responsible for the increase of the particles size, critically depends on the mobility of the Ag atoms on the surface and, therefore, on the properties of the underlying material. A key property that influences the mobility of the Ag NPs during annealing is their adhesion energy $\left(E_{ad}=\gamma_m+\left(1+\cos\theta\right)\right)$ to the substrate surface, which is determined by the surface energy of the Ag film $\left(\gamma_m\right)$ and the equilibrium contact angle $\left(\theta\right)$ of the particles [193]. The contact angle of a set of NPs, formed from the 6 nm Ag precursor film, was measured by cross-sectional SEM images and no pronounced differences

$\left[\left(\theta_{\mathrm{ZnO-Ag}}=91^\circ\pm4.2^\circ\right);\left(\theta_{\mathrm{GZO-Ag}}=89.6^\circ\pm7^\circ\right);\left(\theta_{\mathrm{AZO-Ag}}=89.5^\circ\pm2^\circ\right)\right]$ were found for the NPs distributions on the different TCO surfaces. This would be expected, since the TCOs are all ZnO-based materials. However, significantly smaller angles $\left(\theta_{\mathrm{Glass-Ag}}=76^\circ\pm4.2^\circ\right)$ were measured for the glass substrate. Therefore, the higher E_{ad} of the Ag NPs on glass can explain their lower mobility, and thereby reduced coalescence, relative to the particles on the different TCO surfaces.

3.2.4 Effect of the surface conductivity

The other key property that hinders their mobility is the surface roughness [194], whose values are indicated in Table 3.1 for the analyzed TCO films. Nevertheless, since the TCO layers have the same 30 nm in thickness, their roughness values are small and quite similar within the error range. Moreover, the small differences in roughness do not correlate with the differences in NPs morphology (i.e. particles size and SC) mapped in Figures 3.1 and 3.2. Therefore, among the samples containing 30 nm TCOs, the differences in their NPs kinetics during annealing cannot be attributed to the roughness variation. Such differences are more likely caused by the distinct TCOs thermal conductivity [195,196], which is directly related to the electrical conductivity, σ, presented in Table 3.1.

Figure 3.5 shows the average Ag MNP size (in-plane diameter) and the SC as a function of the electrical conductivity of the different substrate surfaces. There is a clear correlation between the average Ag MNP size and the substrate conductivity, which increases monotonically from ZnO to AZO, as can be observed in Figures 3.1 and 3.2. As expected, the opposite trend is observed for the surface coverage due to the conservation of the total Ag material on the surface.

Surfaces with higher thermal conductivity (see Table 3.1) have a higher heating rate and can transfer heat more efficiently to the Ag material, which promotes its mobility on the surface. On thermal insulating surfaces such as glass (top row of Figures 3.1 and 3.2), the surface diffusion length is lower than the average distance between the particles, so the migration and coalescence process is suppressed and the particles remain small even for longer annealing times. Therefore, the results indicate that a higher conductivity induces a higher mobility of the Ag material on the surface and, consequently, a higher NPs coalescence during annealing. This results in the reduction of the number of small MNPs, the formation of more spherical and larger particles, and a lower surface coverage. For this reason, the nanostructures formed on the more conductive layer (AZO - bottom of Figures 3.1 and 3.2) present a remarkable increase in the size and uniformity of the MNPs and the lowest surface coverage (~ 8%).

This morphology is expected to yield strong light scattering of red-NIR light and a relatively small parasitic absorption with respect to the Ag MNP structures attained so far by dewetting for application in plasmonic back reflectors of TF SC [56,59].

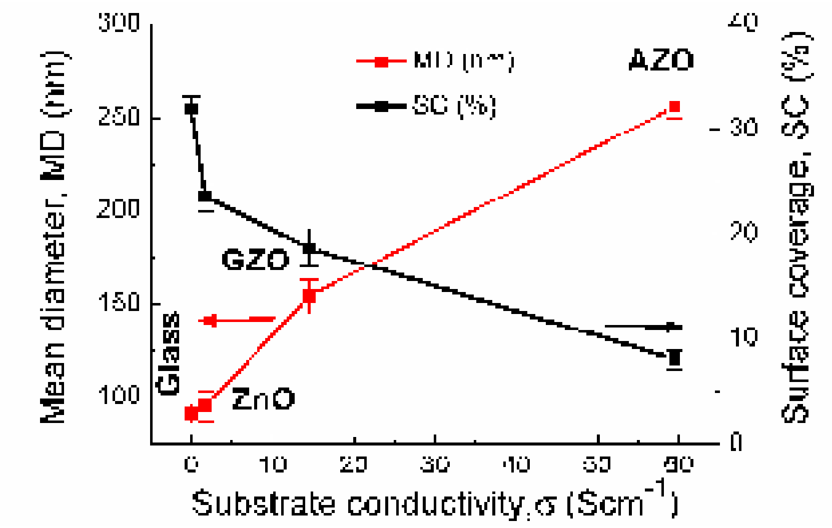

Figure 3.5 Dependence of the average Ag MNP size and surface coverage on the substrate electrical conductivity. The red and black lines are guides to the eyes. The points in the plot for MD and SC have an associated error estimated by analyzing, for the different points, sets of 3 samples fabricated with the same parameters.

3.2.5 Effect of the Surface roughness

Since the surface conductivity can be a crucial parameter affecting the self-assembling mechanism of Ag MNPs by thermal annealing, one might expect that thicker TCO films may lead to better distributions, as they become more electrical and thermal conductive. However, that may not be the case, since the surface roughness can come into play [194]. Figure 3.6 presents SEM images of the Ag MNPs formed on AZO films with different thicknesses (30, 90 and 120 nm) on glass substrates, using the same annealing conditions as those of Figure 3.1. The values of the root mean-square roughness of the films' surface and their electrical conductivity are shown in the images and in Table 3.1. The roughness of the substrates with 90/120 nm of AZO is ~3/6 times higher than that of Figure 3.1 with 30 nm AZO, thereby forming higher barriers for the Ag diffusion which significantly hinders the migration and coalescence process of the MNPs. This means that, as the substrate roughness increases, the NPs become quite irregular in shape and size [194], making it difficult to compare their mean morphological properties as performed in Figure 3.5. This indicates that, in this case, the substrate surface roughness has also an important role, which opposes that of the thermal conductivity of the film where the MNPs are formed. In general, the conductivity favors the increase of the NPs size, while the roughness causes obstacles to such increase and worsens the uniformity of the NPs geometry.

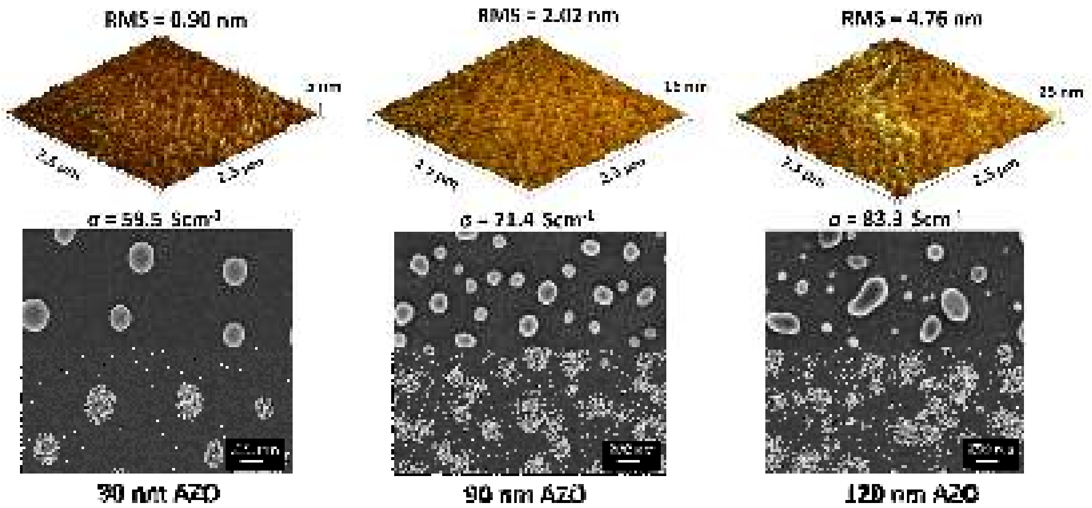

Figure 3.6 Top: AFM scans on 2.5 × 2.5 µm² areas of distinct AZO layers with 30, 90 and 120 nm thickness. The root mean square (RMS) surface roughness values and the electrical conductivity (σ) of the AZO layers are indicated in each image. Bottom: SEM images of Ag NPs.

3.3 Ultra-fast plasmonics back reflector production for TF Si solar cells application

This study reports a fast method to fabricate plasmonic light trapping structures in just ten minutes (>5× faster than the present state of art), with excellent light scattering properties. The structures are composed of Ag NPs deposited by thermal evaporation and self-assembled using a rapid thermal annealing system. The effect of the RTA heating rate on the NPs production reveals to be crucial to the decrease of the annealing process. The Ag NPs are integrated in thin film silicon solar cells to form a plasmonic back reflector that causes a diffused light reflectivity in the near-infrared (600–1100 nm wavelength region). In this configuration the thicknesses of the AZO spacer/passivating layers between NPs and rear mirror, and between NPs and silicon layer, play critical roles in the near-field coupling of the reflected light towards the solar cell absorber, which is investigated in this work. The best spacer thicknesses were found to be 100 and 60 nm, respectively, for Ag NPs with preferential sizes of about 200 nm. The microcrystalline silicon (µc-Si:H) solar cells deposited on such improved PBR demonstrate an overall 11% improvement on device efficiency, corresponding to a photocurrent of 24.4 mA/cm² and an efficiency of 6.78 %, against 21.79 mA/cm² and 6.12 %, respectively, obtained on flat structures without NPs.

3.3.1 Sample preparation

The PBRs (schematically shown in Figure 3.7) were fabricated with the structure: glass/Ag mirror (120 nm)/AZO/Ag NPs/AZO. The planar Ag mirror layers on glass were deposited by electron gun-assisted thermal evaporation technique, and the AZO [197] layers were deposited by RF magnetron sputtering. The Ag NPs were formed from the deposition of thin Ag layers at room temperature, by electron gun-assisted thermal evaporation, on glass with sizes at list 20 x 20 cm^2 followed by annealing under nitrogen atmosphere using a RTA system. A series of 6 nm Ag films were deposited on glass, previously coated with 60 nm of AZO, under the same conditions. The films were then annealed in RTA at 500 ˚C under nitrogen atmosphere, using different temperature ramp-up rates (ranging from 16 to 150 ˚C/s) and for different times (2-40 min) of steady-state (close to 500 ˚C) temperature.

The thickness of AZO layers between planar Ag film and Ag NPs ($d_{\text{Ag-NPs}}$) and the thickness between Ag NPs and n-doped µ-Si:H layer ($d_{\text{NPs-Si}}$) were varied and their influence in the PBR performance was evaluated.

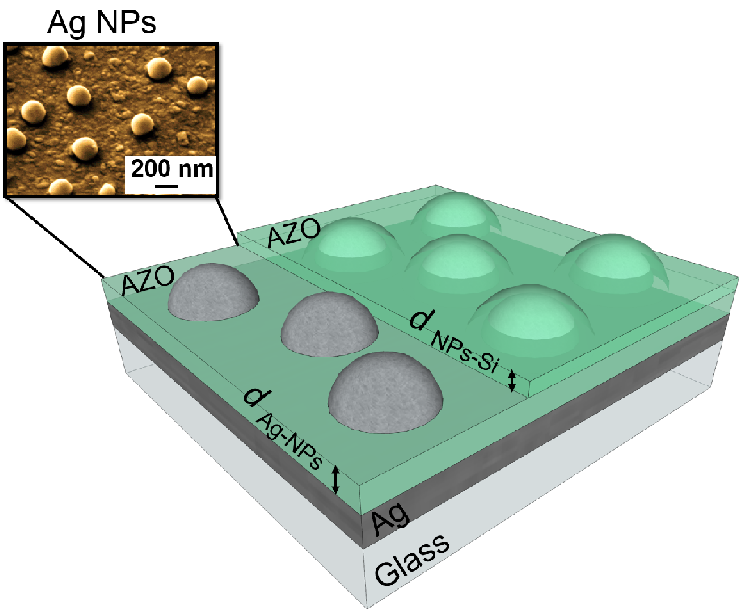

Figure 3.7 Schematic structure of a PBR consisting in the following layers stack: glass/Ag/AZO/Ag NPs/AZO. The bottom AZO layer below the Ag NPs separates the Ag planar mirror from the NPs, with a thickness d Ag-NPs. The other layer above the Ag NPs separates them from the μc-Si:H layers of the cell, with a thickness $d_{\text{NPs-Si}}$. The inset is a tilted SEM showing close-up images of the Ag NPs on an uncoated PBR.

Microcrystalline silicon solar cells, with an nip (substrate) configuration (shown in Fig. 3.14 (b)) were deposited on the PBRs at a temperature of 160 °C using a multi-chamber PECVD system [48], as described in section 2.5.2. The remaining deposition conditions of the nip Si layers are summarized in Table 3.2.

Table 3.2 Microcrystalline silicon layers thickness and deposition conditions: hydrogen dilution, D_H (%); dopant (trimethilboron or phosphine) ratio to silane, R_d (%); deposition pressure, p (Torr); power density, P_d (mW cm^{-2}); frequency, f (MHz).

Layer	Thickness (nm)	D_H (%)	R_d (%)	p (Torr)	P_d (mW cm^{-2})	f (MHz)
n	54	96.70	0.99	2.0	69.44	13.56
i	1500	95.90	-	1.0	138.89	75
p	20	99.29	0.56	2.4	90.28	13.56

3.3.2 Effect of the RTA heating rate and time of annealing on the NPs formation

Literature has demonstrated that the formation of Ag NPs suitable for LT via dewetting processes [198] usually requires an elevated annealing time, generally (1-4h) [12,56,187]. However, here we show that such time can be highly decreased by changing the temperature ramp-up rate of the annealing, which is a parameter hard to control in conventional systems (e.g. tube furnace, ovens) but can be easily tuned with RTA system as employed in this work. Figure 3.8 shows SEM images of Ag NPs formed at 500 °C during only 2 minutes, from a nominal precursor film thickness of 6 nm, with a temperature ramp-up rate ranging from 16 °C/s to 150 °C/s. Note that, for efficient light scattering for solar cell LT, we are mainly interested in growing semi spherical NPs with sizes > 100 nm. It is generally desirable to prevent the formation of smaller or irregularly-shaped NPs, as they are known to increase the parasitic absorption and/or lower the scattered intensity.

It can be observed that, by increasing the temperature ramp rate, a drastic morphological evolution occurs from a partially continuous film to a discontinuous dewetting pattern, and eventually disintegrating into isolated isotropic Ag NPs. For temperature ramp rates above 50 °C/s a NP structure is formed, instead of worm-like islands for lower rates, and at 150 °C/s there is a uniform distribution of appropriately sized particles. At such fast rate there is quick uptake of thermal energy by the precursor film which results in a more instantaneous kinetic transformation into particles and their consequent aggregation via material diffusion on the surface [187]. However, although 2 minutes is sufficient to form separated NPs, their geometry is not the best due to quite irregularly shaped and large particle aspect ratios.

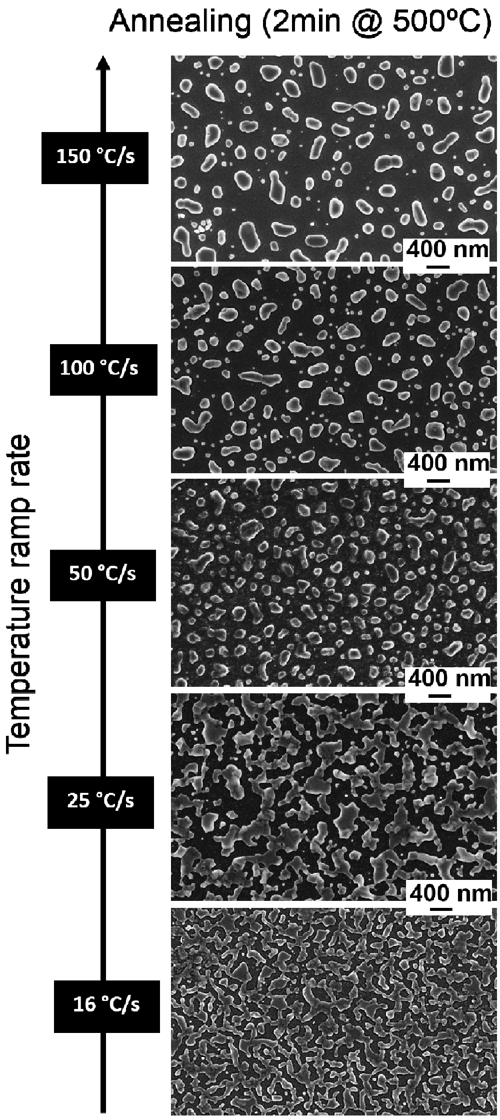

Figure 3.8 SEM images of Ag NPs formed on 30 nm AZO coated on glass after annealing at 500 °C from 6 nm precursor films with different temperature ramp-up rate and 2 min of annealing time.

More regular and semi-spherical NPs can be obtained by increasing the time or the temperature of the annealing process. The Ag NPs formed at temperatures higher than 500 °C (shown in Figure 3.9) have obvious improvements compared to the Ag NPs formed at 500 °C, since higher temperature promotes the coalescence of a large number of Ag islands. However, temperatures of 500 °C are enough to obtain uniformly distributed NPs on the BR, with large diameter (~200 nm on average), regular and semi-spherical shape.

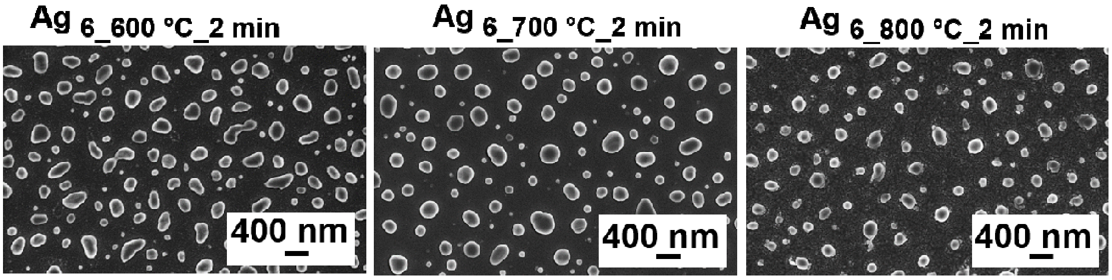

Figure 3.9 SEM images of Ag NPs formed after annealing (2 min) of precursor films with a thickness of 6 nm at 600 °C, 700 °C and 800 °C using the same temperature ramp rate (150 °C/s).

Figure 3.10 depicts the morphology of the NPs formed from 6 nm thick Ag precursor films, using the same annealing temperature and ramp-up rate (500 °C at 150 °C/s), but different steady-state annealing times between 5 and 40 min. By increasing the time of the annealing from the previous 2 min to 5 min, the worm-like Ag islands (see Figure 3.8) evolve into more regularly isotropic NPs.

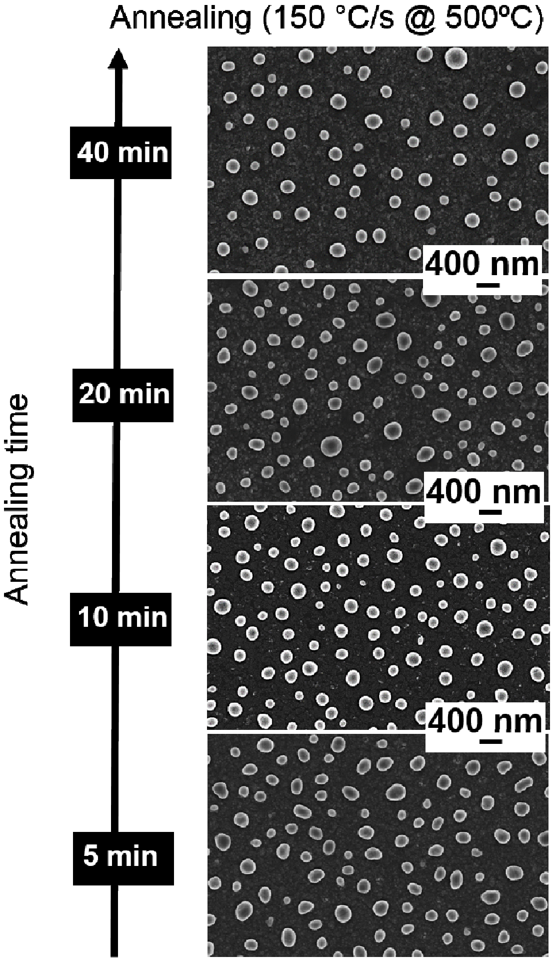

Figure 3.10 SEM images of Ag NPs formed from 6 nm thick Ag films, at the same temperature and ramp rate (500 °C at 150 °C/s), but different annealing times, between 5 and 40 min.

Upon further incrementing annealing time to 10 min or more, the NPs become progressively more semi-spherical, the number of smaller NPs (<100 nm) reduces via coalescence with bigger particles and the inter-particle space increases. It was found that, under these conditions, the morphology of the NPs structure does not change considerably for annealing times of 10 min or higher.

3.3.3 Effect of the AZO spacer layer between Ag film and Ag NPs on TF μc-Si solar cell performance

First, we will discuss the effect of the bottom AZO layer, with thickness $d_{\text{Ag-NPs}}$, on the morphological and optical performance of the PBR and their influence on the performance of the solar cell. We measured by SEM (not shown here) the height together with the size (in-plane diameter) histograms of Ag NPs formed on AZO layers with different $d_{\text{Ag-NPs}}$, and we found that $d_{\text{Ag-NPs}}$ had no significant effect on the morphology of the fabricated Ag NPs for $d_{\text{Ag-NPs}}$ from 30 to 140 nm (shown in Figure 3.11). The trends obtained in Figure 3.11 are in accordance with those determined by Tan et al. [59]. For $d_{\text{Ag-NPs}}$ lower than 30 nm the formation of a thin film occurs (Figure 3.12).

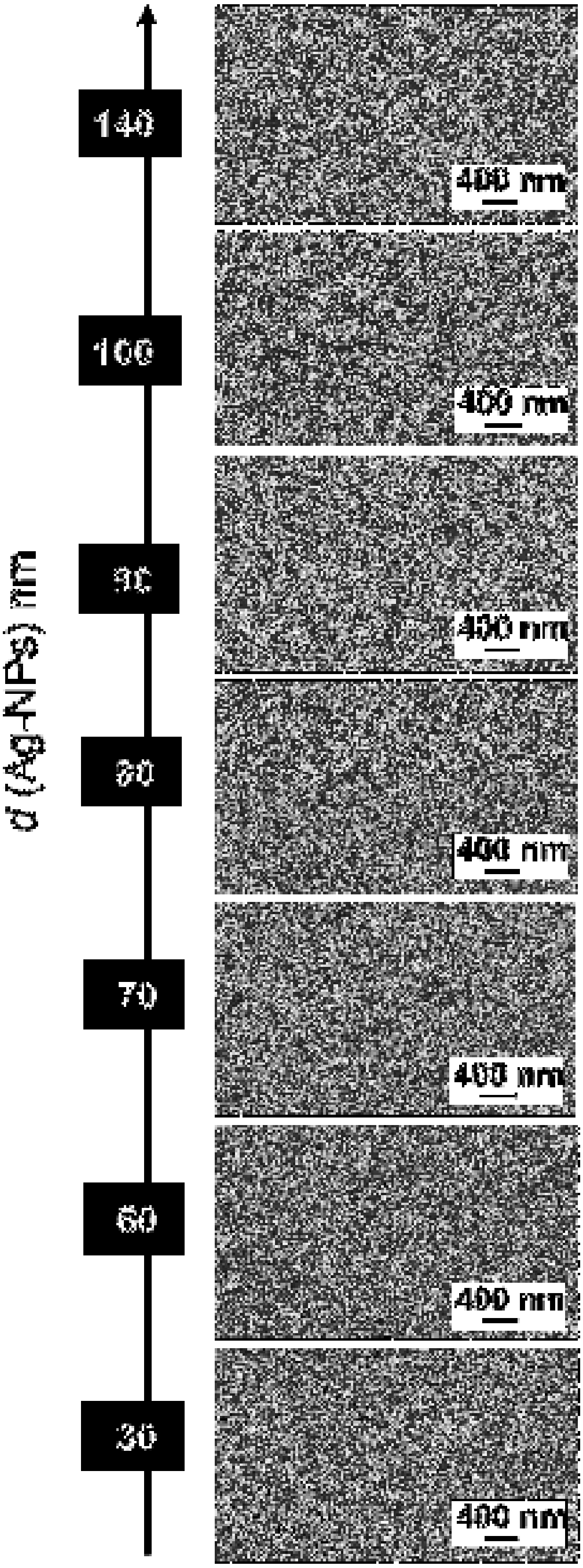

Figure 3.11 SEM images of Ag NPs deposited on PBR configuration (glass/Ag/AZO) for thicknesses of AZO (*d* Ag-NP) between 30 and 140 nm. The NPs are formed after annealing of precursor films with a thickness of 6 nm for 10 min at 500 °C with a temperature ramp rate of 150 °C/s.

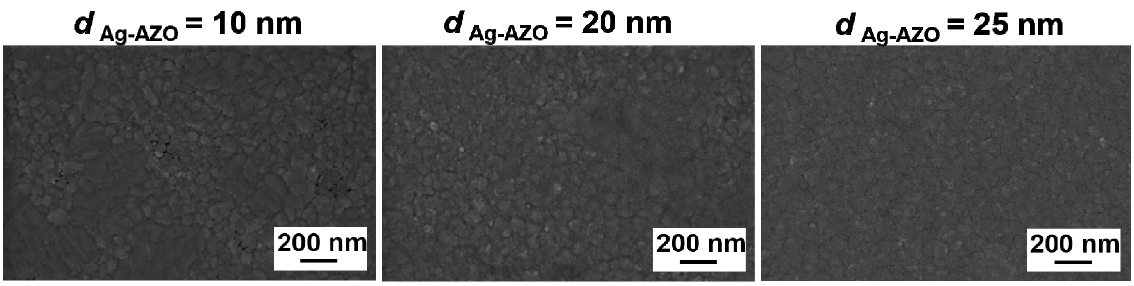

Figure 3.12 SEM images of Ag NPs deposited on PBR configuration (glass/Ag/AZO) for thicknesses of AZO ($d_{\text{Ag-NPs}}$) lower than 30 nm. The NPs are formed after annealing of precursor films with a thickness of 6 nm for 10 min at 500 °C with a temperature ramp rate of 150 °C/s.

The reflective properties of PBRs with different $d_{\text{Ag-NPs}}$ are presented in Fig. 3.13, which shows the values of the average total ($\langle R_{TOT} \rangle$) and diffuse ($\langle R_{DIF} \rangle$) reflectance in the 600–1200 nm wavelength range corresponding to the preferential LT window of μc-Si:H solar cells.

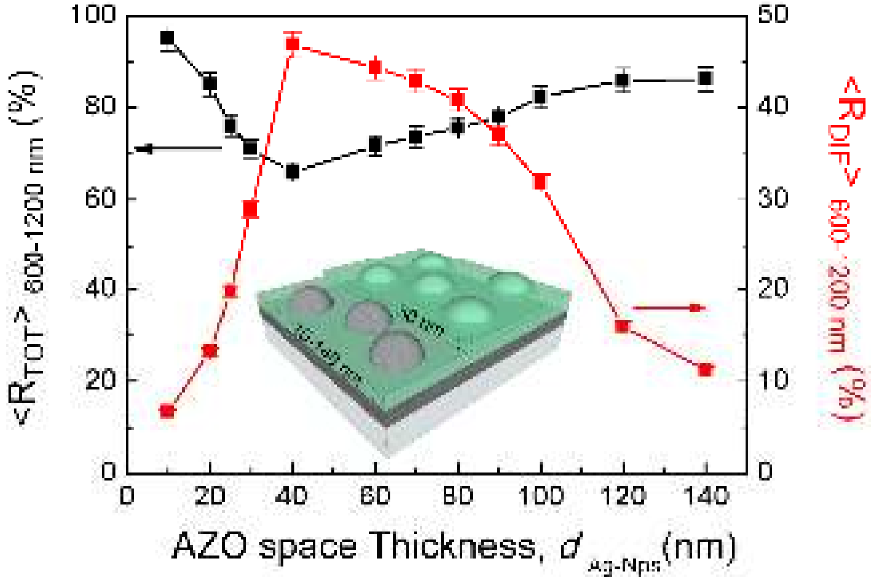

Figure 3.13 (a) Total reflectance (<RTOT>) and diffuse reflectance <RDIF> averaged over the 600–1200 nm spectral range for Ag NPs formed from 6 nm thick Ag films, at the same temperature and ramp-up rate (500 °C at 150 °C/s) during 10 min, with varying thickness of AZO layer between the mirror and the particles ($d_{\text{Ag-NPs}}$). The plotted points have an associated error bar estimated by analyzing, for each point, sets of 3 samples fabricated with the same parameters.

It can be observed that for $d_{\text{Ag-NPs}} = 40$ nm the diffuse reflectance reaches a maximum and the total reflectance a minimum. For thicknesses higher than 40 nm, the thinner the spacer the higher the R_{DIF}, due to increased near-field interaction between the MNPs and the Ag mirror which enhances the scattering efficiency of the nanoparticles [23]. On the other hand, the total reflectance decreases with the proximity to the mirror, which means that such interaction also contributes to the parasitic absorption of the PBR. Interestingly, for separation distances lower than 40 nm, the diffuse reflectance decreases and the total reflectance increases. At very close distances to mirror, i.e. between 10 and 20 nm, the diffuse reflectance is significantly lower because of the formation of a thin film, due to the elevated degree of coalescence there is no formation of isolated nanoparticles (see Figure 3.12). The trends obtained in Figure 3.13 are in accordance with those determined by Sesuraj *et al.* [190] and demonstrate that, for a given MNP distribution, the scattering spectrum of the PBR can be optimized by tuning the AZO spacer layer.

To investigate the light trapping performance of the PBRs, microcrystalline silicon (μc-Si:H) solar cells with an n-i-p configuration (Fig. 3.14) were deposited in the same deposition run by PECVD.

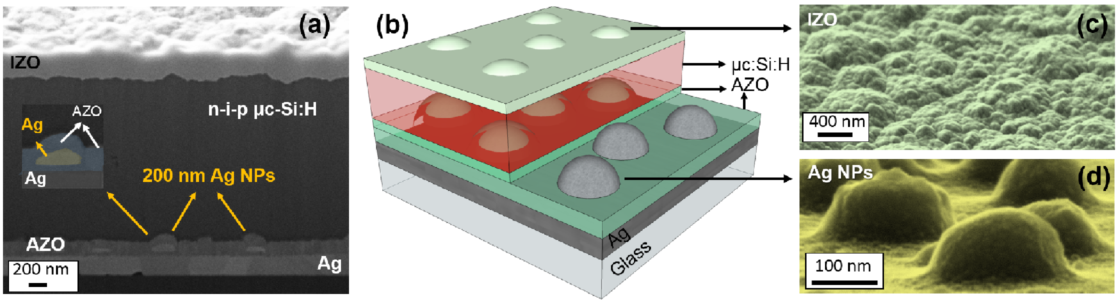

Figure 3.14 (a) SEM of the solar cell inner cross-section obtained by milling the layers with FIB, showing a zoom on an MNP embedded in the AZO layers. The solar cells deposited on the PBRs, depicted in (b), present ~200 nm hemispherical corrugations/domes on the top IZO surface (see tilted SEM in (c)) formed from the conformal deposition of material over the NPs (cross sectional SEM in (d)).

Figure 3.15 (a) shows the total and diffuse reflectance of PBRs with 40 and 100 nm $d_{\text{Ag-NPs}}$. Figures 3.15 (b) and (c) show the total absorption (1-R) and external quantum efficiency (EQE) curves of the solar cells deposited on such PBRs, compared with those of a reference planar device deposited on a similar back reflector (120 nm Ag/60 nm AZO) but without NPs. For wavelengths above 720 nm, both the EQE and total absorption are significantly enhanced (averaged total absorption and EQE improved by 62% and 45.3%, respectively) in comparison to the planar cell. At such long wavelengths, the improved EQE can be attributed to the strong scattering of light in the NIR by the Ag NPs, which increases the optical path length in the photoactive layer compared to the flat BR.

The solar cells were constructed on several PBRs with different $d_{\text{Ag-NPs}}$ from 10 to 120 nm, and the maximum photocurrent density (J_{ph}) was found for $d_{\text{Ag-NPs}}$=100 nm (Figure 3.15 (c)). This is attributed to a lower parasitic absorption of the $d_{\text{Ag-NPs}}$=100 nm PBR throughout most of the spectrum, particularly when compared with PBRs of lower $d_{\text{Ag-NPs}}$ (see Figure 3.13), while maintaining high NIR scattering performance [59,190].

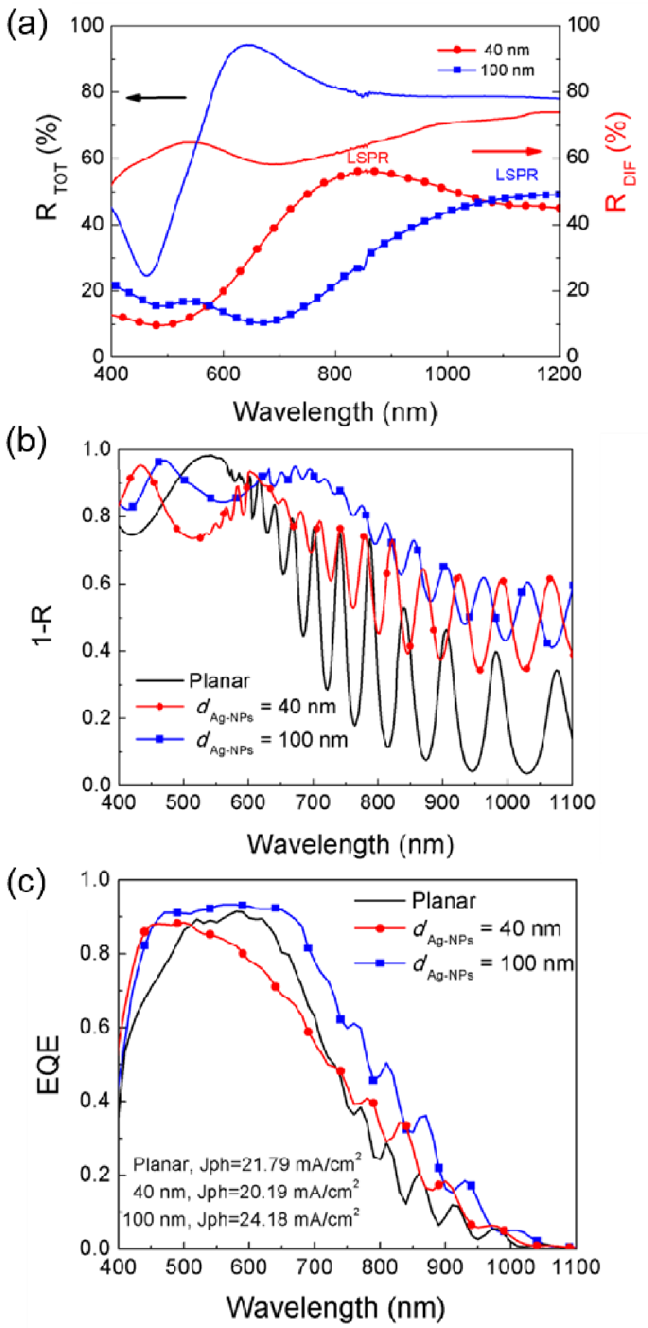

Figure 3.15 (a) Total reflection (R_{TOT}) and diffuse reflectance (R_{DIF}) of plasmonic BRs with $d_{\text{Ag-NPs}}$ of 40 and 100 nm. EQE (b) and total absorption (1 – R) (c) curves of 1.5 µm thick µc-Si:H solar cells deposited on planar and in two plasmonic back reflectors with AZO thickness $d_{\text{Ag-NPs}}$ of 40 and 100 nm. The photocurrent density (J_{ph}) values of the solar cells are indicated in (c).

At wavelengths between 550 and 720 nm, the EQE of the 40 nm $d_{\text{Ag-NPs}}$ PBR decreases abruptly when compared with both the planar cell and PBR with 100 nm $d_{\text{Ag-NPs}}$, due to its higher parasitic absorption, as indicated by its much lower R_{TOT} curve in Figure 3.15

(a). Therefore, a compromise should be considered between the scattering and parasitic absorption when choosing the particle-mirror distance. At short wavelengths (400 – 550 nm), the EQE attained with the PBRs of 40 and 100 nm $d_{\text{Ag-NPs}}$ is almost the same, since such light is fully absorbed in a first pass along the Si layer and does not reach the rear part of the cell. Despite that, a strong enhancement in EQE and total absorption is observed relative to the planar reference, which can only be explained by the anti-reflection action of the front surface texturing (see top corrugations in Figure 3.14 (c) resulting from the conformal deposition of the material over the NPs. Such hemispherical corrugations on the cell front cause geometrical index matching between the incident light and the Si layer, which can strongly reduce the light reflected off the illuminated surface [199].

The main J-V parameters of the μc-Si:H solar cells are summarized in Table 3.3. The solar cells deposited on PBRs yield slightly lower (for $d_{\text{Ag-NPs}}$=40 nm) or higher ($d_{\text{Ag-NPs}}$=100 nm) photocurrent relative to the planar cell, but the fill factor (FF) and Voc decrease significantly for both cases. The sharp valleys around the Ag NPs (see Figure 3.14), and their overall induced roughness, can create cracks near the n/i interface and even propagating inside the intrinsic layer. These can act as shunting paths and/or charge trapping sites that reduce the device electrical performance. Such a deterioration of FF and Voc has been a common issue in LT schemes [23,200]. Nevertheless, the photocurrent gains attained with properly tuned PBRs can compensate such electrical losses and result in clear efficiency enhancement, as attained for the $d_{\text{Ag-NPs}}$=100 nm case.

Table 3.3 Opto-electronic parameters of solar cells deposited on different BRs

	Voc (V)	Jph (mA/cm^2)	FF (%)	η (%)
Planar	0.43	21.79	65.36	6.12
$d_{\text{Ag-NP}}$ = 40 nm	0.41	20.19	63.50	5.23
$d_{\text{Ag-NP}}$ = 100 nm	0.42	24.18	64.96	6.59

3.3.4 Effect of the AZO spacer layer between Ag NPs and n-doped layer on TF μc-Si solar cell performance

The PBRs analyzed so far had a 30 nm AZO spacer layer between the Ag NPs and the Si material. Figure 3.16 shows how the EQE and J-V parameters of solar cells change when deposited on PBRs with a thicker (60 nm) AZO spacer layer. When the $d_{\text{NP-Si}}$ is increased from 30 to 60 nm, the J_{ph} increased from 24.180 to 24.376 mA/cm^2, while the Voc and FF also improved. This may be ascribed to an improved morphology of the top surface coating the particles, which is beneficial for the growth of dense μc-Si:H materials with less defect density. The thicker AZO layer on the Ag NPs assists in flattening their sharp surface features [23,200] and also in preventing the diffusion of metallic contaminants to the Si material, which is particularly crucial during the plasma enhanced deposition. Further improvement is not observed as the thickness is increased beyond 60 nm.

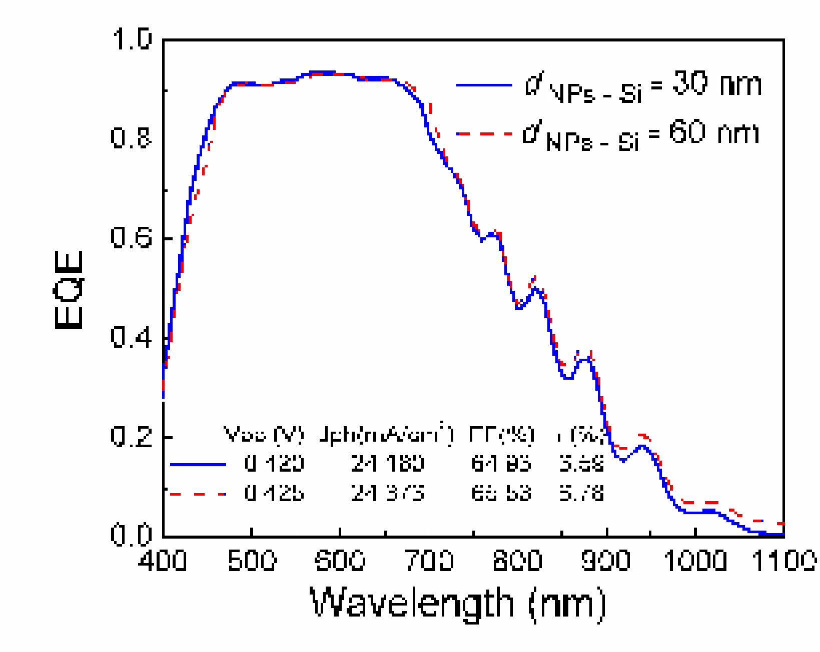

Figure 3.16 EQE of solar cells deposited on the PBRs with 30 and 60 nm thick AZO layers on top of the Ag NPs. The inset table shows the J-V parameters of the solar cells.

3.4 Conclusions

The resonant nature of plasmonic light scattering makes it crucially dependent on the physical properties of the scattering objects. Therefore, its successful application in any opto-electronic device, such as for light trapping in the near-bandgap spectral range of TF SC, requires a precise control of the geometry of the MNPs. Nanoparticle sizes appropriate for far-field light scattering (> 100 nm) have so far been achieved with dewetting by adjusting the thickness of the precursor Ag film or the annealing temperature. However, it has remained difficult to obtain large and regularly shaped Ag MNPs with low surface coverage, since thicker precursor films tend to form non-uniform MNP geometries.

In this chapter, we investigated another route to engineer the desired particles' morphology by analyzing the influence of the underlying surface material on the MNPs self-assembly. It was shown that parasitic absorption is reduced and scattering is enhanced by forming Ag NPs on a thin (30 nm) AZO film, with good conductivity (σ = 59.5 Scm^{-1}) and low surface roughness, which yielded relatively large (100-300 nm) particles with a semi-spherical shape and an 8% surface coverage. The MNP arrays formed on such AZO film present the best morphological properties relative to the nanostructures formed on films with higher thicknesses or resistivity, as they exhibit highly regular particles with the appropriate geometries and low surface coverage. This study points out the important routes to select the best surface properties for the self-assembly of Ag MNPs in view of their application on the TCO layers of thin film photovoltaic devices.

An ultra-fast rapid-thermal annealing strategy is presented to fabricate top-performing plasmonic back reflectors for light trapping in thin film Si solar cells. The fabrication and optical studies presented here show that a rapid heating (i.e. temperature ramp-up) rate is very beneficial to ensure the formation of Ag NPs with favorable monodispersed geometries in a short annealing time.

The performance of the PBRs was improved by careful adjustment of the AZO spacer layers separating the NPs from both the rear mirror and the μc-Si:H absorber, to yield maximum light trapping (low parasitic absorption and high NIR scattering) with minimum degradation of the cells' electrical properties. The best performing PBR was found to have the structure: 120 nm Ag/100 nm AZO/Ag NPs/60 nm AZO, with the Ag NPs formed from a 6 nm precursor Ag film annealed at 500 ºC for 10 min after a rapid 150 ºC/s temperature ramp-up rate. Such PBR provided a photocurrent and efficiency enhancement of 10.6% and 9.8%, respectively, relative to the solar cell reference with a planar rear reflector structure: 120 nm Ag/60 nm AZO.

Chapter 4

Silver Nanoparticles by Dewetting Process for SERS Application

The aim of this chapter was to develop highly efficient surface enhanced Raman spectroscopy (SERS) constructed on low-cost, fully recyclable and highly reproducible paper substrates. The active optical component is based on plasmonic silver nanoparticles deposited by a one-step methodology, without any post-deposition thermal procedures. Different type of cellulose substrates and strategies to enhance the SERS signal were tested and their influence on the SERS signal, uniformity and stability investigated.

The results demonstrate that the control of Ag NPs particle sizes, inter-Ag-NPs gaps, sensing area, concentration of Ag NPs or new architectures, like 3D structures, are crucial to increase the SERS signal of the substrates. It is then shown that the stability of the SERS platforms can be greatly enhanced on substrates with a metal layer located close to the MNPs. The final results showed that a remarkable 10^9 signal enhancement was obtained using R6G (10^{-8} M) as the test analyte, on a new kind of flexible and cost-efficient SERS substrate (cardboard plates). Besides such advantages, cardboard substrates proved to be uniform and stable SERS platforms.

This chapter contains relevant information from the publication:

Araújo A, Caro C, Mendes M J, Nunes D, Fortunato E, Franco R, Águas H and Martins R 2014 Highly efficient nanoplasmonic SERS on cardboard packaging substrates. *Nanotechnology* **25** 415202.

Araújo A, Pimentel A, Oliveira M J, Mendes M J, Franco R and Fortunato, Elvira, Águas, Hugo, Martins R 2017 Direct growth of plasmonic nanorod forests on paper substrates for low-cost fl exible 3D SERS platforms *Flex. Print. Electron.* **2** 014001.

Pimentel A†, Araújo A† (equal contribution), Beatriz J, Coelho D N, Oliveira M J, Mendes M J, Águas H, Martins R and Fortunato E 2017 3D ZnO/Ag Surface-Enhanced Raman Scattering on Disposable and Flexible Cardboard Platforms *Materials* **10** 1351

4.1 Highly efficient nanoplasmonic SERS on cardboard packaging

This work reports on highly efficient surface enhanced Raman spectroscopy constructed on low-cost, fully recyclable and highly reproducible cardboard plates, which are commonly used as disposable packaging material. The active optical component is based on plasmonic silver nanoparticle structures separated from the metal surface of the cardboard by a nanoscale dielectric gap. The SERS response of the Ag nanoparticles of various shapes and sizes was systematically investigated, and a Raman enhancement factor higher than 10^6 for rhodamine 6G detection was achieved. The spectral matching of the plasmonic resonance for maximum Raman enhancement with the optimal local electric field enhancement occurs using 60 nm-sized Ag NPs, as predicted by the electromagnetic simulations, which reinforces the outstanding results achieved. Furthermore, the nanoplasmonic SERS substrates exhibited high reproducibility and stability. The SERS signals showed that the intensity variation was less than 5% along the substrate area, and the SERS performance could be maintained for up to at least 6 months.

4.1.1 Introduction

MNPs can generate intense electromagnetic field enhancements, via localized surface plasmon resonance effects. At resonance, MNPs can produce particularly intense localized near-field and propagating far-field scattering; however, these features depend intrinsically on the size, shape and spacing of the MNPs as well as on their surrounding environment [11,40,119,120,201]. SERS takes advantage of the near field scattering, leading to highly amplified Raman scattering signals close to the surface of the NPs. Therefore, the Raman signal from molecules can only be increased if they are located directly in contact or at least in the vicinity of the MNPs [15]. This localized enhancement effect allows detecting extremely small amounts of analytes, making SERS an efficient tool for detection of a variety of problems, including corrosion, detection of chemical warfare agents, bacteria on food, trace evidence in forensic science, blood, glucose, among others [202–205].

Currently, the most frequent method for producing MNPs with nanoscopic controlled geometry and inter-particle distance is employing advanced lithographic processes, such as e-beam lithography [167]. However, this method has crucial drawbacks such as high patterning time and elevated costs, which limits its extensive use in macroscopic scale systems. Alternative large scale processes such as chemical synthesis [143,169,170,206], physical deposition with PDA [12] or template and electrodeposition [89] are also commonly applied. However, several processing steps are required, despite the fact that PDA, for example, requires elevated temperature conditions. Merlen *et al* [207] showed the potential of fabricating MNP structures at room temperature using a sputtering technique with short deposition time (a few seconds) under primary vacuum, without post-annealing. However, this process does not allow for a fine control of the size, shape and organization of NPs, hindering the direct correlation between the NPs morphology and the resulting SERS signal intensities; but it can be advantageous for the fabrication of novel SERS nanostructures such as metal-coated dielectric nanorod arrays [125].

Metal deposition by e-beam evaporation results in the direct arrangement of individual NPs, with a good control of size and shape, without any post-deposition thermal procedure. This methodology consists of one step only. Ag NPs are formed in situ during the thermal evaporation of thin films of Ag onto substrates heated at 150 ºC. The low temperature nanoparticle formation method developed in this work is largely applicable to a broad range of substrate materials (e.g. flexible ones) which would not be compatible with standard post-annealing dewetting methods carried out at high temperatures (300-500ºC) [12,73,175]. Nevertheless, suitable substrate heating is imperative in order to favor the material surface diffusion during deposition, and avoid worm-like structures [12,171]. This process revealed to be relatively simple and inexpensive for the preparation of SERS substrates with improved stability, uniform morphology and exhibiting pronounced Raman enhancement effects throughout large-scale areas.

Intense efforts have been made in order to find cost-efficient SERS substrates, such as paper substrates [127,143–146,163,208]. In fact, paper has been widely used as a low-cost platform for medical diagnostic [147,148,209], analysis and/or quality control devices [150,210].

In this work, we developed a new kind of SERS substrate based on cardboard. This particular substrate is an aseptic and biodegradable material that is widely used in several applications such as the packaging of food and in the beverage industry. Cardboard substrate, like common paper, is cost-efficient, highly sensitive, and amiable to several different environments and target analytes. In addition, is extremely robust when compared to common paper substrates. Here, we demonstrate the feasibility of nanoplasmonic cardboard substrates for reproducible and stable SERS substrates, with a tunable visible resonance. We show that Ag nanoplasmonic cardboard substrates prepared by an alternative one-step thermal evaporation method, for arrangement of individual SERS active NPs, exhibit a very strong SERS activity, using R6G as Raman probe.

4.1.2 Sample preparation

The cardboard packaging substrates used in this study consist of pressed cellulose fibbers, polymeric coatings and evaporated aluminium. The polymeric portions of the paper promote the proper adhesion of the metalized layer to the cellulose and protect the thin metalized layer from scraping or other environmental damage. Moreover, a thin native oxide (Al_xO_y) layer is present on the top of the aluminium layer. The presence of such surface oxide is essential for the formation of metallic NPs by the solid-state dewetting method.

Ag NPs were obtained by deposition of metal layers directly on cardboard substrate (2.5×2.5 cm^2) using electron-gun assisted thermal evaporation technique. The substrate was kept at 150 °C during the thermal evaporation while the thicknesses of Ag films was ranging from 2 to 12 nm (described in section 2.1.3.1). SERS substrates were prepared by dropping 100 µl of R6G solution with a concentration of 10^{-6} M onto the substrate (described in section 2.5.2). Figure 4.1 represents a schematic of the production process of Ag NPs by e-beam on cardboard substrates for SERS application.

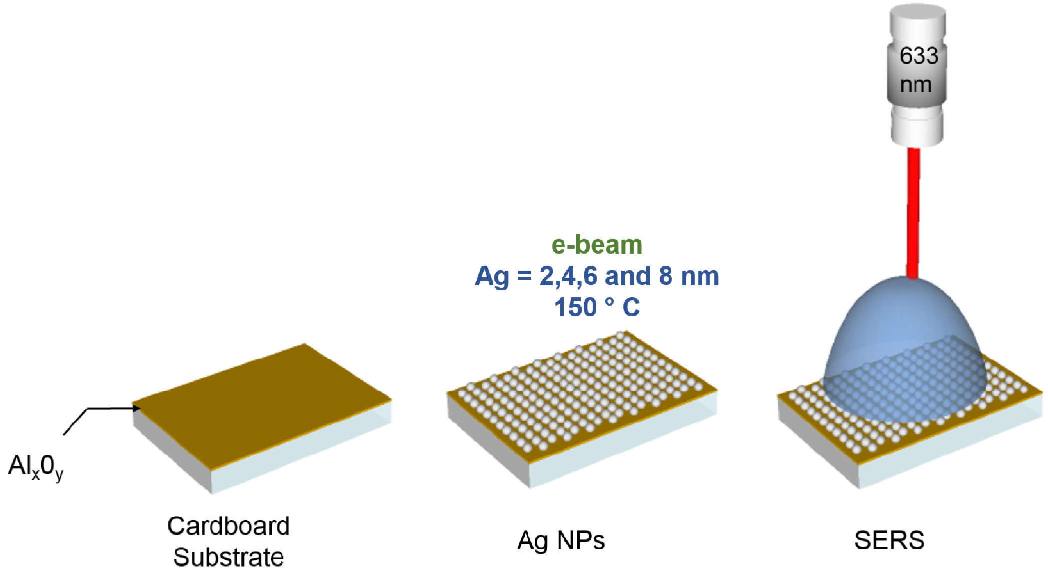

Figure 4.1 Schematic of the production of Ag NPs by e-beam on cardboard substrates, for SERS application.

4.1.3 Ag nanoparticles formed on cardboard substrate

4.1.3.1 Substrate characterization

As demonstrated in previous studies, MNPs have high SERS effect [89,169,211–213]. So in this work we fabricated the metal nanostructures to enhance the Raman signal of

R6G by thermal evaporation assisted by electron-beam method, using an alternative SERS substrate. Scanning electron microscopy and atomic force microscopy analyses of the cardboard substrates before and after the NPs deposition have been carried out (Figure 4.2). Figure 4.2 a) and Figure 4.2 b) show the surface morphology of the cardboard substrates before Ag NPs deposition. The surface roughness of the cardboard substrate lies in the micrometer range. Nevertheless, at the nanoparticle level, the root mean square (RMS) is 2.37 (±0.05) nm as determined by AFM (Figure 4.2 b).

Ag films are successively deposited onto cardboard surface by the similar method. The surface morphology evolution of the NPs for Ag mass-equivalent layer thickness (hereafter designated as *mass thickness*) ranging from 2 to 8 nm are show in Figure 4.2 c).

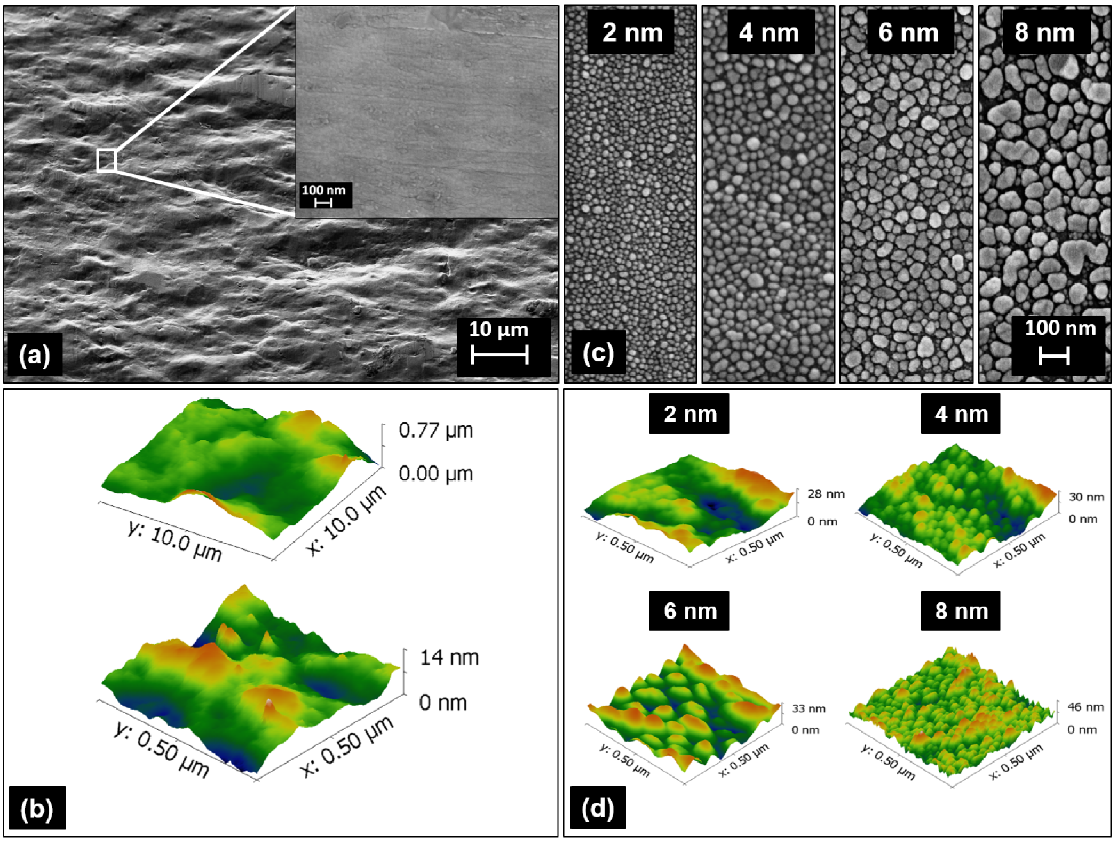

Figure 4.2 (a) SEM and (b) AFM images showing the cardboard packaging surface at two distinct magnifications. (c) SEM images showing the uniformly dense surface of cardboard substrates covered with Ag NPs obtained from different Ag mass thickness, and (d) corresponding AFM images.

Despite the inherent heterogeneity of the cardboard packaging substrate, SEM images revealed a highly dense and uniform distribution of Ag NPs along the substrates, without large scaled agglomerates. The uniformity of the nanostructures produced by thermal evaporation greatly contributes to the high reproducibility of SERS, as the laser spot covers a range of tens of microns containing several thousands of particles. Thus, a large ensemble of illuminated NPs affects the resulting signal.

Figure 4.3 depicts the temperature-dependent mass change (TG) and temperature-dependent heat flux (DSC) results for laminated cardboard substrate (sample mass: 21 mg). One endothermic peak was detected at 99.3 °C temperature with a weight loss of 6.6 % (A) which is due to the release of adsorbed water. Above 250 °C one mass loss step of 57.7 % (B) occurs when the substrate starts to decompose. Therefore, the cardboard packaging substrate maintains its properties up to temperatures of 250 °C.

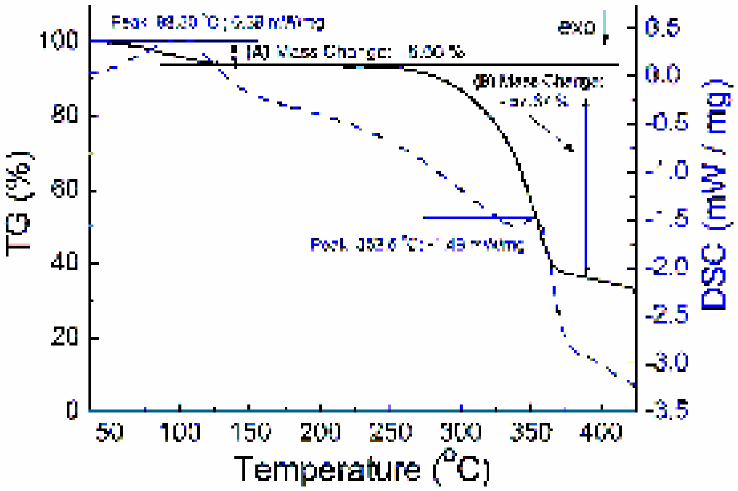

Figure 4.3 Temperature-dependent mass change (TG), and heat flux (DSC) signal of cardboard substrate.

4.1.3.2 Morphological and optical properties of NPs

Figure 4.4 presents colour plots with the distribution of the particles in-plane semi-axes, for four different Ag mass thicknesses. The 2 nm mass thickness NPs exhibited mostly semi-spherical shapes. With increasing mass thickness increases from 2 to 6 nm, the NPs shape becomes more irregular, elongated (with semi-ellipsoidal shape) and larger in size, as observed by SEM images (Figure 4.4 (c)). Recently, Eshwar Thoutis et al. [175] reported a similar thickness-dependent morphology evolution of nanostructures fabricated by thermal evaporation with a post annealing step at 200 °C. The Ag NPs evolved into an elongated shape and became larger in size as the mass thicknesses increased.

AFM measurements of the NPs with mass thickness of 4 and 6 nm revealed an average height of approximately 30 and 46 nm, respectively (Figure 4.4 (d)), with typical in-plane ellipsoid axes ratios of ~1.3. For mass thicknesses of 8 nm or higher, heterogeneously distributed NP sizes were observed, which is evidenced by the strong increase of particles smaller than 40 nm and bigger than 80 nm. This heterogeneity is clearly visible in Figure 4.4 (c) and originates a double-peak in the corresponding distribution histogram.

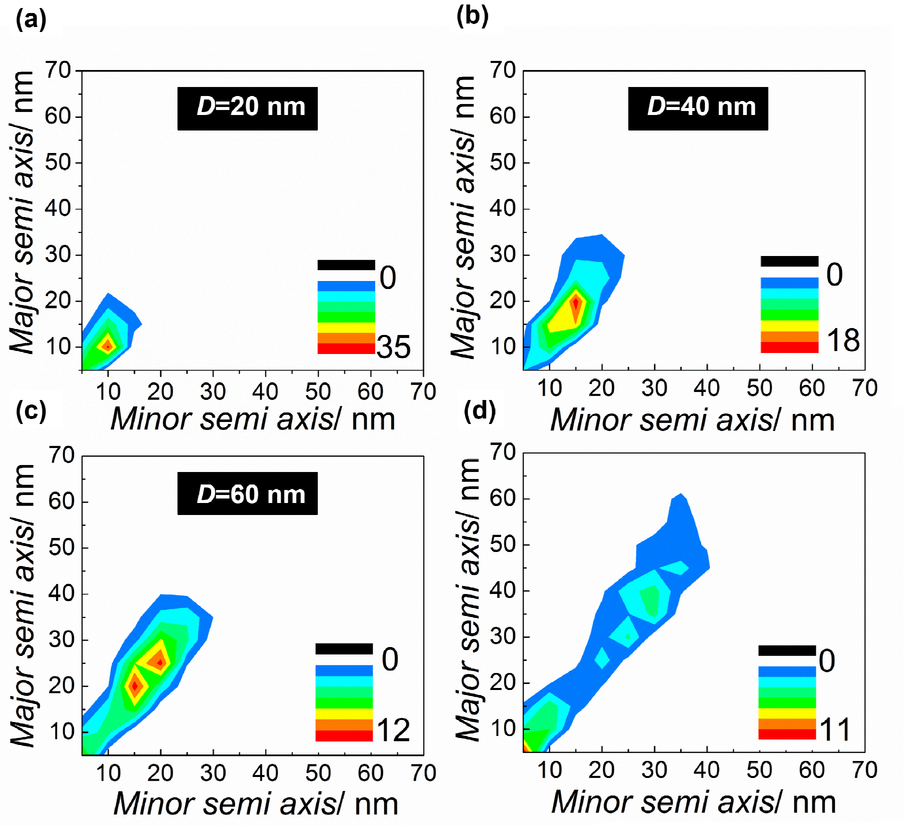

Figure 4.4 Histogram distributions of the Ag NPs for the 2 (a), 4 (b), 6 (c) and 8 (d) nm mass thicknesses. The values for the average size (in-plane major axis, D) of the deposited Ag NPs are indicated for samples with 2, 4 and 6 nm mass thicknesses. Mass thicknesses of 8 nm or higher resulted in heterogeneous dispersions of NP sizes, for which the average size is not presented.

To study the LSPRs spectral positions of the SERS substrates and, hence, the wavelength range in which the structures can be useful for SERS applications, the absorptance spectra (Figure 4.5), determined from the total reflectance (R_{ToT}) spectra before and after Ag NPs deposition.

SERS substrates presents two characteristic peaks. The shorter wavelength peaks correspond to quadrupole resonances (sharp peaks at ~ 400 nm), whereas the broader peaks at longer wavelengths (centered approximately around the used laser wavelength) correspond to the dipolar resonances of the Ag NPs [119]. The increase of Ag mass thickness leads to an increase in the average particle size and more elongated semi-ellipsoidal shapes, as previously mentioned, which in turn results in red-shift and broadening of the LSPR peaks [214]. These nanoplasmonic SERS substrates providing different plasmon resonances in the visible, allow direct correlation between the NPs plasmonic properties, the used excitation wavelength, and observed SERS signal intensities. Photographs of the SERS substrates with 2, 4, 6 and 8 nm mass thicknesses (see insets in Figure 4.5) reveal that a preliminary assessment of the NPs differences, and LSPR spectral position, can be estimated by simple visual inspection of the substrate colours.

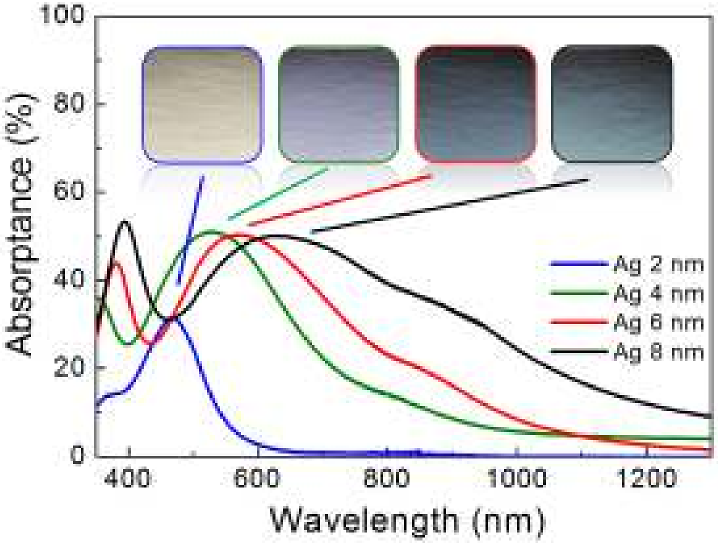

Figure 4.5 UV-Vis-NIR absorption spectra of cardboard packaging substrates after Ag NPs deposition with 2, 4, 6 and 8 nm Ag mass thicknesses. Photographs of the NP-coated substrates are presented above the spectra.

4.1.4 Near field light enhancement

Standard optical measurements as those of Figure 4.5 can only detect the far-field light extinction caused by the particles, but do not allow the probing of their near-field light scattering responsible for SERS [120]. To investigate the localized near-field light enhancement originated in the vicinity of Ag NPs, electromagnetic models can be used such as the single-particle Mie theory formalism [120]. This analytical method is based on a spherical particle immersed in an infinite homogeneous medium. This condition does not contemplate the semi-hemispherical Ag NPs deposited on the cardboard packaging substrates. Nevertheless, Mie theory can still be used to estimate the order-of-magnitude of the electric field intensity scattered at the vicinity of each particle. For that, it has been considered a spherical Ag nanoparticle surrounded by a homogeneous medium with an effective refractive index between alumina (native oxide layer at the surface of the aluminium-coated cardboard) and air [199].

When the particle is illuminated by a plane wave incident from the top (depicted in the inset of Figure 4.6), with a wavelength higher than the particle diameter (D), a dipolar-like near-field pattern is produced with an intensity maximized when the wavelength matches the LSPR of the nanoparticle [13]. The solid curve in Figure 4.6 shows the scattered electric field intensity ($|\mathbf{E}_S|^2$) at the LSPR wavelength of the particle, at the point of maximum field enhancement located in the intersection between its equator and the incident field ($\mathbf{E}_o$) direction.

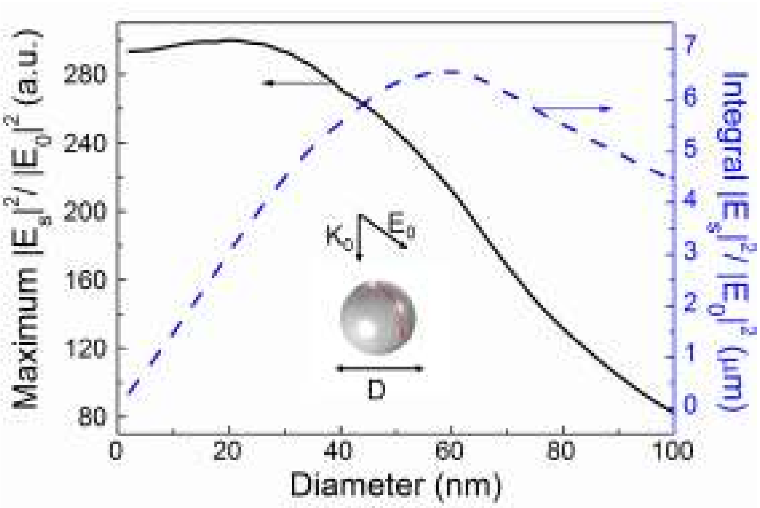

Figure 4.6 Maximum scattered electric field (E_S) intensity, in units of the incident electric field (E_0) intensity, produced at the LSPR of a Ag nanosphere, as a function of the particle diameter (D). The sphere is illuminated by a plane wave with wavevector K_0 and is immersed in an uniform medium with an effective refractive index between alumina (Al_2O_3) and air. *Dashed line* – Integral of $|E_S^2|/E_0^2|$ along the solid line on the surface of the sphere, in the E_0, K_0 plane.

For small nanoparticle sizes (D < 30 nm), the near-field intensity remains almost invariable, as particles scatter in the purely-dipolar electrostatic regime. When the diameter increases, retarded potentials start influencing the plasmonic oscillations, causing deviations from the fundamental dipolar mode. Thus, higher-order LSPRs appear in the scattering spectra together with the highly localized dipolar near-field enhancement exhibited by the Ag NPs, which is, in turn, reduced.

For molecular detection in SERS, it is vital not only to allow a strong electric field enhancement in the vicinity of the NPs, but also to have the largest area with such enhancement. Therefore, the determination of the optimal particle size must take into account that smaller MNPs exhibit higher E_S intensities while larger MNPs have more surface area for Raman-active molecules to attach and be illuminated by the scattered near-field. The preferable particle size for SERS detection can be estimated by the integral of the scattered field enhancement along the line segment depicted on the surface of the sphere of Figure 4.6. Such integration is performed only along a quarter of the perimeter of the sphere due to the symmetry of the dipolar scattering pattern and to the unpolarized nature of the illuminating light, with $\mathbf{E_0}$ at any direction orthogonal to the direction of incidence. The integral values presented in Figure 4.6 increase almost linearly in the electrostatic small-particle size range (D < 30 nm), peak at D = 59.3 nm, and decrease for larger particle sizes. Hence, according to the morphological characteristics of the MNP structures presented in Figures 4.2 the desirable particle sizes for molecular SERS detection correspond to those with the 6 nm Ag mass thickness, in which the majority of the MNPs have sizes around 60 nm.

4.1.5 Implementation of plasmonic cardboard substrate as SERS device

4.1.5.1 Maximum SERS intensity with an excitation wavelength λ_{exc}

It is well known that the plasmonic resonances of the particles are strongly dependent on their surrounding dielectric environment (including substrate, solvent, and adsorbates) [201,215–217]. Therefore, the LSPR spectral positions will change upon deposition of the molecule. For that reason, the produced LSPR shift has been optically reanalyzed before performing the Raman measurements. R6G molecules were adsorbed onto the SERS substrates by drop casting a 10^{-6} M R6G aqueous solution onto the substrates, followed by drying at 80 °C for 10 min. The absorption spectra (Figure 4.7) revealed that the LSPR peaks were red-shifted and broadened, when compared to those of Figure 4.5, due to the increase of the effective refractive index surrounding the NPs. In the case of the 6 nm mass thickness structure, the LSPR position red-shifts 90 nm, resulting in λ_{LSPR} = 660 nm.

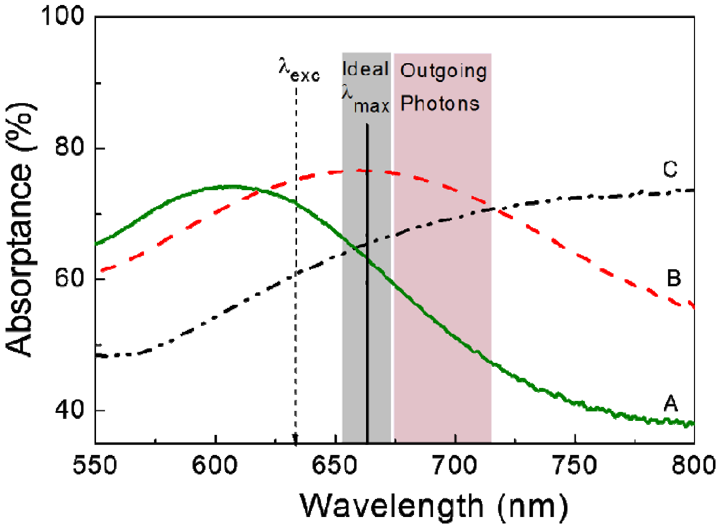

Figure 4.7 Absorptance spectra of SERS substrates with 4 nm (A), 6 nm (B), and 8 nm (C) mass thickness of Ag after deposition of R 6G, showing the ideal wavelength (λ_{max}) for maximum SERS intensity with an excitation wavelength λ_{exc}.

Recent works have investigated the SERS EF as a function of both the LSPR spectral location and the input laser wavelength [218–220]. The condition for maximum Raman enhancement occurs when the LSPR wavelength is located at the midpoint between the laser excitation wavelength (λ_{exc}) and the chosen Raman-scattered photon wavelength, enhancing both the incident and Raman-scattered fields. For an excitation light with wavelength of λ_{exc} = 633 nm, the outgoing Raman-scattered photons, associated with stretches in the 1000-1800 cm^{-1} frequency region, have wavelengths in the 675-714 nm range (marked in Figure 4.7). Therefore, the maximum SERS enhancement is predicted for LSPRs located within the 654-674 nm range (also marked in Figure 4.7), which matches precisely the LSPR peak of the optimal NPs structures with 6 nm of Ag mass thickness.

4.1.5.2 SERS device characterization

SERS spectra of RG6 on cardboard substrates are reported in Figures 4.8. Figure 4.8 (a) clearly shows that the intensity of the Raman signal is pronouncedly amplified when the mass thickness increases from 2 to 6 nm, while it reduces as the mass thickness increases from 6 to 12 nm.

We also provide an estimation of SERS enhancement achieved by each substrate at the same laser excitation source by calculating the enhancement factor. Average EF values and relative standard deviation as a function of the Ag mass thicknesses are reported in Figure 4.8 (b). Each point in Figure 4.8 (b) represents the average value from five individual spectra measured at distinct locations on the samples. The error bars show standard deviations of about 5 % for each set of five measurements. EF data show that an average enhancement as high as 1×10^6 is achieved for the nanoplasmonic cardboard SERS substrate obtained from 6 nm Ag mass thickness. This is attributed to both the optimal spectral matching of the plasmonic resonance (λ_{LSPR} = 660 nm), as depicted in Figure 4.7, and to the high local electric field enhancement produced the 60 nm-sized Ag NPs as predicted by Mie theory analysis (Figure 4.6). According to the maximum scattered electric field curve in Figure 4.6, individual Ag NPs sustaining LSPRs can produce scattered electric field intensities with two orders of magnitude higher than the incident intensity, close to their external surface. Therefore, such particles would be able to generate SERS enhancements up to ~104 when the LSPR is matched with the frequencies of both the incident and Raman-scattered photons. However, the localized near-field enhancement produced by the NP structures fabricated in this work can be considerably higher due to the their elongated character and to the overlap of the near-field regions between adjacent particles, creating the so-called “hot-spots”; thereby yielding EF values one or two orders of magnitude higher than those that could be attained with single Mie nanospheres. As such, these results support that the observed SERS mechanism involves the plasmonic enhancement of both the incident and Raman-scattered photon intensities, particularly with the best-performing 6 nm Ag mass thickness structure.

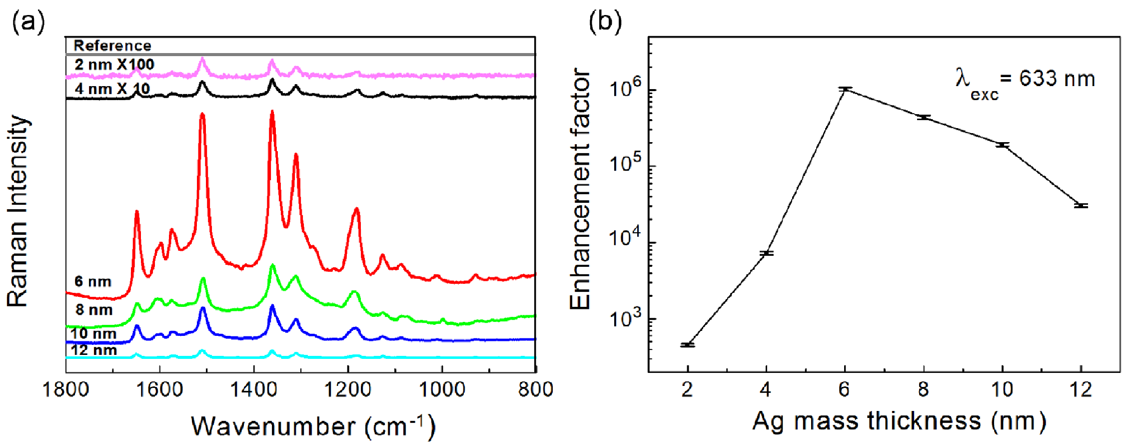

Figure 4.8 (a) SERS spectra of the cardboard packaging substrates coated with and without (Reference) NPs, in the presence of R6G (trace labels). (b) Enhancement factor (EF) as a function of mass thickness.

4.1.5.3 Uniformity and stability of the cardboard substrate

Apart from the highly-sensitive detection, the uniformity and stability of the SERS substrate is crucial for its use as a routine analytical tool. To test the ability to give reproducible SERS signals we collected additional SERS spectra of R6G molecules, using the best-performing 6 nm Ag mass thickness, from 6 randomly-selected spots on the same substrate (2.5 x 2.5 cm² area) separated by a distance of at least 1 cm. Each curve in Figure 4.9 (a) represents the average from five individual spectra measured at the vicinity of each spot. The areas below the characteristic peak at 1360cm^{-1} lie within ~5% variation range, as shown in Figure 4.9 (b). The Raman spectra profiles are almost identical, indicating a good uniformity. Besides, SERS measurements were performed on different substrates, produced in separate batches using the same best-performing conditions, yielding quite similar results; which proves the reproducibility of the method.

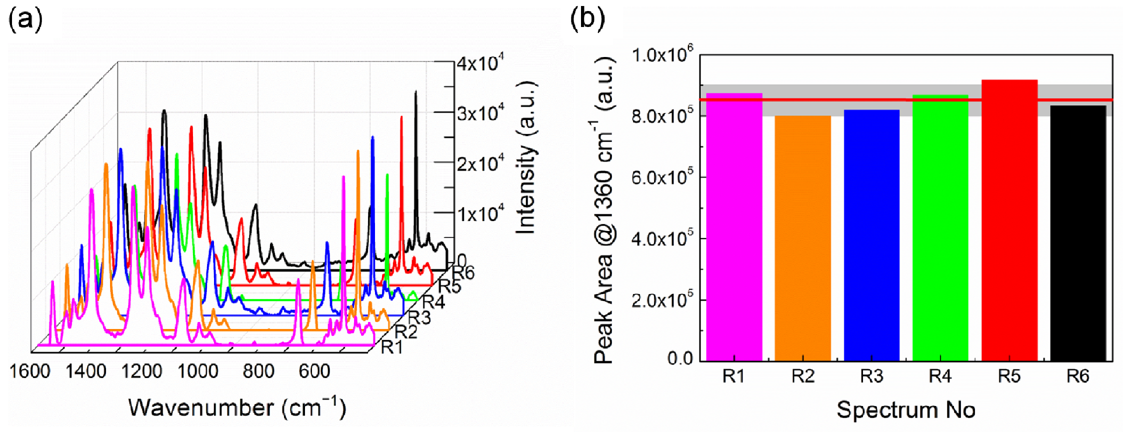

Figure 4.9 (a) SERS spectra of 10^{-6} M R 6G acquired from the best-performing 6 nm Ag mass thickness substrate, at 6 randomly selected spots. Each curve represents the average

from five individual spectra measured at the vicinity of each spot. (b) Values of the integral of the 1360 cm^{-1} peaks in the 6 spectra of (a). The red line indicates the average of the 6 spectra and the gray region represents a 5% variation interval.

The stability of the SERS cardboard substrates has been tested by comparing the Raman signals produced by freshly prepared samples with those measured after six months of storage. The SERS spectra of 10^{-6} M R6G aqueous solutions were posteriorly reanalyzed (Figure 4.10), showing that the Raman peaks profile is similar to that of the newly prepared sample, suggesting a rather stable SERS substrate.

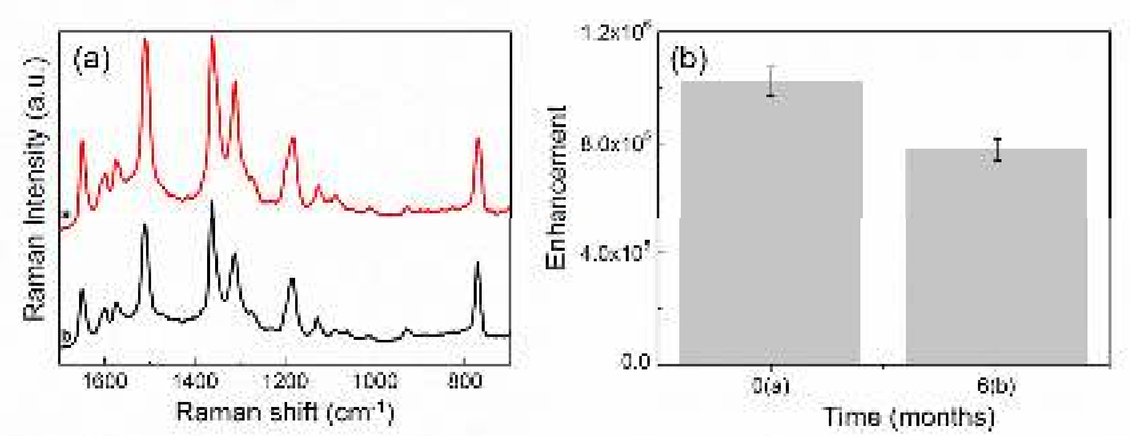

Figure 4.10 a) SERS spectra of 10^{-6} M R6G acquired from arrays stored over a six months under ambient conditions. Each data point represents the average value from five SERS spectra, b) Enhancement Factor (EF) and error bars showing the standard deviations.

4.1.6 Conclusions

In summary, it has been demonstrated the implementation of cardboard packaging for highly efficient SERS substrates. The efficiency of the nanoplasmonic cardboard-based SERS substrates has been assessed through Raman measurements, in which R6G was employed, and under the optimal fabrication conditions, an enhancement factor of $\sim 10^6$ was achieved. Electromagnetic simulations performed with Mie theory indicate that the desirable particle sizes for molecular SERS detection should be ~60 nm. The optimal spectral matching of the plasmonic resonance for maximum Raman enhancement, together with the high local electric field enhancement produced by the 60 nm-sized Ag NPs, enabled the achievement of a remarkable maximum SERS enhancement factor. Furthermore, high reproducibility and stability were also demonstrated. Thus, the large tunability of surface plasmon resonance combined with the advantage of high stability and reproducible EF demonstrate that these cost-efficient Ag nanoplasmonic substrates, fabricated by a low temperature methodology are effectively a large area substrate for SERS.

4.2 3D ZnO/Ag surfaces for disposable and flexible SERS substrates

4.2.1 Introduction

In the last decade several efforts have been made to develop inexpensive opto-electronic devices with unique properties, such as flexibility, portability and/or disposability. Several studies focused their research on paper-based platforms in electronic applications, in order to develop their innovative use as bendable supports, with reliability similar (or even potentially superior) to that of conventional rigid substrates. These paper-based devices are already being used in distinct applications, such as electronic displays [221], thin film transistors [222] and solar cells [101], paper batteries [223], UV sensors [224], biomedical applications [225], platforms for SERS detection [92,117,156], among others.

A tremendous amount of work on the fabrication of various cost efficient cellulose substrates for SERS has already been performed by various research groups [92,153,154,208,226]. This type of substrates can have Raman signal enhancements (EF= 10^5 - 10^7) comparable with the conventional rigid and planar supports such as glass and silicon wafers. Nevertheless, paper substrates for SERS have several advantages over conventional rigid substrates in terms of cost, flexibility, portability, eco-friendliness and biodegradability. For instance, such substrates are able to collect analytes when used in contact with the human body or food in packaging [136,137], as they can be wrapped around curved surfaces, opening doors for the next generation of bio-medical optical sensing. Despite its known technological applications, there are still few contributions investigating 3D ZnO nanostructures on paper [227–231], and even less addressing the direct growth of aligned ZnO NRs on such substrates [232].

Recently, NPs made of noble metals, such as Ag or Au, have been proposed as promising SERS substrates when deposited on nanostructures (Ag@ZnO [233], Ag@SiO_2 [234] and Ag@TiO_2 [182]), with different morphologies, such as nanorods, nanotubes and nanowires. This is due to the contributions of three main effects: 1) local electromagnetic field enhancement provided by noble MNPs sustaining SPRs, 2) increase of the surface area provided by the semiconductor nanostructures, and 3) semiconductor-supported electromagnetic enhancement caused by the charge transfer between the noble metal and the adjacent semiconductor [125,182,235–237].

Among the materials used for the 3D nanostructures, ZnO has received much attention. The possibility of engineer many different ZnO morphologies, employing a variety of growth methods, makes this material a promising candidate for potential applications such as piezoelectric nanodevices [230,231], UV sensors [238], photocatalysis [239] and SERS devices [233,240]. Among the various morphologies, ZnO NRs are particularly interesting mainly due to their high surface-to-volume ratio, making them an ideal nanostructured support for the development of SERS substrates [125,241].

To the best of our knowledge, this is the first report demonstrating the direct growth of Ag NPs@ZnO NRs on paper substrates for low-cost and flexible SERS devices. Here, a simple and scalable two-step method is presented: First, ZnO NRs are grown on paper using a low temperature (90° C) and very fast (5-15 min) hydrothermal method assisted by microwave radiation. The fabrication of ZnO NRs using hydrothermal methods has thus far been described as requiring much higher synthesis times [227,229,230,232]. Secondly, the NRs are decorated with Ag NPs formed by thermal evaporation assisted by electron beam, which results in the direct arrangement of a dense array of individual NPs with good control of their size and shape, without requiring post-deposition thermal processes [92]. These can be strategically exploited to fabricate flexible, disposable, low cost, highly sensitive SERS substrates.

4.2.2 Direct growth of plasmonic nanorod forests on paper substrate for low-cost flexible 3D SERS platforms

This work reports a paper substrate, coated with ZnO NRs decorated with Ag NPs, for the production of inexpensive, highly-performing and reproducible three-dimensional (3D) SERS platforms. The ZnO NRs were synthesized by a simple, fast and low-temperature hydrothermal method assisted by microwave radiation and made SERS-active by decorating them with a dense array of Ag NPs deposited via a single-step thermal evaporation technique. Using R6G as probe molecule, with an amount down to 10^{-9} M, the SERS substrates allowed a Raman signal enhancement of 10^{7}. The contribution of the inter-Ag-NPs gaps for 3D geometry, ZnO NRs orientation and the large sensing area allowed by the NR scaffolds, were determinant factors for the significant Raman enhancement observed. The results demonstrate that plasmonic nanorod forests, covered with Ag NPs, are efficient SERS substrates with the advantages of being recyclable, flexible, lightweight, portable, biocompatible and extremely low-cost.

4.2.2.1 Sample preparation

The raw paper substrates used in this study are made from the “Felix Schoeller Group” and consist of pressed cellulose fibers with several micrometers of diameter, without any coating. The paper (cut with an area of 2.5×2.5 cm^{2}) weights 63 g/m² and has 135-136 mm thickness. Figure 4.11 shows the fabrication procedure of Ag-coated zinc oxide nanorods. In the first step, 100 nm-thick ZnO seed layer was deposited on the paper substrate by sputtering. A ceramic oxide target with a purity of 99.99% was used for the deposition. The oxide deposition conditions were: power density P = 8.2 Wcm^{-2}, distance between the target and substrate, d = 15 cm; deposition pressure, p = 4×10^{-3} mbar. Next, the ZnO nanorod arrays were synthesized by the hydrothermal method assisted by microwave radiation. The ZnO NRs were grown with an aqueous solution of 25 mM zinc nitrate hexahydrate ($Zn(NO_3)2\cdot6H_2O$; 98%, CAS: 10196-18-6) and 25 mM hexamethylenetetramine ($(C_6H_{12}N_4)2$; 99%, CAS: 100-97-0), both from Sigma Aldrich. Additional information about this procedure can be found elsewhere [238]. Considering energy consumption, the hydrothermal synthesis via microwave heating of ZnO NRs is preferential to other techniques, since it has proven to be a low temperature and low cost process [229,239].

The ZnO seeded substrates (25 x 25 mm) were placed at an angle against the vessel, with the seed layer facing down and filled with an aqueous solution of zinc nitrate hexahydrate and hexamethylenetetramine. The ZnO NRs synthesis was carried out with a microwave power input of 50 W and a constant temperature of 90 °C, for 15 minutes. After each synthesis process, the materials were cleaned with deionized water and dried with compressed air.

Finally, the Ag NPs were formed by the deposition of a 8 nm layer of Ag by one step thermal evaporation at 150 °C. With this fast and simple strategy, it is possible to fabricate homogeneous silver-coated zinc oxide nanorod (Ag NPs@ZnO NRs) arrays on the entire paper substrate.

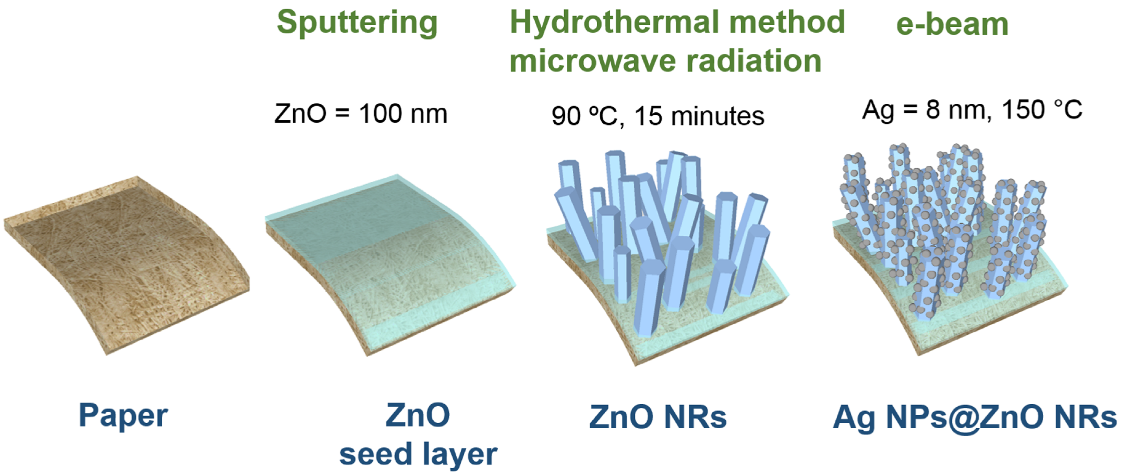

Figure 4.11 Schematic drawing of the fabrication of SERS platforms on paper, composed of ZnO NRs covered with Ag NPs. In the first step, crystalline ZnO seeds are deposited by sputtering on paper, followed by the growth of ZnO NRs via a hydrothermal technique. Secondly, Ag NPs are spontaneously formed throughout the rods upon thermal evaporation of a thin Ag layer.

4.2.2.2 Paper characterization

Prior to the nanostructures fabrication, a complete characterization of the substrate morphology is crucial, as it will influence the final geometry and density of the ZnO NRs arrays, which will also affect the subsequent Ag NPs decoration. K. Ogata *et al.* [229] made preliminary attempts to form Ag NPs@ZnO NRs on paper by using a surface coating with either ZnMgO or Au layers. The authors observed that, due to the rough surface structures of cellulose, the growth of ZnO NRs was not uniform, on both ZnMgO/paper and Au/paper substrates. It became initially believed that the growth of highly pure, crystalline and aligned nanorods demanded extreme temperature treatments and smooth, specifically-oriented substrates [232]. In fact, the thermal vulnerary, extreme surface roughness and certain contaminants of cellulose paper present important challenges to allow its role as platform for precisely-engineered nanostructures formation.

SEM-EDS analysis of the raw paper substrate (Figure 4.12 a–b) revealed a high-density structure of intertwined cellulose fibers with a cylindrical and flat shape with several micrometers of diameter, and also the absence of calcium carbonate ($CaCO_3$), as confirmed by XRD and EDS measurements. Figure 4.12 (c) shows XRD patterns of the raw substrate. From the data it is possible to qualitatively evaluate that all paper substrates present the same diffraction features, which is corroborated by the characteristic peaks at 2θ= 14.7° and 22.7°, corresponding to the 110 and 200 crystallographic planes of monolithic cellulose, in accordance with the literature[242]. Figure 4.12 (d) shows that the raw paper has a rough surface with a root mean square (RMS) value of almost 5 µm.

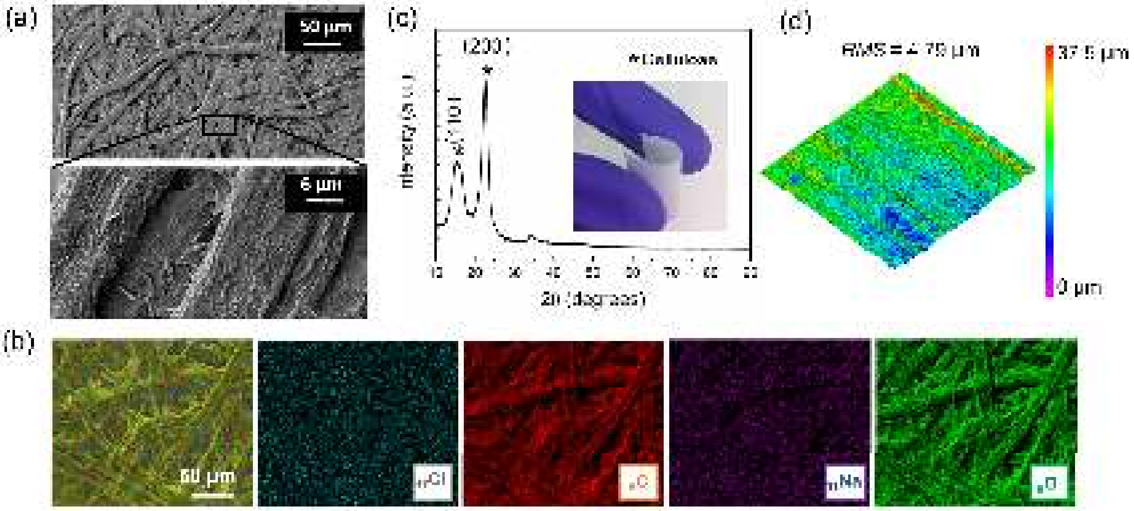

Figure 4.12 Raw paper characterization. (a) SEM images at a low and high magnifications, showing its fibrous morphology; (b) SEM images (artificial colored) together with the

corresponding X-ray maps of Cl, C, Na and O species; (c) XRD diffractogram. The inset is the image of the paper used as substrate; (d) 3D profilometer on a 1×1 µm area.

Differential scanning calorimetry was then used to determine the substrate material stability during the nanostructures formation process. Figure 4.13 depicts the temperature-dependent mass change (TG) and temperature-dependent heat flux (DSC) results for raw paper substrate. The DSC curve presents a tiny endothermic peak at 93 °C, accompanied by a small weight loss (about 3.8 %) which corresponds to desorption or water evaporation from the cellulose fibers. Above this temperature, the paper shows no further mass variation up to ~280 °C. At 328 °C two exothermic peaks are observed, accompanied by two decomposition steps that corresponded to a weight loss of about 85.25 %. These peaks and weight loss can be correlated with the decomposition of cellulose fibers. By analyzing the obtained results, it is possible to ensure that the substrate can be heated up to 280 °C without damage and without losing its properties. Above this temperature the mass of the sample starts to decrease, indicating that it is the maximum processing temperature that this type of substrate can withstand.

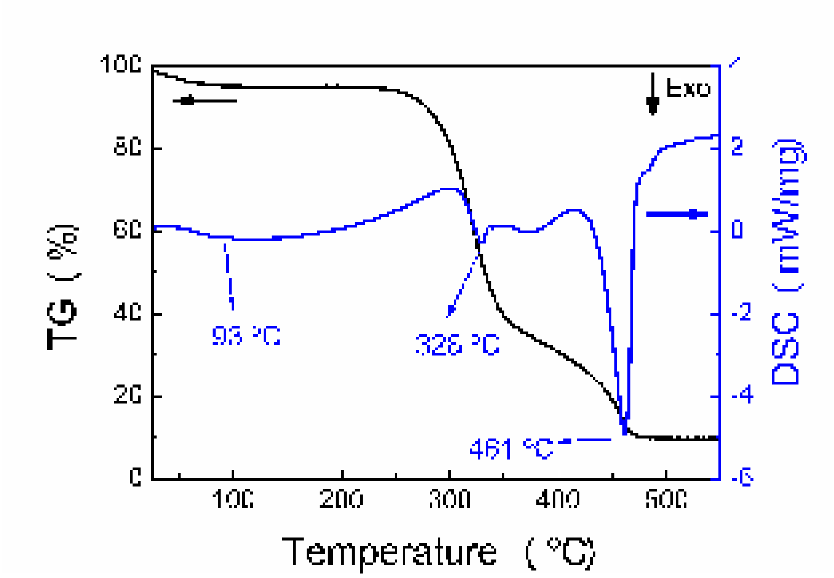

Figure 4.13 Temperature-dependent mass change, TG (%) (black line), and heat flux (DSC) signal of the paper substrate between room temperature and 550 °C (blue line).

4.2.2.3 ZnO nanorods growth on paper and glass substrate

The representative surface and cross-sectional SEM images of the ZnO NRs formed on paper substrate are presented in Figure 4.14. The low magnification images indicate that quasi-aligned[3] hexagonal-shaped nanorods are uniformly grown in high density on the entire substrate surface. The typical widths and lengths of the obtained nanorods

---

[3] vertically oriented with small tilt angles with respect to the normal-to-substrate direction

are in the range of 50–100 nm and 200-300 nm, respectively. The XRD diffractogram of the paper substrate with ZnO NRs is presented in Figure 4.14 (e) and 4.14 (f), showing two intense peaks at 15 and 22 degrees that are characteristic peaks of amorphous and crystalline cellulose fibers, respectively [243]. By magnifying the diffractogram [Figure 4.14 (f)], it is possible to observe three peaks between 30 and 40 degrees all corresponding to the crystallographic planes of ZnO. The synthesized material can be fully assigned to the hexagonal wurtzite ZnO crystalline structure, with lattice constants of a=0.3296 nm and c=0.52065, in accordance to the reported data [244]. No other crystalline phases were detected.

Despite the intrinsically rough nature of the paper surface, NRs could be uniformly grown on the entire substrate surface, without damaging the cellulose fibers during their chemical synthesis process.

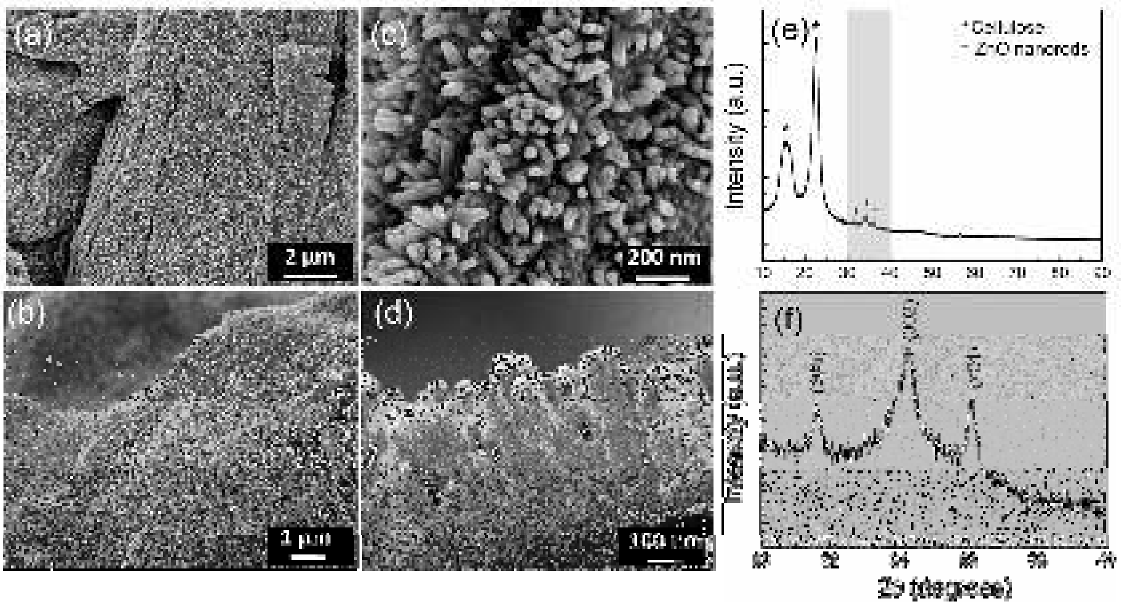

Figure 4.14 Surface (a,c) and cross-section (b,d) SEM images of the ZnO nanorods directly grown on paper substrate. XRD pattern (e) of the sample and amplification (f) of the pattern in the 30-40 degrees range.

One important aspect that has been overlooked in the literature so far, is the role of the substrate on which ZnO NRs are synthetized. The representative cross-sectional and surface SEM images of the ZnO NRs formed on the glass substrate using the same seed layer conditions are presented in Figure 4.15. On glass substrate, dense and aligned ZnO NRs with widths around 40–50 nm and lengths of 400-500 nm were obtained. It should be noted that the average widths of the NRs on paper substrate have a higher value (~100 nm) than on bare glass substrates (~ 50 nm). It is well known that the particle size of the seed layer is a critical parameter in determining the diameter of ZnO NRs [245]. This is consistent with XRD results, shown in the inset of Figure 4.15, in which the grain size of the ZnO seed layer is higher for paper substrate (D = 18.11 nm).

Grain sizes of ZnO thin films on paper and glass substrates were calculated from Scherre's equation [232] :

$$D = 0.94 \times \lambda \times \beta \times \cos\theta \qquad (4.1)$$

where, λ is the wavelength of the X-ray radiation; θ is the Bragg's angle; and β is the full width at half maximum.

On the other hand, the average length of the NRs increased from 300 nm to 500 nm when the substrate is glass. The same tendency was observed for the variation of the seed layer morphology as a function of the annealing temperature [238,246]. The growth rate of the ZnO NRs on the sputtered ZnO seed layer increased because of the improved crystallinity of the seed layer. From the inset of Figure 4.15, the peak intensity of the (002) plane is found to increase for the glass substrate, indicating that the degree of crystal orientation increases.

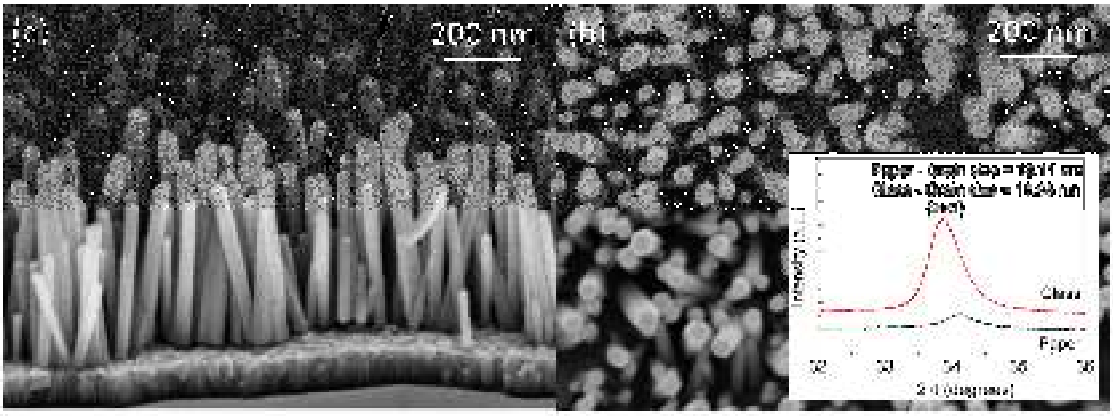

Figure 4.15 Cross-section (a) and (b) surface SEM images of the ZnO nanorods grown on glass substrate. Inset: XRD pattern and the respectively crystallite sizes of ZnO thin films (seed layers) on glass and paper substrate, obtained with Scherrer's equation.

4.2.2.4 Decoration of Ag Nanoparticles on ZnO Nanorods paper substrate

To provide SERS activity, the NRs were coated with Ag NPs deposited by thermal evaporation (Ag NPs@ZnO NRs). Two control samples were also prepared: one with only Ag NPs (without NRs) deposited on paper in the same run, and a second control sample with only ZnO NRs on paper but without NPs. The absorptance spectra of these samples are shown in Figure 4.16. The absorption edge at ~360 nm present in the sample without Ag NPs corresponds to the bulk value (3.37 eV) of the ZnO bandgap [247,248]. Such a sharp edge is not evident in the Ag NPs@ZnO NRs sample because the NRs surface is fully covered with Ag NPs, allowing little light exposure to the ZnO material, as it can be observed in the corresponding SEM inset image of Figure 4.16. The spectra of the Ag NPs and Ag NPs@ZnO NRs paper substrates show two main peaks: (1) a broad smooth peak in the visible region (LSPR, indicated in Figure 4.16), corresponding to the dipolar SPRs of the Ag NPs, which is the main mode responsible for SERS; and (2) a relatively narrower peak in the UV (at around 400 nm) which can be ascribed to higher order modes caused either within the particles (i.e. quadrupole SPRs) or by interaction with their vicinity media (i.e. short-range interparticle coupling and particle-substrate/NRs interactions) [92,119,249]. The inset in Figure 4.16 shows typical SEM images of ZnO NRs before and after Ag NPs deposition. As previously reported [92] and confirmed by the surface morphology observed by SEM (see inset of Figure 4.16), Ag NPs arrays formed from 8 nm Ag mass thickness are composed of semi-spherical particles with in-plane base diameters in the 50–80 nm range but shorter heights (about half the diameter) with an average separation of less than 10 nm between adjacent Ag NPs. On 3D ZnO NRs, close-packed Ag NPs are distributed uniformly on the top and sidewalls of the hexagonal ZnO NRs, leading to a large surface–volume ratio of the nanostructure. The size of these Ag NPs is about 30-40 nm in diameter, with an average separation of less than 5 nm between adjacent Ag NPs, which is critical to create high SERS activity excited by the surface plasmon coupling between the narrow gaps of the neighboring Ag NPs growing on the NRs [94,95]. Comparing with the paper substrate without ZnO NRs, the average size and separation of the NPs decreases by half its value. The decrease of the NPs sizes on ZnO NRs can be attributed to the higher surface area that is covered during Ag deposition, resulting in a lower Ag thickness.

When unpolarized light impinges from the top, onto Ag NPs deposited on paper, the incident electric field vector mainly excites in-plane SPR modes along the long axes (i.e. the equator) of the particles. However, when the NPs are located on vertically oriented NRs, the light impinges on the NPs side surface and its electric field will excite SPRs along the short-axis (i.e. the height) of the semi-spherical particles. The frequencies of the short-axis SPRs are blue-shifted from the long-axis resonances [249] which explains the observed blue-shift from the plasmons bands of the Ag NPs@ZnO NRs relative to the Ag NPs on paper (λ = 692 nm to λ = 600 nm) in Figure 4.16. This is an important aspect regarding the interpretation of the optical effects of MNPs-decorated NRs, which has so far received little attention in the literature. In addition to that, it is well know that a decrease in the average particle size results in a blue shift of the SPR [171,174].

The UV-Vis-NIR spectra of Figure 4.16 provides information on the averaged far-fields scattered from the NPs ensemble, but not on the near-fields localized in the

NPs vicinity which are responsible for the "hot-spots" that amplify the Raman signals in SERS [249]. Nevertheless, the analysis of such spectra is important to determine the spectral location and extension of the SPRs and, thereby, enable the matching with the wavelengths of the incident laser and Raman photons scattered from the analyte, as explained below.

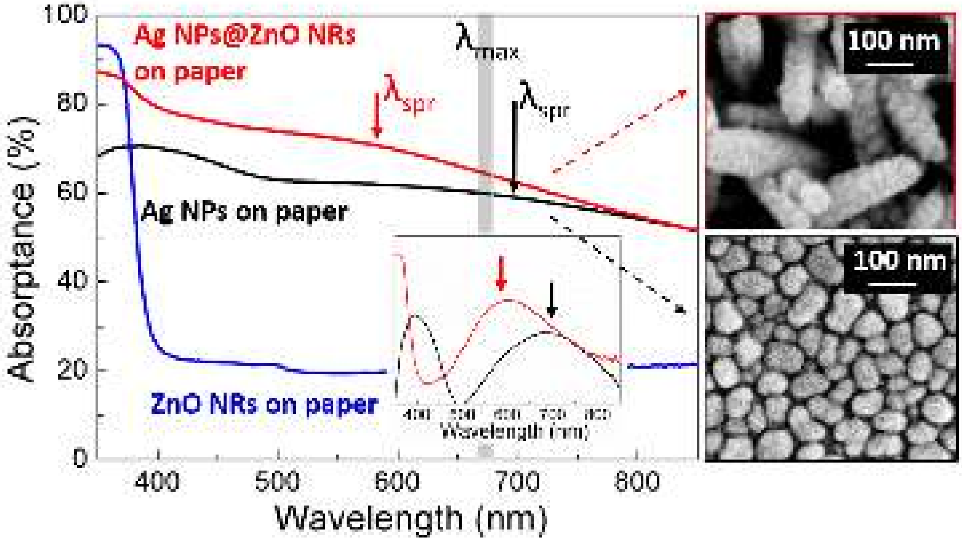

Figure 4.16 UV-Vis-NIR spectra of ZnO NRs (blue line), AgNPs (black line) and Ag NPs@ZnO NRs (red) on paper substrates. The vertical solid line indicates the ideal wavelength (λ_{max}) for maximum SERS intensity with excitation wavelength λ_{exc}=633 nm. *Inset:* Detail of the SPR peaks with subtracted linear baseline and SEM images of the paper substrate and the arrays of ZnO nanorods after Ag NP decoration.

4.2.2.5 Implementation of plasmonic paper substrate as SERS device

The SERS activity of different Ag NPs decorated samples was evaluated using 10^{-6} M solution of R6G as a Raman reporter and let to dry at room temperature corresponding to 9.58 x 10^{-1} nanograms. As shown in Figure 4.17 (a), R6G on the Ag NPs paper substrate displays one order of magnitude lower signal when compared to its signal in the substrate containing Ag NPs@ZnO NRs.

For a more precise determination of the EF, the calculations of both the I_{SERS} and I_{Raman} intensities consider the area under the Raman peaks at 1360 and 1509 cm^{-1}, as shown in Figure 4.17 (b). The average EF obtained with the Ag NPs substrate (without NRs) was 1.6×10^5, while with the Ag NPs@ZnO substrate an average enhancement as high as 1×10^6 was achieved.

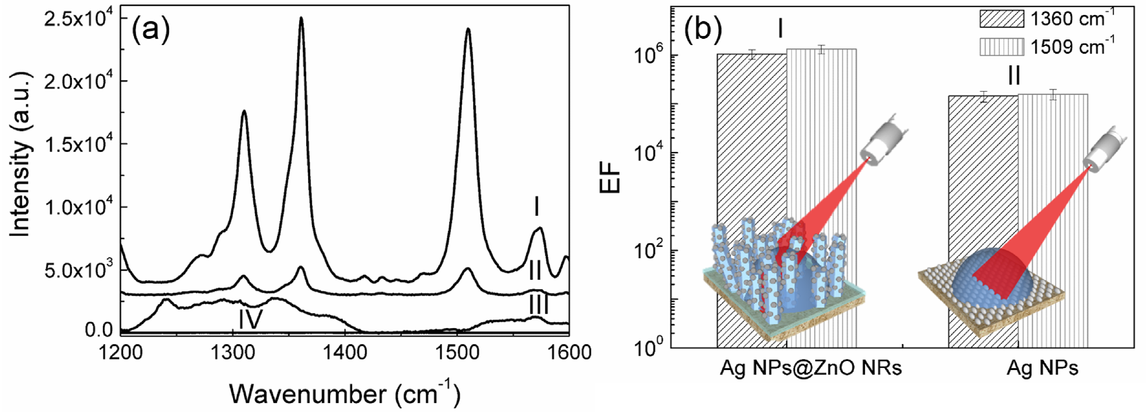

Figure 4.17 Raman spectra of 10^{-6} M of R6G dried (corresponding to 9.58 x 10^{-1} nanograms) on the SERS paper substrate decorated with Ag NPs@ZnO NRs (I) and Ag NPs (II). These are compared with the respective backgrounds without analyte, (III) Ag NPs@ZnO NRs and (IV) Ag NPs. (b) SERS EF (Enhancement factor) of the strongest Raman vibrational lines (1360 and 1509 cm^{-1}). The inset is the schematic drawing of each SERS active substrate.

Recent works have investigated the SERS EF as a function of both the LSPR spectral location and excitation laser wavelength [92,220]. It has been found that the condition for maximum Raman enhancement occurs when the LSPR wavelength is located at the midpoint between the laser excitation wavelength (λ_{exc}) and the chosen Raman-scattered photon wavelength, which enhances both the incident and Raman-scattered fields. For an excitation light with a wavelength of λ_{exc} = 633 nm, the outgoing Raman-scattered photons, associated with stretches in the 1200–1600 cm^{-1} frequency region, have wavelengths in the 685–704 nm range. Therefore, the maximum SERS enhancement is predicted for LSPRs located within the 659–668 nm range [92] (labeled in figure 4.16), which is very close to the LSPR peak of the Ag NPs structures on paper. The LSPR of the Ag NP@ZnO NRs is slightly blue shifted from this optimum band, due to the excitation of LSPRs along the short axis and the decrease of the NPs sizes. Therefore, higher SERS enhancement can be anticipated with structures composed by larger and/or more spherical NPs, which red-shifts the plasmonic resonances. However, it is important to note that further increasing the Ag precursor layer to allow bigger NPs can be detrimental to SERS, as it leads to NPs aggregation and film formation.

The observed high SERS enhancement can be ascribed to the decrease of the MNPs separation and to the increase of the sensing area provided by the 3D NR supports. Theoretical calculations and experiments have shown that, when the interparticle separation decreases to less than 10 nm, the electromagnetic coupling between neighboring Ag NPs creates extremely high SERS activity due to the generation of “hot-spots” with strong electric-field intensity [93,250,251]. Comparing the substrate without and with ZnO 3D structures, the gaps between adjacent Ag-NPs decrease from 10 to 5 nm, respectively, as shown in Figure 4.16. Consequently, this should contribute to the SERS activity shown in Figure 4.17 (b). However, the main cause for the enhancement is the large available surface area provided by the dense NRs forest, which leads to a large surface-to-volume ratio for Ag NP deposition, thus providing an extended area to form plasmonic “hot-spots” and for the deposition of analyte molecules [233,234,252]. In addition, a third possibility is the natural inclination of the ZnO NRs on paper substrate. The maximum and minimum SERS intensities observed for MNPs are for the polarization directions perpendicular and parallel to the long axis of the NPs, respectively [87,253–255]. In the case of the tilted NRs arrays, the incident polarized electric field is not completely parallel to the NPs, and thus the electromagnetic enhancement should be higher than for example, that for the vertically aligned NRs, which also contributes to an improved SERS detection.

Previous investigations of SERS on semiconductor NR supports claim that there can be a chemical enhancement effect resulting from the interaction between the ZnO and the metallic particles materials [11–14]. To study such possible chemical effect of the ZnO NRs, we compared the Raman activities of two substrates: an Ag film grown on a ZnO layer (Ag/ZnO_{layer}/paper) and an Ag film grown on paper substrate (Ag/paper). The deposition conditions of the ZnO_{layer} and Ag films are the same as those described in the experimental section. The SERS activity of these test samples was measured using 10^{-6} M solution of R6G as a Raman analyte and let to dried as it is shown in Figure 4.18. The Raman intensity of the R6G bands at 1360 cm^{-1} and 1509 cm^{-1} collected with the ZnO_{layer}/Ag substrate is lower than that collected with the bare Ag substrate, demonstrating that the supporting ZnO_{layer} material in the hybrid structure should not present any chemical enhancement effect on the SERS activity.

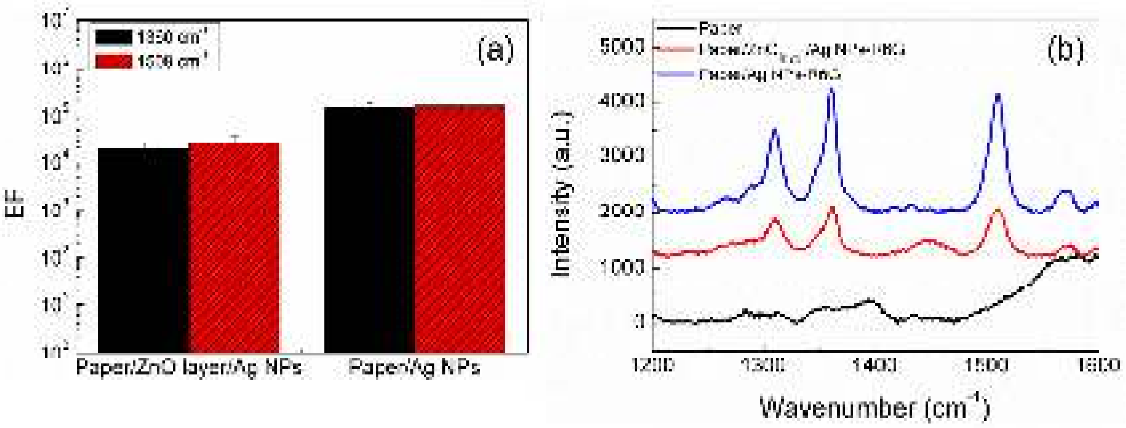

Figure 4.18 (a) Raman spectra of 10-6 M (i.e. 9.58 x10^{-1} nanograms) of R6G on paper substrate with ZnOlayer/Ag NPs and Ag NPs. These are compared with the respective background paper substrate without analyte. (b) SERS EF (Enhancement factor) of the strongest Raman vibrational lines (1360 and 1509 cm^{-1}).

Figure 4.19 (a) shows the SERS spectrum with different amounts (10^{-6}, 10^{-7}, 10^{-8} and 10^{-9} M) of R6G deposited on the Ag NPs@ ZnO NRs paper substrate and let to dried at room temperature (corresponding to 9.58 x 10^{-1}, 9.58 x 10^{-2}, 9.58 x 10^{-3}, 9.58 x 10^{-4} nanograms of R6G, respectively). Figure 4.19 (b) presents a correlation between SERS lines areas of the 1360 and 1509 cm^{-1} vibration lines, and the amount of R6G present. It is noteworthy that the Raman signal can still be observed at an amount as low as 10^{-9} M, i.e. we are able to sense a number of molecules as low as N_{SERS}= 1.20 x 10^9 molecules of R6G. The SERS measurements of the Ag NPs@ ZnO NRs sample using 10^{-9} M R6G resulted in the maximum EF value (~1 × 10^7) attained in this work.

The plot in Figure 4.19 represents the mean average value of three measurements for each sample and the error bar for each data point is the SD of the area signal. The area of the SERS line at 1360 cm^{-1} due to C-C stretching vibration is highly sensitive to the concentration of R6G. At low concentrations, the vibrational line area increases linearly with the amount of R6G ($\mathrm{AA}_{1360}\mathrm{cm}^{-1}$ Equation 4.2), where $\mathrm{AA}_{1360}\mathrm{cm}^{-1}$ corresponds to the analytical area from the band at 1360 cm^{-1}, and M_{R6G} to the R6G amount. The linear correlation was used to determine the limit of detection (LOD), sensitivity (slope of the working curve), and the linearity (r^2=0.993) from the LOD up to 9.58 x 10^{-1} nanograms:

$$\mathrm{AA}_{1360\ \mathrm{cm}^{-1}} = (131 \pm 6) \times 10^4\, \mathrm{M}_{\mathrm{R6G}} - (2 \pm 3) \times 10^4 \qquad (4.2)$$

The limit of detection (LOD) was about $8.9 \pm 0.9{\times}10^{-9}$ nanograms of R6G distributed along the drop area after dried, which was estimated by the following expression: $LOD = \frac{3\sigma}{\mathrm{M}_{\mathrm{R6G}}}$, where σ is the standard deviation of the background signal. The background signal refers to the SERS area from a sample with R6G concentration equal to zero, and helps to set the limit for separation of a positive detection from a negative detection. The limit of quantification (LOQ) is defined by: $LOQ = \frac{\mu + 10\sigma}{\mathrm{M}_{\mathrm{R6G}}}$, where μ is the average of background signal. Therefore, LOQ could be determined as $1.3 \pm 0.1 \times 10^{-7}$ nanograms of R6G.

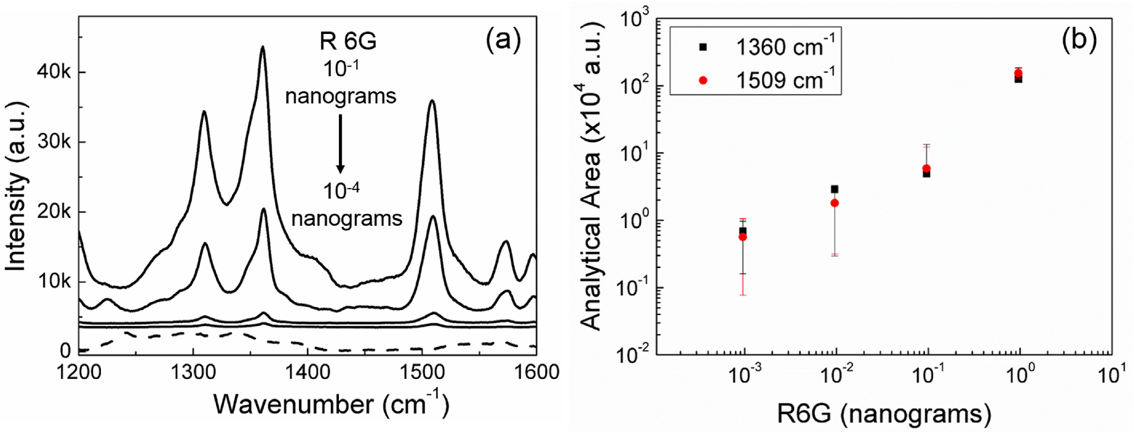

Figure 4.19 (a) Raman spectra at four different amounts (10^{-6}, 10^{-7}, 10^{-8} and 10^{-9} M corresponding to 9.58 x 10^{-1}, 9.58 x 10^{-2}, 9.58 x 10^{-3}, 9.58 x 10^{-4} nanograms of R6G, respectively) of R6G. The spectrum of Ag NPs@ ZnO NRs is plotted (dash line) as background. (b) Values of the Raman area of the 1360 and 1509 cm^{-1} vibrational lines for the different amounts of R6G added to the SERS substrate.

It is thus demonstrated that the SERS performances of the Ag NPs@ZnO NRs paper-based substrates developed here are comparable to those exhibited by state-of-the-art substrates, based on conventional rigid materials (Glass, c-Si), containing arrays of Au or Ag-coated nanorods, when employing the same molecular probe [183,234]. Nonetheless, our innovative methodology provides an easy and fast fabrication process to form the Ag NPs@ ZnO NRs, resulting in a good homogeneity of the morphological characteristics of the 3D structures that greatly contribute to the uniformity and stability of the SERs signals.

4.2.2.6 Conclusions

In summary, a simple strategy is presented to fabricate paper-based SERS substrates with highly ordered ZnO nanorods arrays decorated with Ag NPs. Using a microwave heating technique, the nanorods were directly grown on paper substrates at low temperature (90 °C) in a short time (15 min). By optimizing the ZnO and Ag nanostructures, the paper substrate exhibited a maximum EF value of ~10^7 using 10^{-9} M of R6G (2 µL of volume) as probe molecule. This substrate, with a high surface area and a high concentration of Ag NPs, has an ideal structure for the development of a SERS sensing system which is recyclable, flexible, lightweight, portable, biocompatible and economically cheap. These attributes make the present substrate very attractive when compared to conventional rigid substrates.

4.2.3 3D ZnO/Ag SERS on Disposable and Flexible Cardboard Platforms

In the present work, ZnO NRs with a hexagonal structure have been synthesized via a hydrothermal method assisted by microwave radiation, using specialized cardboard materials as substrates. Cardboard-type substrates are cost-efficient and robust paper-based platforms that can be integrated into several opto-electronic applications for medical diagnostics, analysis and/or quality control devices. This class of substrates also enables highly-sensitive Raman molecular detection, amiable to several different operational environments and target surfaces. The structural characterization of the ZnO NR arrays has been carried out XRD, SEM and optical measurements. The effects of the synthesis time (5–30 min) and temperature (70–130 °C) of the ZnO NR arrays decorated Ag NPs have been investigated in view of their application for surface-enhanced Raman scattering molecular detection. The size and density of the ZnO NRs, as well as those of the Ag NPs, are shown to play a central role in the final SERS response. A Raman enhancement factor of 4.6×10^{9} was obtained using rhodamine 6G (10^{-8} M) as the test analyte; a ZnO NR array was produced for only 5 min at 70°C. This condition presents higher ZnO NR and Ag NPs densities, thereby increasing the total number of plasmonic “hot-spots”, their volume coverage and the number of analyte molecules that are subject to enhanced sensing.

4.2.3.1 Sample preparation

Two sets of experimental conditions were tested for a microwave power input of 50 W:
1 – Variation of synthesis time, 5, 10, 20 and 30 minutes, with a constant temperature of 70 ºC, which is the minimum temperature required for the ZnO nanorod formation;
2 – Variation of temperature, 70, 90, 110 and 130 °C, employing the longer 30 minutes synthesis time in order to have a higher width/length ratio of the NRs. After each synthesis process, the materials were cleaned with deionized water and isopropyl alcohol and dried with compressed air.

After the growth of ZnO NRs on the cardboard substrates, Ag NPs were deposited using an electron gun-assisted thermal evaporation technique [172], to be able to use the substrates as platforms for SERS. The temperature during the evaporation process was held at 150 °C and the Ag layer was deposited with a mass-equivalent thickness of 6 nm. Figure 4.20 represents a schematic of the production process of ZnO NRs arrays decorated with Ag NPs on cardboard substrates. To understand the effect of the length and width of the ZnO NRs on the SERS signal, the Ag NPs were deposited onto the different aforementioned rod structures with distinct synthesis times and temperatures.

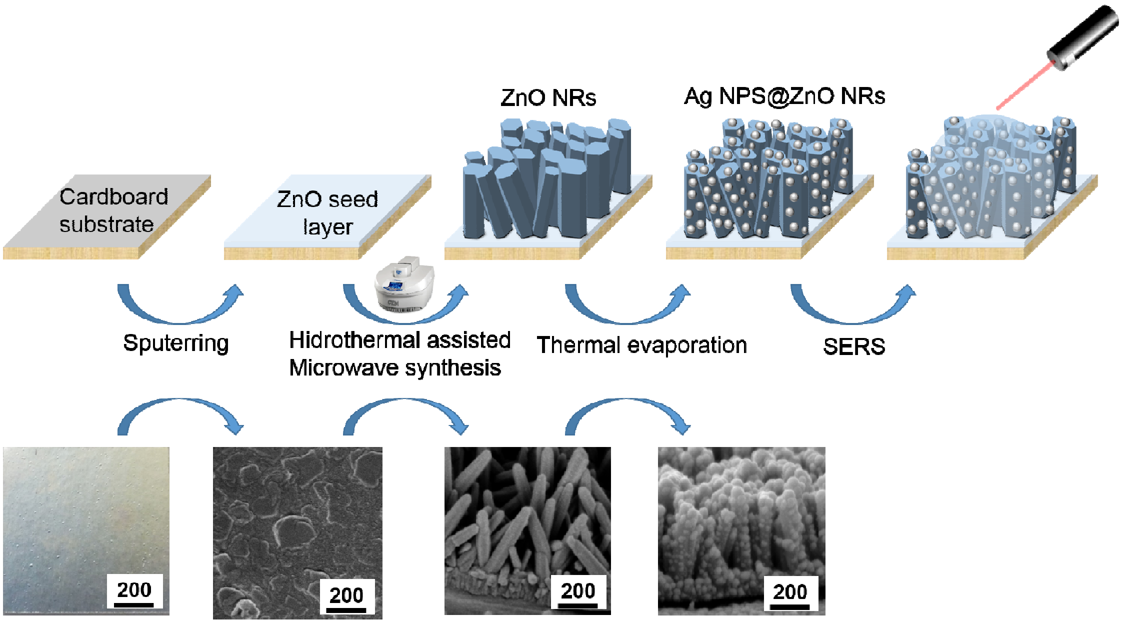

Figure 4.20 Schematic of the production process of ZnO nanorod arrays, by hydrothermal synthesis assisted by microwave radiation, decorated with Ag NPs, on cardboard substrates, for SERS application.

4.2.3.2 ZnO nanorods characterization

To infer the morphology and the crystallographic structure of the synthesized materials, SEM and XRD experiments were carried out on all the produced samples. The synthesis time and temperature are two of the most important parameters in ZnO NRs synthesis that control the resulting morphology.

SEM analysis for samples produced at 70 °C for different periods of time (5, 10, 20 and 30 minutes) are presented in Figure 4.21. It is noteworthy that the NRs shape is hexagonal regardless of the synthesis time. Nevertheless, with the increase of synthesis time, it is possible to observe that the ZnO NRs become wider with a less compact distribution, with widths ranging from 45 (± 5), 50 (± 5), 55 (± 5) to 75 (± 5) nm, for synthesis times of 5, 10, 20 and 30 min, respectively. From the cross-sectional SEM images of Figure 4.21, it is clear that the ZnO NRs growth is “quasi-aligned” vertically from the substrate. The NRs length also increases with longer time, presenting values of approximately 150 (± 5), 175 (± 10), 200 (± 20) and 325 (± 20) nm, for synthesis times of 5, 10, 20 and 30 minutes, respectively. These results are consistent with what is reported in the literature [256]. The size of the ZnO NRs depends on the concentration of [Zn^{2+}] ions in the solution. So, considering the initial solution concentration, the concentration of ions in solution will decrease with the increase of particle size. Therefore, more synthesis time implies prolonged nanorod growth, which occurs with a constant crystal growth rate that allows the formation of NRs with a constant diameter from the bottom to the top, as the ones observed in the cross section images of Figure 4.21. As such, longer synthesis time will add more ions to the ZnO NRs crystallographic structure and make them grow in length and in width, while maintaining the rods' alignment.

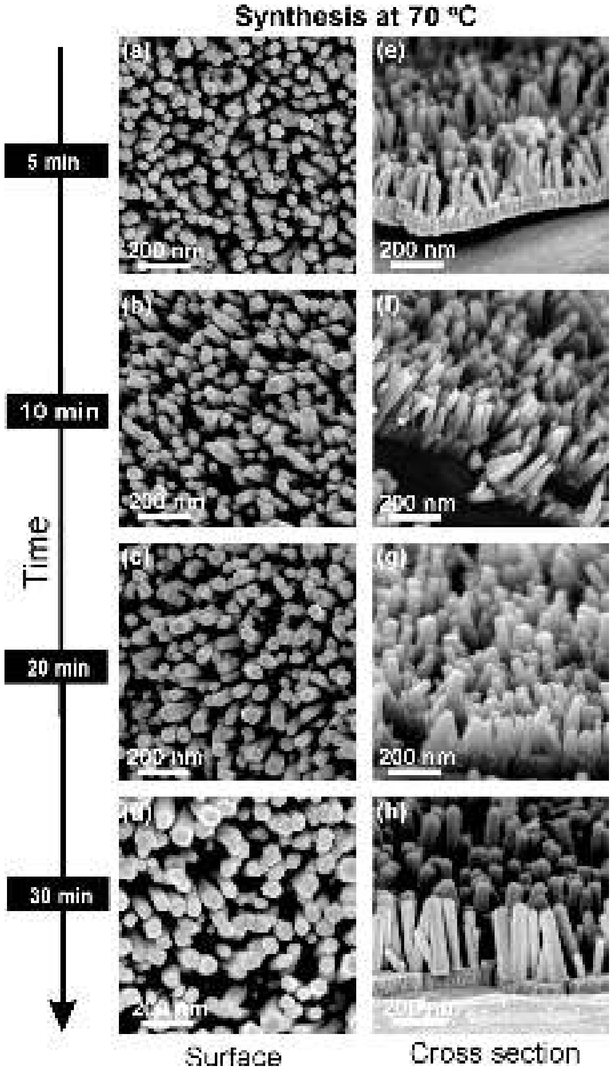

Figure 4.21 Surface and cross section SEM images of ZnO NRs produced by the hydrothermal method assisted by microwave radiation, at 70 °C, with different synthesis times on cardboard substrate: (a, e) 5 min, (b, f) 10 min, (c, g) 20 min, (d, h) 30 min.

Figure 4.21 shows the SEM analysis of samples produced with different temperature (70, 90, 110 and 130 °C), for 30 minutes. With the increase of synthesis temperature, it is interesting to observe that the ZnO NRs become wider and then thinner again. The NRs' diameter increases from approximately 70 (± 5) nm (at 70 °C) to 120 (± 20) nm (at 90 °C), decreasing to 80 (± 5) nm (at 110 °C) and then to 50 (± 5) nm (at 130 °C). This may be due to the fact that the microwave power needs to be turned on more frequently during the synthesis in order to maintain the higher temperatures [257]. Regarding the NRs length, it increases monotonously from 300 (± 20) nm to 500 (± 20) nm with the increase of temperature, in accordance with literature studies [258]. Besides, with the increase of synthesis temperature the ZnO NRs become more misaligned and the top of the NRs becomes sharper. With the increase of temperature, the NRs' top goes from flat to a pencil-like shape. This may be related with anisotropy in the growth rate direction, caused by the increase of temperature. In the hydrothermal synthesis of ZnO it has been reported by some authors that the higher crystal growth velocity is in the [0001] direction [259]. As such, the appearance of the pencil-like NRs structure suggests that the growth rate of the (001) crystal facet is relatively faster at higher temperature, when compared with the NRs with a flat top, produced at lower temperature [259,260].

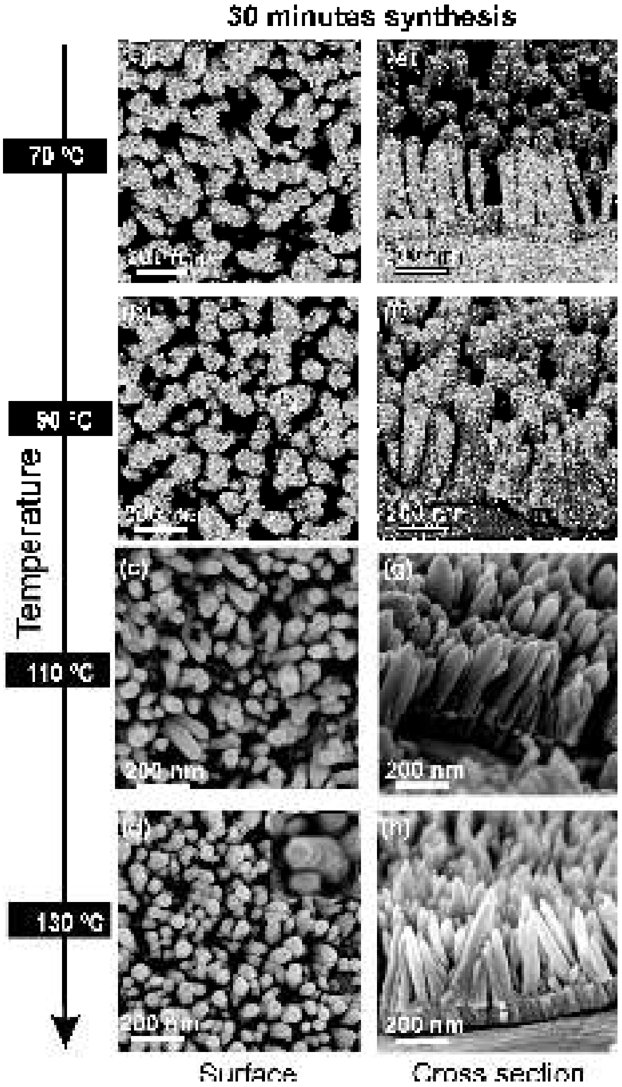

Figure 4.22 Surface and cross section SEM images of ZnO NRs produced by hydrothermal method assisted by microwave radiation, for 30 minutes, with different synthesis temperatures, on cardboard substrate: (a, e) 70 °C, (b, f) 90 °C, (c, g) 110 °C, (d, h) 130 ° C.

The XRD diffractograms of the produced ZnO nanorod arrays grown on cardboard substrate are presented in Figure 4.23. All samples present similar XRD patterns, indicating that the ZnO NRs possess high crystallinity. It is possible to observe that, for all the produced samples, a single peak at 2θ = 34.4° is present, being fully assigned to the (002) plane of the hexagonal wutzite ZnO structure, displaying a lattice constant of a = 0.3296 nm and c = 0.5207 nm, in accordance with [261]. This result shows that the ZnO NRs are well oriented along the c-axis direction.

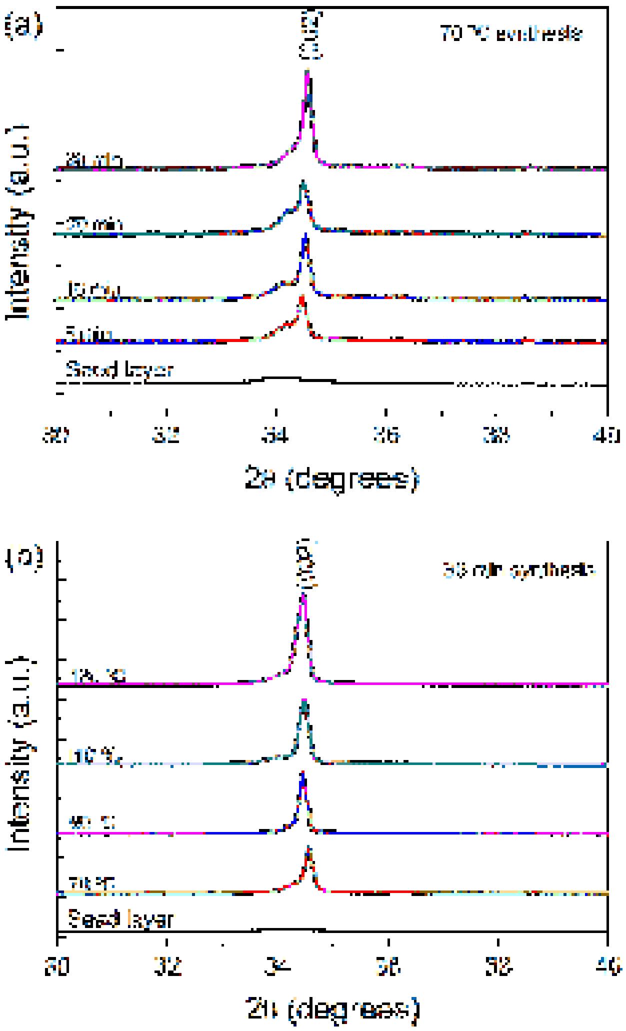

Figure 4.23 XRD diffractograms of ZnO nanorod arrays produced by the hydrothermal method assisted by microwave radiation, (a) with a temperature of 70 °C for 5, 10, 20 and 30 minutes, and (b) for 30 min with a temperature variation between 70 and 120 °C.

For synthesis at 70 °C, with different process times (see Figure 4.23 a), the peak intensity increases with the increase of synthesis time, which can be attributed to the increase of the grain size [262] or to the increase of NRs' length (as confirmed by the SEM images of Figure 4.21). A higher rod width will also increase the XRD signal.

With the increase of synthesis temperature there is an increase of the intensity of the (002) peak, which suggests that the ZnO NRs become more crystalline. This can be attributed to a change in the crystal size of the ZnO material along the rods (see Figure 4.23 b) [262]. Also, it is possible to see that, for lower synthesis temperatures, a broad peak still appears which corresponds to the XRD diffraction of the seed layer. This bump disappears with the increase of the synthesis temperature, probably due to the increase of the NRs' size. At higher synthesis temperatures, other ZnO crystallographic peaks starts to appear (even if they are almost imperceptible), which indicates that the NRs start to become more misaligned. These results confirm that pure and quasi-aligned ZnO nanostructures were obtained by microwave-assisted synthesis on cardboard substrates, in accordance with what was observed in the SEM micrographs of Figures 4.21 and 4.22.

The optical bandgap of the ZnO nanorod structures, produced with different synthesis temperature and time on the cardboard substrates, was evaluated from the reflectance spectra shown in the insets of Figure 4.24. The Al coating on such substrates acts as a mirror, reflecting most of the impinging light. Therefore, the decrease of reflection is mainly given by light absorption occurring in the ZnO NRs material. As such, its bandgap can be determined through the Tauc equation for direct band semiconductors [263]:

$$(\alpha h\nu)^{m} = A(h\nu - E_g) \tag{4.3}$$

where α is the material absorption coefficient, h is the Plank constant, ν is the frequency, m is a constant that depends on the type of optical transition (i.e. $m = 1/2$ for allowed direct transitions and $m = 2$ for allowed indirect transitions), A is a photon energy-independent constant and E_g is the material optical bandgap.

Figure 4.24 shows the optical bandgap calculated by extrapolating $(\alpha h\nu)^2$ vs. $h\nu$. It is possible to observe that, in general, the ZnO NRs absorb almost all light in the UV region as the material reflectance almost decays to zero. The higher reflectance in the visible range, observed for the sample with only the ZnO seed layer, is due to the low thickness of the layer (100 nm) and to the small sputtered ZnO grains that absorb less radiation.

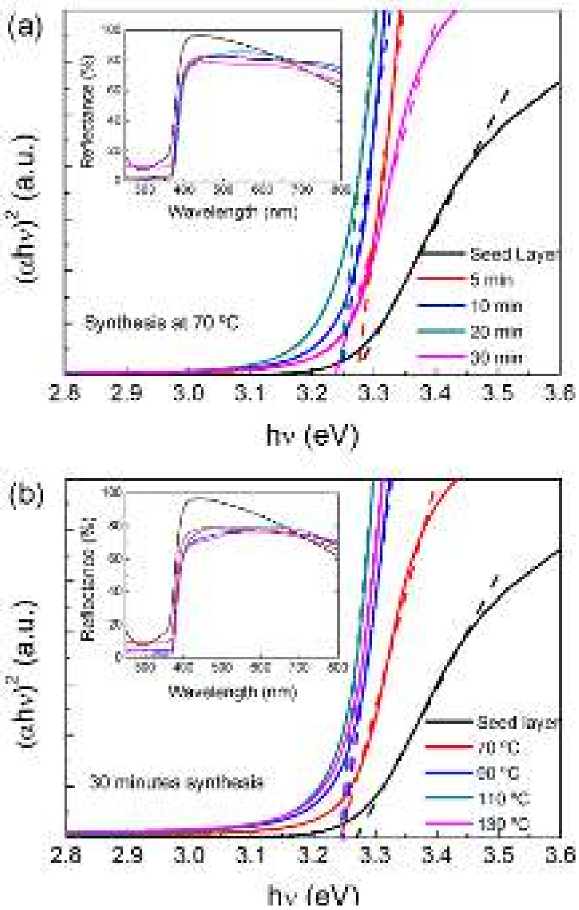

Figure 4.24 Tauc plots used for the determination of the optical bandgap of the ZnO nanorod arrays produced by the hydrothermal method assisted by microwave radiation, on cardboard substrate, (a) with a temperature of 70 °C for 5, 10, 20 and 30 minutes, and (b) for 30 min with a temperature variation between 70 and 130 °C.

The estimated optical bandgap values are indicated in Table 4.1. The bandgap decreases with the increase of synthesis time, changing from 3.27 eV to 3.24 eV. However, with the increase of synthesis temperature, the bandgap value remains constant at 3.24 eV. It is well known that the optical bandgap of a semiconductor depends on distinct parameters, such as the residual strain, crystal defects, impurities and grain size confinement [264]. Moreover, the bandgap value usually decreases with the increase of grain size and NRs length.

Table 4.1 Optical bandgap of ZnO NRs, produced with different synthesis time and temperature, obtained by extrapolating $(\alpha h\nu)^2$ vs. hν.

Synthesis time	Seed layer	5 min	10 min	20 min	30 min
70 °C	3.275 eV	3.275 eV	3.265 eV	3.242 eV	3.240 eV

Synthesis temperature	Seed layer	70 °C	90 °C	110 °C	130 °C
30 min	3.275 eV	3.240 eV	3.242 eV	3.241 eV	3.241 eV

4.2.3.3 Decoration of Ag nanoparticles on ZnO NRs cardboard substrate

The ZnO NRs need to be decorated with MNPs to exhibit SERS activity, thus the NRs were coated with Ag NPs deposited by thermal evaporation (Ag NPs@ZnO NRs). As previously reported [92], the desirable particle sizes for molecular SERS detection correspond to those formed with a 6 nm Ag mass-equivalent film thickness, resulting in a uniform array of NPs with average long-axis diameter of around 60 nm. Figure 4.25 shows the variation of the Ag NPs structures, formed from such 6 nm mass thickness, when deposited on ZnO NRs produced at 70 °C with different synthesis times.

Close-packed Ag NPs are distributed uniformly on the top and sidewalls of the hexagonal ZnO NRs, leading to a large surface-to-volume ratio of the plasmonic nanostructure. The average Ag NPs diameter (*D*) was measured for all samples (indicated in Figure 4.25) and it was found that it decreases when decreasing the NRs synthesis time. Such decrease is due to the lower NRs width (thus lower sidewall area, see figure 4.21) which hinders the coalescence of the Ag NPs during their formation [172]. Nonetheless, the average separation between adjacent Ag NPs remains similar (less than 5 nm) for all cases of Figure 4.25, which is critical to create high SERS activity within their interspace excited by the surface plasmon coupling between the narrow gaps (called "hot spots") of neighboring NPs [94,95].

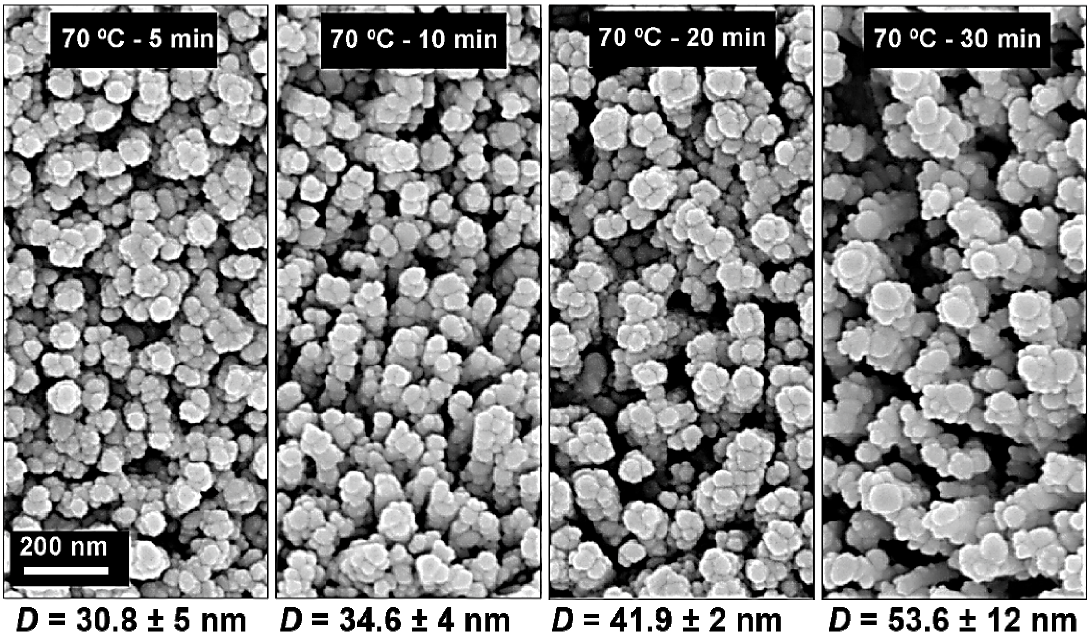

Figure 4.25 SEM images of ZnO NRs with Ag NPs deposited by thermal evaporation. The NRs were produced at 70 °C, with different synthesis times (5, 10, 20 and 30 minutes). The corresponding values of the average NP size (in-plane major axis, *D*) of the Ag NPs deposited on the NRs, from 6 nm mass equivalent thicknesses, are indicated below the images.

EDS mapping has been carried out and is presented in Figure 4.26 for the ZnO samples produced at 70 ˚C with a synthesis time of 5 min. The EDS analyses attested to the homogeneous distribution of Ag NPs, covering completely the ZnO NRs surface.

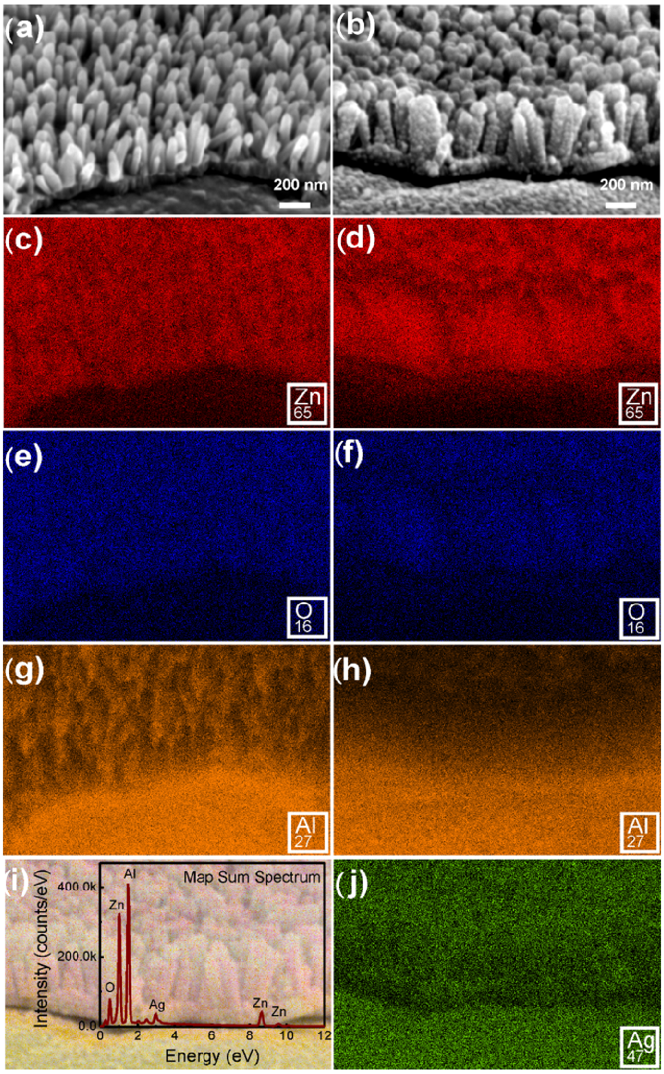

Figure 4.26 SEM images of ZnO NRs formed at 70 °C with a synthesis time of 5 min (a) and ZnO NRs covered with Ag NPs (b). The respective X-ray maps corresponding to Zn are presented in (c) and (d), O in (e) and (f), Al in (g) and (h), and Ag in (j). i) Map sum spectrum of the sample with Ag NPs covering the ZnO NRs.

To study the localized surface plasmon resonance spectral positions of the SERS substrates, the NPs absorptance spectra, Abs (Figure 4.27), determined from the total reflectance, R_{TOT}, spectra before and after the Ag NPs deposition, was calculated using the following equation:

$$\mathrm{Abs} = \mathrm{R}_{\mathrm{TOT}}\left(\mathrm{Substrate} + \mathrm{ZnO\ NRs}\right) - \mathrm{R}_{\mathrm{TOT}}\left(\mathrm{Substrate} + \mathrm{ZnO\ NRs} + \mathrm{NPs}\right) \tag{4.4}$$

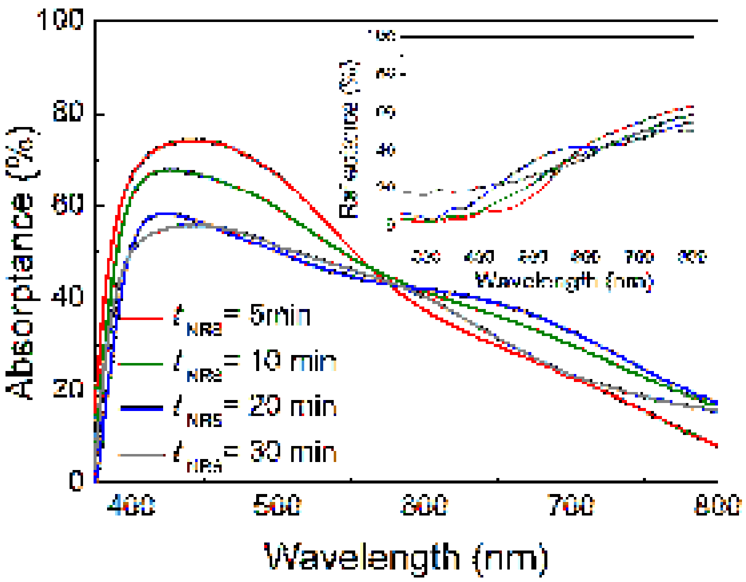

Figure 4.27 UV–Vis-NIR absorption spectra of the ZnO NRs substrates produced at 70 °C, with different synthesis times (5, 10, 20 and 30 minutes), after Ag NPs deposition with 6 nm Ag mass equivalent thickness.

It should be pointed out that the spectrophotometry measurements of Figure 4.26 can only detect the far-field light extinction caused by the particles; but, they do not probe their near-field light scattering, which is responsible for SERS. Nevertheless, the analysis of such spectra is important to determine the spectral location and extension of the LSPRs and, thereby, enable the matching with the wavelengths of the incident laser and Raman-scattered photons.

4.2.3.4 Implementation of 3D cardboard substrate as SERS device

SERS device characterization

Figure 4.28 (a) shows that the intensity of the Raman signal (using 10^{-6} M R6G analyte solution) is pronouncedly amplified when the NRs synthesis time (t_{NR}) decreases from 30 to 5 minutes. For the determination of the EF (Figure 4.28 b), the calculations of the intensities consider the area under the Raman vibrational lines at 1360 cm^{-1}. The average EF obtained with the t_{NR} = 30 min substrate was 3×10^4, while with the t_{NR} = 5 min substrate an average enhancement of 7.0×10^5 was achieved. The observed trend of higher EF with lower nanorod synthesis time is chiefly attributed to the higher number of Ag NPs present per unit area of the substrate surface. Figure 4.28 (b) presents a correlation between the EF variation and the estimated number of nanoparticles (N_{NPs}) per μm^2, as function of the different ZnO synthesis times.

The observed highest SERS enhancement of the t_{NR}= 5min substrate can be ascribed to the higher estimated NPs density on the sample, due to the increase of the

NRs density (described in section 4.2.3.2), providing an increase in the total number of plasmonic “hot-spots” and an extended area for the deposition of analyte molecules covered by such regions of strong near-field intensity [117,181,252].

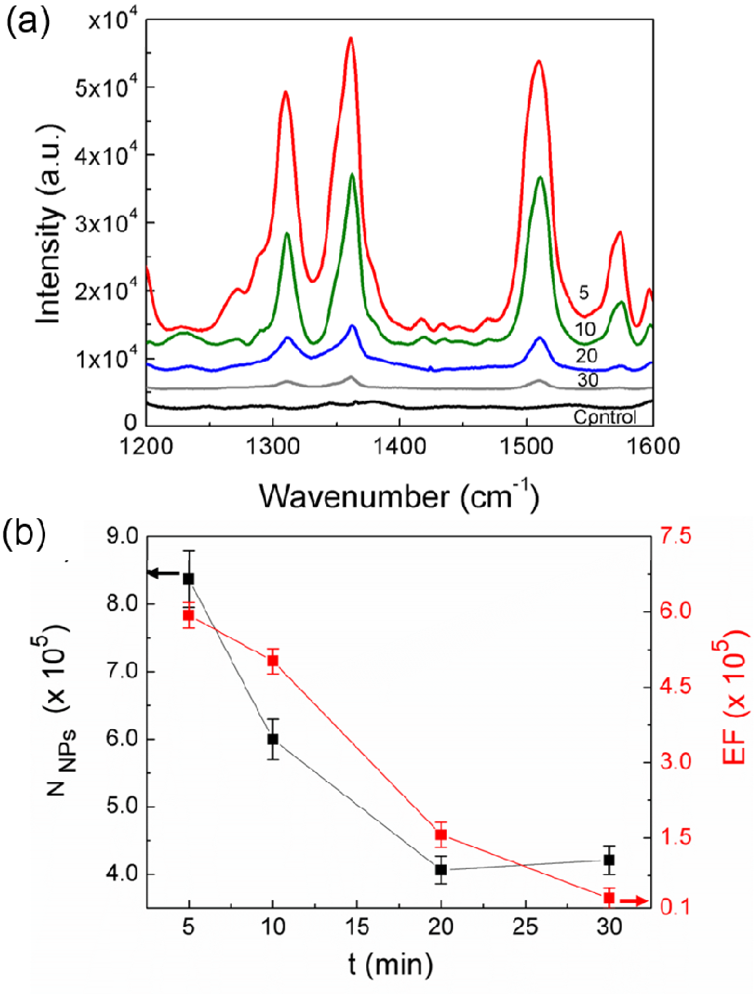

Figure 4.28 (a) Raman spectra of 10^{-6} M of R6G on ZnO NRs with and without (control) Ag NPs. The NRs were produced at 70 °C, with different synthesis times (5, 10, 20 and 30 minutes). (b) Enhancement factor (EF) and estimated number of Ag nanoparticles (N_{NPs}) per micrometre square, as function of the ZnO NRs synthesis times. The points in the plot have an associated error estimated by analyzing, for the different points, sets of 3 samples fabricated with the same parameters.

In Figure 4.29 it is possible to observe the variation of Ag NPs deposited on ZnO NRs produced for 30 minutes, with different synthesis temperatures varying from 70 °C to 130 °C. In this case, the Ag NPs present different diameters, which approximately follow the trend of the NRs average width shown in Figure 4.22. However, despite the fact that the morphology, alignment and density of the NRs changes considerably for this set of samples, the SERS signals obtained were similar (with EF ~ 10^5), regardless of the different NRs synthesis temperatures. This may be due to the fact that, for higher temperatures, the ZnO NRs density decreases and the top of the NRs goes from flat to pencil-like tops, leading to the decrease of the number of “hot-spots” on the NRs’ upper illuminated part. On the other hand, since at higher temperatures the NRs became misaligned (as previously reported), the unpolarized illuminating electric field incident from the top becomes more aligned with the longest NPs axes along their base diameter, thus allowing higher electromagnetic enhancement than for the vertically-aligned NRs. This can compensate the disadvantageous pencil geometry of the NRs formed at higher temperature and contribute to keep approximately unchanged the SERS signal among the structures of Figure 4.29.

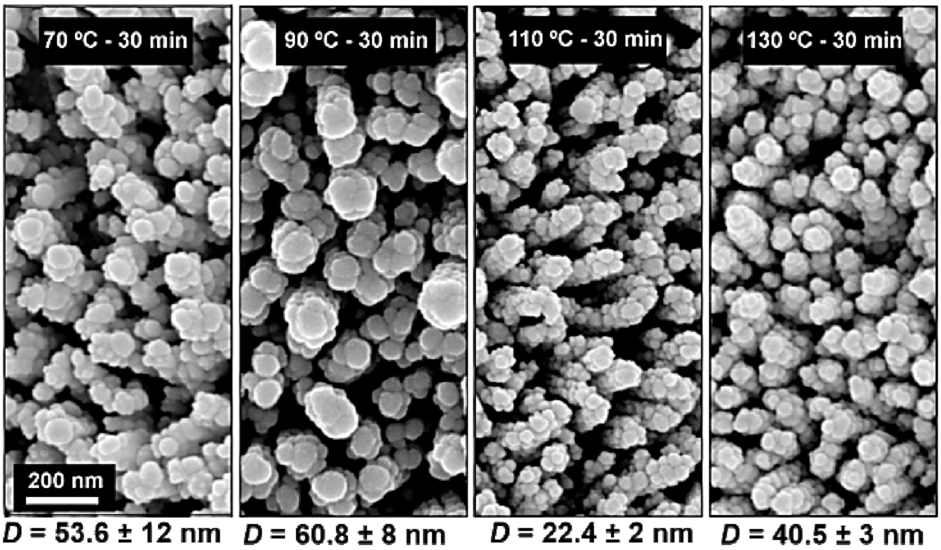

Figure 4.29 SEM images of ZnO NRs with Ag NPs deposited by thermal evaporation. The NRs were produced for 30 minutes, with different synthesis temperatures (70, 90, 110 and 130 °C). The values for the average size (in-plane major axis, *D*) of the deposited Ag NPs from 6 nm mass thicknesses are indicated.

Uniformity and stability of the cardboard SERS device

To test the uniformity of the best-performing substrate (t_{NR} = 5 min, covered with 6 nm Ag mass thickness), additional SERS spectra of 10^{-6} M R6G molecules were collected from 6 randomly-selected spots on the same substrate (2.5 x 2.5 cm^2 area) separated by a distance of at least 1 cm. From Figure 4.30 it is possible to observe that Raman spectra profiles revealed to be quite similar, indicating high uniformity of the Ag NPs@ZnO NRs substrates and good reproducibility of the SERS signal. The stability of the SERS cardboard substrates has been tested by comparing the Raman signals produced by freshly prepared samples with those measured after 6 months of storage, showing that the Raman peaks profile is similar to that of the newly prepared sample, suggesting a rather stable SERS substrate.

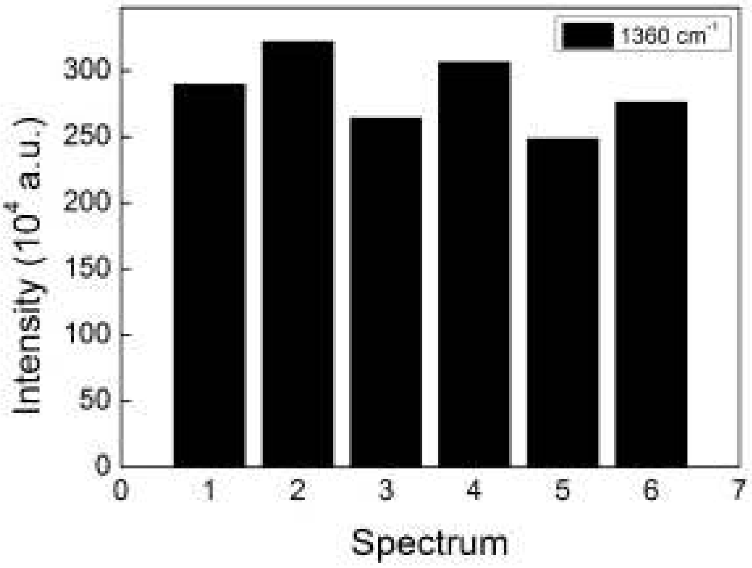

Figure 4.30 Intensities of the 1360 cm^{-1} Raman vibrational lines of the spectra of 10^{-6} M R6G, acquired from the best-performing substrate (t_{NR} = 5 min, covered with 6 nm Ag mass thickness) at 6 randomly selected spots on its surface. Each bar corresponds to the average from five individual spectra measured within the vicinity of each spot.

Figure 4.31 presents a correlation between the EF at 1360 vibration line, and the amount of R6G present. It is noteworthy that the Raman signal can still be observed at an amount as low as 10^{-8} M. The SERS measurements of the Ag NPs@ ZnO NRs sample using 10^{-8} M R6G resulted in the maximum EF value (~4.6×10^9) attained in this work.

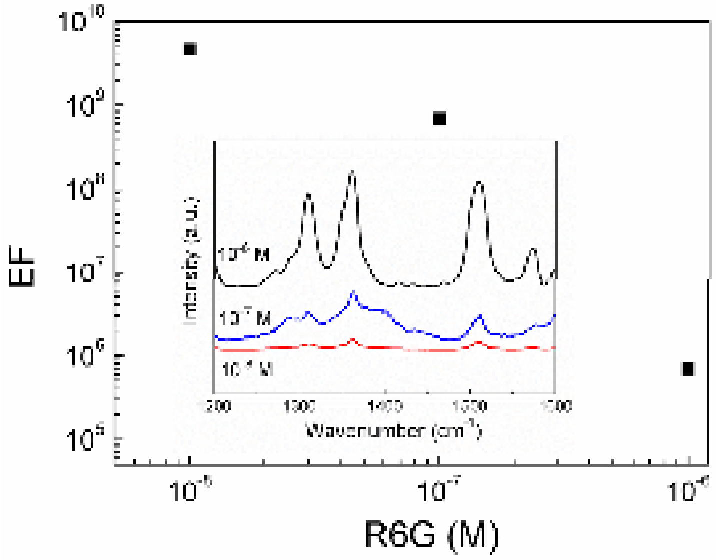

Figure 4.31 Values of the EF at the 1360 vibrational line for the different amounts of R6G (10^{-6}, 10^{-7}, 10^{-8} M) added to the SERS substrate. Inset: Raman spectra of the best-performing substrate from mean average value of hundred measurements, at the different amounts (10^{-6}, 10^{-7}, 10^{-8} M) of R6G.

4.2.3.5 Conclusion

In this work, ZnO NRs were synthesized on cardboard substrates by an innovative ultrafast method based on hydrothermal synthesis assisted by microwave radiation. A set of synthesis times (5-30 min) and temperatures (70-130 °C) were tested. As the synthesis time and temperature increase, the diameter and length of the resulting ZnO NRs also increases. Their material bandgap decreases with the increase of time and temperature, suggesting an increase of crystallite size. With the deposition of Ag NPs over the ZnO NRs, it was possible to test the produced substrates as platforms for SERS application, obtaining a remarkable average EF value of 4.6×10^9, with the NRs scaffold produced at 70 °C for 5 minutes.

The results presented here show that it is possible to grow well-aligned and highly crystalline ZnO NRs on cardboard-type substrates, using an ultra-fast method, and that it is possible to use it as a low-cost, disposable platform for SERS detection in chemical and biological analytical devices.

Chapter 5

Conclusions and Future Perspectives

This thesis was aimed at the implementation of self-assembled plasmonic nanostructures for light trapping in thin film silicon solar cells and surface enhanced Raman spectroscopy.

First, the morphology and optical properties of nanoparticles with different sizes, fabricated by a solid-state dewetting process (temperature of 500 °C for 20 min, with a heating rate of 16 °C/s), was analyzed on different underlying surface materials like glass, ZnO, GZO and AZO coated glass substrates. The study revealed that both the thermal conductivity and surface roughness of the underlying surface layer play a determinant role on the morphology of the nanostructures formed. It was verified that higher conductivity induces a higher mobility of the Ag material on the surface and, consequently, a higher NPs coalescence during annealing, resulting in higher Ag NPs sizes. On the other hand, the surface roughness causes obstacles to such mobility and, consequently, to the size increase of the NPs via coalescence; besides worsening the uniformity of the resulting nanostructures. It is also concluded that the parasitic absorption is reduced and the scattering is enhanced by forming Ag NPs on a thin (30 nm) AZO film, with good conductivity ($\sigma = 59.5$ Scm^{-1}) and low surface roughness (~1 nm), which yielded relatively large (100-300 nm) particles with a semi-spherical shape and with 8% surface coverage. Next, the incorporation of NPs in the rear contact of silicon solar cells, in a substrate (nip) configuration was investigated. Aimed at the investigation of plasmonic light trapping for nip thin film silicon solar cells, the best condition (6 nm mass thickness of Ag on AZO underlying surface) were used in the back contact of μc-Si:H solar cells. The selected deposition conditions assured well-distributed Ag MNP arrays with a size distribution within the appropriate range (~100-300 nm) for lower parasitic absorption and strongest far-field light scattering within the cells. As previously mentioned, in solar cell applications, the Ag NPs are embedded in an AZO layer which is in contact with a silver mirror. This means that other parameters need to be taken into account for the optimization of the AZO layer. Namely, the distance between the MNPs and the Ag mirror ($d_{\text{Ag-NPs}}$), in order to optimize the distance-dependent optical interaction (parasitic absorption and scattering). The study revealed that the annealing process time can be reduced to 10 min by increasing the temperature ramp-up rate. Inducing the dewetting mechanism with an ultra-fast temperature ramp rate (150 °C/s), revealed to be very beneficial for faster formation of the desired NPs structures during annealing. This is because the rapid uptake of thermal energy by the precursor Ag film causes the film to be more favorably transformed (broken) into NPs with the preferential larger (>100 nm) sizes. Next, the structural properties of NPs formed on AZO spacer layers with different thicknesses, were investigated and it was found that (i) the $d_{\text{Ag-NPs}}$ had no effect on the morphology of Ag NPs for $d_{\text{Ag-NPs}}$ from 30 to 140 nm; (ii) for $d_{\text{Ag-NPs}}$ lower than 30 nm the formation of thin films occurs. It was verified that the AZO layer in contact with the Ag mirror has no influence on the morphological properties of the NPs, contrary to what happened when the NPs were formed in an underlying surface of AZO without a mirror layer, which can be attributed to the similarity of conductivity and roughness values. By analysing the optical properties of this set of distinct PBRs in the 600–1200 nm wavelength range, it has been shown that (i) there is an intermediate distance, $d_{\text{Ag-NPs}}$ = 40 nm, where the diffuse reflectance reaches a maximum and the total reflectance a minimum; (ii) for thicknesses higher than 40 nm, the thicker the spacer the higher the total and the lower the diffuse reflectance and (iii) for thicknesses lower than 40 nm, the diffuse reflectance starts to decrease and the total reflectance increases. The obtained results are in accordance with the theoretical predictions found in the literature.

Afterwards, plasmonic light trapping in PBR configuration was implemented in thin film μc-Si:H solar cells. By analysing sets of solar cells built on distinct $\mathrm{d}_{\text{Ag-NPs}}$, it is shown that the best-performing PBRs were achieved for $\mathrm{d}_{\text{Ag-NPs}}$=100 nm, which is attributed to (i) strong scattering of light in the IR from the PBR; (ii) less parasitic absorption (lower optical losses) in the PBR configuration (ii) induced front surface structuring which improves anti-reflection. As a result, higher values of J_{ph} were achieved in comparison to planar and other PBR configurations, and similar to the state-of-the-art of plasmon-enhanced μc-Si:H solar cells. However, some cracks appeared near the n/i interface and inside the intrinsic layer resulting in the formation of sharp valleys around the Ag NPs, which resulted in a slight decrease of FF and Voc. To overcome this issue, different ZnO:Al spacer layers on top of the Ag NPs were tested. On the best-performing solar cells, obtained with $d_{\text{Ag-NPs}}$=100 nm, different ZnO:Al spacer layers ($d_{\text{NP-Si}}$) on top of the Ag NPs were tested. It was found that, when the $d_{\text{NP-Si}}$ is increased from 30 to 60 nm, the Voc and FF improved. This can be ascribed to an improved surface morphology, which is beneficial for the growth of dense Si materials with less cracks. Therefore, we can conclude that a spacer layer between the Ag NPs and the n-doped μc-Si:H layer should be optimally designed to provide a good surface to grow high-quality μc-Si:H materials and to avoid the low scattering and strong parasitic absorption of the Ag NPs in the long wavelengths. The microcrystalline silicon solar cells deposited on such improved PBRs achieved an overall enhancement of 11% on efficiency, corresponding to a photocurrent of 24.4 mA/cm^2 and an efficiency of 6.78 %, against 21.79 mA/cm^2 and 6.12 %, respectively, obtained on flat structures without NPs.

The second part of this thesis (chapter 4) was dedicated to the development and application of MNPs for Raman enhancement. Since the focus was the development of plasmonic cellulose-based SERS substrates, a simple, uniform, reproducible and large scale one-step method to deposit MNPs on the cellulose-based substrates was developed. This methodology revealed that individual nanoparticles arrays with good control of their size and shape can be deposited without any post-deposition thermal procedures. Next, we developed a new kind of cost-efficient SERS substrate (cardboard substrate). On this type of substrate, different sizes of NPs were investigated, and their influence on the SERS signal was analysed. The study revealed that the best average enhancement ($EF=1\times10^{6}$) using R6G (10^{-6} M) was achieved for the nanoplasmonic cardboard SERS substrate obtained from 6 nm Ag mass thickness, which is attributed to the (i) spectral matching of the plasmonic resonance (λ_{LSPR} = 660 nm) with the excitation laser; (ii) high local electric field enhancement produced the resulting 60 nm-sized Ag NPs, as predicted by Mie theory analysis. It was also verified that the samples were found to be stable for at least 6 months. Next, we applied the same conditions and the same type of NPs on a different cellulose based substrate (raw paper). The study revealed that raw SERS substrates showed an EF ($\sim10^{5}$) lower than cardboard substrate, which may be ascribed to the influence of the aluminium layer of the cardboard substrate that shifts the LSPR for wavelengths near the laser, and originates a constructive interaction with the particles that increases their near-field amplitude [23,265]. To overcome this issue, a different approach to increase the SERS signal of these substrates was tested. The study revealed that ZnO NRs synthesized by a simple, fast and low-temperature hydrothermal method, and decorated with Ag NPs, can enhance the Raman signal from $EF=1.6\times10^{5}$ (substrate without NRs) to $EF=1\times10^{6}$, which is attributed to the (i) lower inter-Ag-NPs gaps for 3D geometry; (ii) natural inclination of the ZnO NRs and (iii) larger sensing area allowed by the NR scaffolds. Next, we tested different amounts of R6G on the Ag NPs@ ZnO NRs paper substrate and we concluded that the Raman signal can still be observed at an amount as low as 10^{-9} M, resulting in the maximum EF value ($\sim1\times10^{7}$) attained in this work. However, the stability of this substrate (Raman signal stable for only one month) is lower than with cardboard substrate, which may be ascribed to the lower oxidation of the NPs in the presence of the aluminium layer in the cardboard structure. This metal layer may be acting as a sacrificial layer, providing anodic protection and preventing possible oxidation of the NPs. This theory gained support via preliminary results on aluminium kitchen foil, that demonstrated that the stability of the SERS substrates can be greatly enhanced on substrates with a sacrificial metal layer in contact with the MNPs.

Aimed at the investigation of higher efficient, uniform and stable SERS substrates, the best substrates and best configuration described in the previous section were further investigated. Using the cardboard material as SERS substrate, different ZnO NRs morphologies were grown and their influence on the NPs deposition was tested. It was verified that the main quantity for the correlation between the NPs sizes and the NRs morphology is the NRs average width. The study revealed that lower NRs width (thus lower sidewall area) hinders the coalescence of the Ag NPs during their formation, leading to NPs with smaller sizes. One aspect that proved to be crucial, is the surface area covered by the NPs "hot spots" (near-field). By analysing sets of SERS devices on distinct NRs width, it is shown that the maximum enhancement of the Raman signal (EF value ~7×10^5) was achieved for lower NRs width (45 nm). The observed highest SERS enhancement of this substrate can be ascribed to the higher estimated NPs density on the sample due to the (i) increase in the total number of plasmonic "hot-spots" and (ii) an extended area for the deposition of analyte molecules covered by such regions of strong near-field intensity. Besides, SERS measurements were performed on different substrates, produced in separate batches using the same best-performing conditions, yielding quite similar results; which proves the reproducibility of the method.

Finally, we tested different amounts of R6G on the best-performing Ag NPs@ ZnO NRs cardboard substrates, and concluded that the Raman signal can still be observed at an amount as low as 10^{-8} M, resulting in the maximum EF value (~4.6×10^9) attained in this work.

Concerning perspectives for future developments, the points to be addressed in the future concerns mainly the design and architecture to be used, besides the proper selection of the nanoparticles, aiming to enable further improvements. In terms of the efficiency of thin film silicon solar cells, the combination of photonic dielectric structures [266,267] on the front contact together with the plasmonic MNPs on the cell back contact cell can be quite promising for broadband absorption enhancement. This is because the front photonic structures mainly allow pronounced anti-reflection action in the shorter (UV-visible) wavelengths, while the plasmonic MNPs act more strongly in the near-infrared. Furthermore, future work should focus on the minimization of the optical losses caused by the MNPs, by improving the uniformity of the NPs. Although this work focuses on thin film microcrystalline Si technology, it is also worth exploring plasmonic nanostructures fabricated by solid-state dewetting for application in different types of thin film solar cells, like those based on CIGS, CZTS, Perovskites, OPV, etc.

Concerning plasmonic SERS substrates, the fabrication methods employed in this thesis can be further optimized to deposit new materials, such as Ag/Au core/shell nanoparticles, to achieve even better stability and biocompatibility, and to continue to improve the ZnO NRs morphology in order to obtain a higher density of hotspots, by reducing the gap between NPs to a distance below 10 nm, ideally, 2 nm. With this, it its envisaged that very highly efficient, uniform and reproducible SERS substrates can be obtained in a variety of platforms such as glass, paper or plastic and metallic foils. With such highly efficient SERS substrates, the direct detection of different analytes such as, sulphites, toxins, pesticides or cells will be possible. It is also foreseen the combination of SERS substrates with microfluidic devices which can provide analyte concentration and separation allowing even a better discrimination.

References

[1] Economou E N 1969 Surface Plasmons in Thin Films *Phys. Rev.* **182** 539

[2] Burke J J, Stegeman G I and Tamir T 1986 Surface-polariton-like waves guided by thin, lossy metal films *Phys. Rev. B* **33** 5186

[3] Maier S A 2007 “Electromagnetics of metals” *Plasmonics:Fundamentals and Applications* (Springer US) pp 5–19

[4] Drude P. 1900 Zur Elektronentheorie der Metalle *Ann. Phys* **306** 566–613

[5] Ashcroft N W and Mermin N D 1976 *Solid State Physics* ed R W Holt and & Winston (New Jersey)

[6] Kittel C 2005 *Introduction to Solid State Physics* ed N Hoboken (Wiley)

[7] Johnson P B and Christy R W 1972 Optical Constants of the Noble Metals *Phys. Rev. B* **6** 4370

[8] Johnson P B and Christy R W 1974 Optical constants of transition metals: Ti, V, Cr, Mn, Fe, Co, Ni, and Pd *Phys. Rev. B* **9** 5056

[9] Hartland G V 2011 Optical Studies of Dynamics in Noble Metal Nanostructures *Chem. Rev.* **111** 3858–87

[10] Johnson P and Christy R 1972 Optical constants of the noble metals *Phys. Rev. B* **1318** 1951–4

[11] Spinelli P, Hebbink M, de Waele R, Black L, Lenzmann F and Polman A 2011 Optical impedance matching using coupled plasmonic nanoparticle arrays. *Nano Lett.* **11** 1760–5

[12] Morawiec S, Mendes M J, Mirabella S, Simone F, Priolo F and Crupi I 2013 Self-assembled silver nanoparticles for plasmon-enhanced solar cell back reflectors: correlation between structural and optical properties. *Nanotechnology* **24** 265601–12

[13] Mendes M J, Luque A, Tobías I and Martí A 2009 Plasmonic light enhancement in the near-field of metallic nanospheroids for application in intermediate band solar cells *Appl. Phys. Lett.* **95** 071105–8

[14] Wurtz G a., Hranisavljevic J and Wiederrecht G P 2003 Electromagnetic Scattering Pathways for Metallic Nanoparticles: A Near-Field Optical Study *Nano Lett.* **3** 1511–6

[15] Bortchagovsky E G, Klein S and Fischer U C 2009 Surface plasmon mediated tip enhanced Raman scattering *Appl. Phys. Lett.* **94** 063118–20

[16] Bohren C F and Huffman D R 1983 *Light Scattering by Small Particles* (New York: Dover Publications, Inc.)

[17] Bohren C F and Huffman D R 2004 *Absorption and Scattering of Light by Small Particles* (Weinheim: Wiley)

[18] Maier S A 2007 Localized surface plasmons *Plasmonics: Fundamentals and Applications* (Wiley-VCH Verlag GmbH) pp 65–88

[19] Mendes M J, Luque A, Tobías I and Martí A 2009 Plasmonic light enhancement in the near-field of metallic nanospheroids for application in intermediate band solar cells *Appl. Phys. Lett.* **95** 071105

[20] Mie G 1908 Beiträge zur Optik trüber Medien, speaiell kolloidaler Metallösungen *Ann. Phys* **25** 377

[21] Schmid M, Klenk R, Lux-steiner M C and Topiˇ M 2011 Modeling plasmonic scattering combined with thin-film optics *Nanotechnology* **22** 025204

[22] Mendes M J, Hern E, Tob I and Luque A 2013 Self-organized colloidal quantum dots and metal nanoparticles for solar cells *Nanotechnology* **24** 345402

[23] Mendes M J, Morawiec S, Simone F, Priolo F and Crupi I 2014 Colloidal plasmonic back reflectors for light trapping in solar cells *Nanoscale* **6** 4796–805

[24] Morawiec S, Mendes M J, Filonovich S A, Mateus T, Mirabella S, Águas H, Ferreira I, Simone F, Fortunato E, Martins R, Priolo F and Crupi I 2014 Broadband photocurrent enhancement in a-Si:H solar cells with plasmonic back reflectors *Opt. Express* **22** A1059–A1070

[25] Dale B E, Ong R G and Lakes D O E G 2014 and evaluation of sustainable bioenergy production systems *Biofuels, Bioprod. Bioref.* **8** 487–503

[26] Fanchi J R 2004 *Energy Technology and Directions for the Future* (Elsevier)

[27] World energy InvestIment 2016 *World energy Investment 2016* (IEA)

[28] Chopra K L, Paulson P D and Dutta V 2004 Thin-Film Solar Cells: An Overview *Prog. Photovoltaics Res. Appl.* **92** 69–92

[29] Ountries C, Martinot E, Chaurey A, Lew D, Moreira R and Wamukonya N 2002 Renewable Energy Markets in Developing Countries *Annu. Rev. Energy Environ.* **27** 309–48

[30] Hegedus S S and Luque A 2005 Status, Trends, Challenges and the Bright Future of Solar Electricity from Photovoltaics *Handbook of Photovoltaic Science and Engineering,* ed A Luque and S S Hegedus (John Wiley & Sons) pp 1–44

[31] Kreith F and Goswami D . Y 2008 *Handbook of Energy Efficiency and Renewable Energy* (Goswami: CRC Press)

[32] Hishikawa Y, Warta W, Green M A, Levi D H, Hohl J, Anita E, Baillie W Y H and Dunlop E D 2017 Solar cell efficiency tables (version 50) *Prog. Photovoltaics Res. Appl.* **25** 668–76

[33] Yoshikawa K, Kawasaki H, Yoshida W, Irie T, Konishi K, Nakano K, Uto T, Adachi D, Kanematsu M, Uzu H and Yamamoto K 2017 Silicon heterojunction solar cell with interdigitated back contacts for a photoconversion efficiency over 26% *Nat. energy* **2** 1–8

[34] Kayes B M, Nie H, Twist R, Spruytte S G, Reinhardt F, Kizilyalli I C and Higashi G S 2011 27 . 6 % conversion efficiency , a new record for single-junction solar cell under 1 sun illumination *Proc. 37th IEEE Photovolt. Spec. Conf.* 4–8

[35] Shockley W and Queisser H J 1961 Detailed Balance Limit of Efficiency of pn Junction Solar Cells *J. Appl. Phys.* **32** 510–9

[36] Liu W, Zhang H, Wang H, Zhang M and Guo M 2017 Titanium mesh supported TiO2 nanowire arrays/upconversion luminescence Er3+-Yb3+ codoped TiO2 nanoparticles novel composites for flexible dye-sensitized solar cells *Appl. Surf. Sci.* **422** 304–15

[37] Tan H, Santbergen R, Smets A H M and Zeman M 2012 Plasmonic Light Trapping in Thin- film Silicon Solar Cells with Improved Self-Assembled Silver Nanoparticles *Nano Lett.* **12** 4070–6

[38] Tan H, Santbergen R, Yang G, Smets A H M and Zeman M 2014 Combined Optical and Electrical Design of CoDesign of Plasmonic Back Reflector for High-Efficiency Thin-Film Silicon Solar Cells *IEEE J. Photovoltaics* **3** 53–8

[39] Tan H, Sivec L, Yan B, Santbergen R, Zeman M and Smets A H M 2013 Improved light trapping in microcrystalline silicon solar cells by plasmonic back reflector with broad angular scattering and low parasitic absorption *Appl. Phys. Lett.* **102** 153902–5

[40] Atwater H A and Polman A 2010 Plasmonics for improved photovoltaic devices. *Nat. Mater.* **9** 205–13

[41] Sopori B 2005 Thin-film SiliconSolar Cells *Handbook of Photovoltaic Science and Engineering* ed A Luque and S S Hegedus (John Wiley & Sons) pp 307–57

[42] Andreani L C, Bozzola A, Kowalczewski P and Liscidini M 2015 Photonic light trapping and electrical transport in thin-film silicon solar cells *Sol. Energy Mater. Sol. Cells* **135** 78–92

[43] Rech B, Springer J and Vanecek M 2004 TCO and light trapping in silicon thin film solar cells *Sol. Energy* **77** 917–30

[44] Collins R W, Ferlauto A S, Ferreira G M, Chen C, Koh J, Koval R J, Lee Y, Pearce J M and Wronski C R 2003 Evolution of microstructure and phase in amorphous , protocrystalline , and microcrystalline silicon studied by real time spectroscopic ellipsometry *Sol. Energy Mater. Sol. Cells* **78** 143–80

[45] Meillaud F, Boccard M, Bugnon G, Despeisse M, Ha S, Haug F, Stuckelberger M, Ballif C, Persoz J and Schu J 2015 Recent advances and remaining challenges in thin-film silicon photovoltaic technology *Mater. Today* **18** 378–84

[46] Yan B, Yue G, Sivec L, Yang J, Guha S, Yan B, Yue G, Sivec L, Yang J and Guha S 2012 Innovative dual function nc-SiOx:H layer leading to a > 16 % efficient multi- junction thin-film silicon solar cell Innovative dual function nc-SiO x□: H layer leading to a > 16 % efficient multi-junction thin-film silicon solar cell *Appl. Phys. Lett.* **99** 113512–5

[47] Vicente A, Aguas H, Mateus T, Araujo A, Lyubchyk A, Siitonen S, Fortunato E and Martins R 2015 Solar cells for self-sustainable intelligent packaging *J. Mater. Chem. A* **3** 13226–36

[48] Lyubchyk A, Filonovich S A, Mateus T, Mendes M J, Vicente A, Leitão J P, Falcão B P, Fortunato E, Águas H and Martins R 2015 Nanocrystalline thin film silicon solar cells: A deeper look into p/i interface formation *Thin Solid Films* **591** 25–31

[49] Águas H, Mateus T, Vicente A, Gaspar D, Mendes M J, Schmidt W a., Pereira L, Fortunato E and Martins R 2015 Thin Film Silicon Photovoltaic Cells on Paper for Flexible Indoor Applications *Adv. Funct. Mater.* **25** 3592–8

[50] Sai H, Maejima K, Matsui T, Koida T, Kondo M, Nakao S, Takeuchi Y, Katayama H and Yoshida I 2015 High□y efficiency microcrystalline silicon solar cells on honeycomb

textured substrates grown with high rate VHF plasma enhanced chemical vapor deposition *Jpn. J. Appl . Phys.* **54** 08KB05–6

[51] Schropp R E I 2015 Industrialization of Hot Wire Chemical Vapor Deposition for thin fi lm applications *Thin Solid Films* **595** 272–83

[52] Holbert K E and Srinivasan M 2011 Solar Energy Systems *Handbook of renewable energy technology* ed A Zobaa and Ramesh Bansal (Singapore: World Scientific) pp 189–2013

[53] Miller O D, Yablonovitch E and Kurtz S R 2012 Strong Internal and External Luminescence as Solar Cells Approach the Shockley – Queisser Limit **2** 303–11

[54] Aguas H, Ram S K, Araujo A, Gaspar D, Vicente A, Filonovich S A, Fortunato E, Martins R and Ferreira I 2011 Silicon thin film solar cells on commercial tiles *Energy Environ. Sci.* **4** 4620–32

[55] Vicente A, Águas H, Mateus T, Araújo A, Lyubchyk A, Siitonen S, Fortunato E and Martins R 2015 Solar cells for self-sustainable intelligent packaging *J. Mater. Chem. A* **3** 13226–36

[56] Seweryn M., M. J. Mendes, Sergej A. F. T M, Salvatore Mirabella, Hugo Águas, Isabel Ferreira F S and Elvira Fortunato, Rodrigo Martins F P and I C 2014 Broadband photocurrent enhancement in a-Si:H solar cells with plasmonic back reflectors *Opt. Express* **22** 1059–70

[57] Águas H, Mateus T, Vicente A, Gaspar D, Mendes M J, Schmidt W a., Pereira L, Fortunato E and Martins R 2015 Thin Film Silicon Photovoltaic Cells on Paper for Flexible Indoor Applications *Adv. Funct. Mater.* **25** 3592–8

[58] Gonçalves G, Grasso V, Barquinha P, Elamurugu E, Brignone M, Martins R and Lambertini V 2011 Role of Room Temperature Sputtered High Conductive and High Transparent Indium Zinc Oxide Film Contacts on the Performance of Orange , Green , and Blue Organic Light Emitting Diodes *Plasma Process. Polym.* **8** 340–5

[59] Tan H, Santbergen R, Yang G, Smets A H M and Zeman M 2013 Combined Optical and Electrical Design of Plasmonic Back Reflector for High-Efficiency Thin-Film Silicon Solar Cells *IEEE J. Photovoltaics* **3** 53–8

[60] Fortunato E, Raniero L, Silva L, Gonçalves A, Pimentel A, Barquinha P, Águas H, Pereira L, Gonçalves G, Ferreira I, Elangovan E and Martins R 2008 Highly stable transparent and conducting gallium-doped zinc oxide thin films for photovoltaic applications *Sol. Energy Mater. Sol. Cells* **92** 1605–10

[61] Assuncao V, Ferreira I, Martins R, Fortunato E, Marques A and Aguas H 2003 Influence of the deposition pressure on the properties of transparent and conductive ZnO:Ga thin-film produced by r.f. sputtering at room temperature *Thin Solid Films* **427** 401–5

[62] Thompson C V. 2012 Solid-State Dewetting of Thin Films *Annu. Rev. Mater. Res.* **42** 399–434

[63] Vicente A, Águas H, Mateus T, Araújo A, Lyubchyk A, Siitonen S, Fortunato E and Martins R 2015 Solar cells for self-sustainable intelligent packaging *J. Mater. Chem. A* **3** 13226–36

[64] Matsui T, Sai H, Suezaki T, Matsumoto M, Saito K, Yoshida I K M 2013 Development of highly Sstable and efficient amorphous silicon based solar cells *Proc. 28th Eur. Photovolt. Sol. Energy Conf.* 2213–7

[65] Yan X, Venkataraj S and Aberle A G 2013 Modified Surface Texturing of Aluminium-Doped Zinc Oxide (AZO) Transparent Conductive Oxides for Thin-Film Silicon Solar Cells *Energy Procedia* **33** 157–65

[66] Ju S, Gu M, Park S, Hoon J, Chul J, Mok W, Sung J and Kim D 2009 Development of surface-textured hydrogenated ZnO:Al thin-films for lc-Si solar cells *Curr. Appl. Phys.* **9** 1318–22

[67] Palanchoke U, Jovanov V, Kurz H, Dewan R, Magnus P, Stiebig H and Knipp D 2013 Influence of back contact roughness on light trapping and plasmonic losses of randomly textured amorphous silicon thin film solar cells *Sol. Energy* **102** 1–3

[68] Rath J K 2014 Understanding light trapping by light scattering textured back electrodes in thin film n-i-p-type silicon solar cells *J. Appl. Phys.* **102** 014503–7

[69] Haug F, Naqavi A and Ballif C 2013 Diffraction and absorption enhancement from textured back reflectors of thin film solar cells *J. Appl. Phys.* **112** 024516–7

[70] Karin S, Erni L, Ding L, Billet A, Boccard M, Barraud L, Wolf S De, Haug F, Despeisse M and Ballif C 2010 Nanoimprint Lithography for High-Efficiency Thin-Film Silicon Solar Cells *Nano Lett.* **11** 661–5

[71] Mendes M J, Morawiec S, Crupi I, Simone F and Priolo F 2014 Colloidal Self-assembled Nanosphere Arrays for Plasmon-enhanced Light Trapping in Thin Film Silicon Solar Cells *Energy Procedia* **44** 184–91

[72] Araújo A, Mendes M J, Mateus T, Vicente A, Nunes D, Fortunato E, Águas H and Martins R 2016 Influence of the substrate on the morphology of self- assembled Ag nanoparticles by rapid thermal annealing *J. Mater. Chem. C* **120** 18235–42

[73] Temple T L, Mahanama G D K, Reehal H S and Bagnall D M 2009 Influence of localized surface plasmon excitation in silver nanoparticles on the performance of silicon solar cells *Sol. Energy Mater. Sol. Cells* **93** 1978–85

[74] Fleischmann M, Hendra P J and McQuillan A J 1974 Raman Spectra of pyridine adsorbed at a silver electrode *Chem. Phys. Lett.* **26** 2–5

[75] McQuillan A J 2009 The discovery of surface-enhanced Raman scattering *Notes Rec. R. Soc.* **63** 105–9

[76] Jeanmaire D L and Van Duyne R P 1977 Surface Raman Spectroelectrochemistry *J. Electroanal. Chem.* **84** 1–20

[77] Albrecht M G and Creighton J A 1977 Anomalously Intense Raman Spectra of Pyridine at a Silver Electrode *J. Am. Chem. Soc.* **99** 5215–7

[78] Moskovits M 1979 Enhanced Raman scattering by molecules adsorbed on electrodes--a theoretical model *Solid State Commun.* **32** 59–62

[79] Moskovits M 1985 Surface-enhanced spectroscopy *Rev. Mod. Phys.* **57** 783–826

[80] Nie S 1997 Probing Single Molecules and Single Nanoparticles by Surface-Enhanced Raman Scattering *Science (80-.).* **275** 1102–6

[81] Kneipp K, Wang Y, Kneipp H, Perelman L, Itzkan I, Dasari R and Feld M 1997 Single Molecule Detection Using Surface-Enhanced Raman Scattering (SERS) *Phys. Rev. Lett.* **78** 1667–70

[82] Pettinger B, Krischer K and Ertl G 1988 Giant raman scattering cross section for an adsorbed dye at ag colloids associated with low EM field enhancement *Chem. Phys. Lett.* **151** 151–5

[83] Nie S and Emory S R 1997 Probing Single Molecules and Single Nanoparticles by Surface-Enhanced Raman Scattering *Science (80-.).* **275** 1102–6

[84] Moskovits M 2013 Persistent misconceptions regarding SERS *Phys. Chem. Chem. Phys.* **15** 5301

[85] Schlücker S 2011 *Surface Enhanced Raman Spectroscopy* ed S Schlücker (Weinheim: Wiley-VCH Verlag GmbH & Co. KGaA)

[86] R. S. Krishnan and R. K. Shankar 1981 Raman effect: History of the discovery *J. Raman Spectrosc.* **10** 1–8

[87] Schlücker S 2014 Surface-enhanced Raman spectroscopy: concepts and chemical applications. *Angew. Chem. Int. Ed. Engl.* **53** 4756–95

[88] Le Ru E C, Blackie E, Meyer M and Etchegoin P G 2007 Surface Enhanced Raman Scattering Enhancement Factors:☐ A Comprehensive Study *J. Phys. Chem. C* **111** 13794–803

[89] Li Z-Y and Xia Y 2010 Metal nanoparticles with gain toward single-molecule detection by surface-enhanced Raman scattering. *Nano Lett.* **10** 243–9

[90] García-Vidal F J and Pendry J B 1996 Collective Theory for Surface Enhanced Raman Scattering *Phys. Rev. Lett.* **77** 1163–6

[91] Yi Z, Xu X, Luo J, Li X, Yi Y and Jiang X 2014 Size controllable synthesis of ultra fi ne spherical gold particles and their simulation of plasmonic and SERS behaviors *Phys. B Phys. Condens. Matter* **438** 22–8

[92] Araújo A, Caro C, Mendes M J, Nunes D, Fortunato E, Franco R, Águas H and Martins R 2014 Highly efficient nanoplasmonic SERS on cardboard packaging substrates. *Nanotechnology* **25** 415202

[93] Stranahan S M and Willets K A 2010 Super-resolution optical imaging of single-molecule SERS hot spots. *Nano Lett.* **10** 3777–84

[94] Theiss J, Pavaskar P, Echternach P M, Muller R E and Cronin S B 2010 Plasmonic nanoparticle arrays with nanometer separation for high-performance SERS substrates. *Nano Lett.* **10** 2749–54

[95] Wang A X and Kong X 2015 Review of Recent Progress of Plasmonic Materials and Nano-Structures for Surface-Enhanced Raman Scattering. *Materials (Basel).* **8** 3024–52

[96] Otto A, Mrozek I, Grabhorn H and Akemann W 1992 Surface-enhanced Raman scattering *J.Phys.:Condens.Matter* **4** 1143–212

[97] Lecomte S, Matejka P and Baron M H 1998 Correlation between Surface Enhanced Raman Scattering and Absorbance Changes in Silver Colloids . Evidence for the Chemical Enhancement Mechanism *Langmuir* **14** 4373–7

[98] Park W and Kim Z H 2010 Charge Transfer Enhancement in the SERS of a Single Molecule *Nano Lett.* **10** 4040–8

[99] Käll M and Apell P 2000 Electromagnetic contributions to single- molecule sensitivity in surface-enhanced Raman scattering *Phys. Rev. E* **62** 4318–24

[100] Martins R, Ferreira I and Fortunato E 2011 Electronics with and on paper *Phys. status solidi - Rapid Res. Lett.* **5** 332–5

[101] Vicente A T, Araújo A, Gaspar D, Santos L, Marques A C, Mendes M J, Pereira L, Fortunato E and Martins R 2017 Optoelectronics and Bio Devices on Paper Powered by Solar Cells *Nanostructured Solar Cells* (InTech)

[102] Du X, Zhang Z, Liu W and Deng Y 2017 Nanocellulose-based conductive materials and their emerging applications in energy devices - A review *Nano Energy* **35** 299–320

[103] Bledzki A 1999 Composites reinforced with cellulose based fibres *Prog. Polym. Sci.* **24** 221–74

[104] Klemm D, Heublein B, Fink H-P and Bohn A 2005 Cellulose: Fascinating Biopolymer and Sustainable Raw Material *Angew. Chemie Int. Ed.* **44** 3358–93

[105] Zhu M, Li T, Davis C S, Yao Y, Dai J, Wang Y, AlQatari F, Gilman J W and Hu L 2016 Transparent and haze wood composites for highly efficient broadband light management in solar cells *Nano Energy* **26** 332–9

[106] Small A C and Johnston J H 2008 Novel hybrid materials of cellulose fibres and doped ZnS nanocrystals *Curr. Appl. Phys.* **8** 512–5

[107] Li C, Wang F and Yu J C 2011 Semiconductor/biomolecular composites for solar energy applications *Energy Environ. Sci.* **4** 100–13

[108] Moon R J, Martini A, Nairn J, Simonsen J and Youngblood J 2011 Cellulose nanomaterials review: structure, properties and nanocomposites *Chem. Soc. Rev.* **40** 3941

[109] Smith S, Moodley K, Govender U, Chen H, Fourie L, Ngwenya S, Kumar S, Mjwana P, Cele H, Mbanjwa M B, Potgieter S, Joubert T-H and Land K 2015 Paper-based smart microfluidics for education and low-cost diagnostics *S. Afr. J. Sci.* 1–10

[110] Yam K L, Takhistov P T and Miltz J 2005 Intelligent Packaging: Concepts and Applications *J. Food Sci.* **70** 1–10

[111] Robinson A M, Zhao L, Shah Alam M Y, Bhandari P, Harroun S G, Dendukuri D, Blackburn J and Brosseau C L 2015 The development of “fab-chips” as low-cost, sensitive surface-enhanced Raman spectroscopy (SERS) substrates for analytical applications *Analyst* **140** 779–85

[112] Betz J F, Yu W W, Cheng Y, White M and Rubloff G W 2014 Simple SERS substrates: powerful, portable, and full of potential *Phys. Chem. Chem. Phys.* **16** 2224–39

[113] Lee C H, Tian L and Singamaneni S 2010 Paper-Based SERS Swab for Rapid Trace Detection on Real-World Surfaces *ACS Appl. Mater. Interfaces* **2** 3429–3235

[114] Aroca R F 2013 Plasmon enhanced spectroscopy. *Phys. Chem. Chem. Phys.* **15** 5355–63

[115] West P R, Ishii S, Naik G V, Emani N K, Shalaev V M and Boltasseva a. 2010 Searching for better plasmonic materials *Laser Photon. Rev.* **4** 795–808

[116] Rycenga M, Cobley C M, Zeng J, Li W, Moran C H, Zhang Q, Qin D and Xia Y 2011 Controlling the Synthesis and Assembly of Silver Nanostructures for Plasmonic Applications *Chem. Rev.* **111** 3669–712

[117] Araújo A, Pimentel A, Oliveira M J, Mendes M J, Franco R and Fortunato, Elvira, Águas, Hugo, Martins R 2017 Direct growth of plasmonic nanorod forests on paper substrates for low-cost fl exible 3D SERS platforms *Flex. Print. Electron.* **2** 014001

[118] Gaspar D, Fernandes S N, De Oliveira A G, Fernandes J G, Grey P, Pontes R V, Pereira L, Martins R, Godinho M H and Fortunato E 2014 Nanocrystalline cellulose applied simultaneously as the gate dielectric and the substrate in flexible field effect transistors *Nanotechnology* **25** 94008

[119] Kelly K L, Coronado E, Zhao L L and Schatz G C 2003 The optical Properties of Metal Nanoparticles: The Influence of Size, Shape, and Dielectroc Environment *J. Phys. Chem. B* **107** 668–77

[120] Mendes M J, Hernández E, López E, García-Linares P, Ramiro I, Artacho I, Antolín E, Tobías I, Martí A and Luque A 2013 Self-organized colloidal quantum dots and metal nanoparticles for plasmon-enhanced intermediate-band solar cells. *Nanotechnology* **24** 345402–13

[121] Huang Y and Kim D 2014 Covalently capped seed-mediated growth:a unique approach toward hierarchical growth of gold nanocrystals *Nanoscale* **6** 6478–81

[122] Gaspar D, Pimentel A C, Mendes M J, Mateus T, Falcão B P, Leitão J P, Soares J, Araújo A, Vicente A, Filonovich S A, Águas H, Martins R and Ferreira I 2014 Ag and Sn Nanoparticles to Enhance the Near-Infrared Absorbance of a-Si:H Thin Films *Plasmonics* **9** 1015–23

[123] Faÿ S, Steinhauser J, Oliveira N, Vallat-Sauvain E and Ballif C 2007 Opto-electronic properties of rough LP-CVD ZnO:B for use as TCO in thin-film silicon solar cells *Thin Solid Films* **515** 8558–61

[124] Chen J, Huang Y, Kannan P, Zhang L, Lin Z, Zhang J, Chen T and Guo L 2016 Flexible and Adhesive Surface Enhance Raman Scattering Active Tape for Rapid Detection of Pesticide Residues in Fruits and Vegetables *Anal. Chim. Acta* **88** 2149–55

[125] Sinha G, Depero L E and Alessandri I 2011 Recyclable SERS substrates based on Au-coated ZnO nanorods. *ACS Appl. Mater. Interfaces* **3** 2557–63

[126] Ngo Y H, Then W L, Shen W and Garnier G 2013 Gold nanoparticles paper as a SERS bio-diagnostic platform. *J. Colloid Interface Sci.* **409** 59–65

[127] Yu W W and White I M 2010 Inkjet printed surface enhanced Raman spectroscopy array on cellulose paper. *Anal. Chem.* **82** 9626–30

[128] Polavarapu L, Porta A La, Novikov S M, Coronado-Puchau M and Liz-Marzán L M 2014 Pen-on-paper approach toward the design of universal surface enhanced Raman scattering substrates. *Small* **10** 3065–71

[129] Polavarapu L and Liz-Marzán L M 2013 Towards low-cost flexible substrates for nanoplasmonic sensing. *Phys. Chem. Chem. Phys.* **15** 5288–300

[130] Zhang R, Xu B, Liu X, Zhang Y, Xu Y and Chen Q 2012 ChemComm Highly efficient SERS test strips w *Chem. Commun.* **48** 5913–5

[131] Wu W, Liu L, Dai Z, Liu J, Yang S, Zhou L and Xiao X 2015 Low-Cost , Disposable , Flexible and Highly Reproducible Screen Printed SERS Substrates for the Detection of Various Chemicals *Sci. Rep.* **5** 1–10

[132] Kumar G V P 2012 Plasmonic nano-architectures for surface enhanced Raman scattering:a review *J. Nanophotonics* **6** 064503

[133] Martín A, Wang J J and Iacopino D 2014 Flexible SERS active Substrates from Ordered Vertical Au *RSC Adv.* **4** 20038–43

[134] Pietrobon B, McEachran M and Vladimir K 2009 Synthesis of Size-Controlled Faceted Pentagonal Silver Nanorods with Tunable Plasmonic Properties and Self-Assembly of These Nanorods *ASC NANO* **3** 21–6

[135] Zheng G, Polavarapu L, Liz-marza L M, Pastoriza-Santos I and Pérez-Juste J 2015 Gold Nanoparticle-loaded Filter paper : A Recyclable “ Dip-Catalyst ” for Real-Time Reaction Monitoring by Surface Enhanced Raman Scaterring *Chem. Commun.* **51** 4572–5

[136] Aksu S, Huang M, Artar A, Yanik A A, Selvarasah S, Dokmeci M R and Altug H 2011 Flexible Plasmonics on Unconventional and Nonplanar Substrates *Adv. Mater.* **23** 4422–30

[137] Osberg K D, Rycenga M, Bourret G R, Brown K A and Mirkin C A 2012 Dispersible Surface-Enhanced Raman Scattering Nanosheets *Adv. Funct. Mater.* **24** 6065–70

[138] Fan M, Andrade G F S and Brolo A G 2011 A review on the fabrication of substrates for surface enhanced Raman spectroscopy and their applications in analytical chemistry *Anal. Chim. Acta* **693** 7–25

[139] Prakash J, Harris R A and Swart H C 2016 Embedded plasmonic nanostructures: synthesis, fundamental aspects and their surface enhanced Raman scattering applications *Int. Rev. Phys. Chem.* **35** 353–98

[140] Zhao W and van der Berg A 2008 Lab on paper *Lab Chip* **8** 1988–91

[141] Kim W-S, Shin J-H, Park H-K and Choi S 2015 A low-cost, monometallic, surface-enhanced Raman scattering-functionalized paper platform for spot-on bioassays *Sensors Actuators B Chem.* **222** 1112–8

[142] Ngo Y H, Li D, Simon G P and Garnier G 2012 Gold nanoparticle-paper as a three-dimensional surface enhanced Raman scattering substrate. *Langmuir* **28** 8782–90

[143] Lee C H, Hankus M E, Tian L, Pellegrino P M and Singamaneni S 2011 Highly Sensitive Surface Enhanced Raman Scattering Substrates *Anal. Chem.* **83** 8953–8

[144] Chung A J, Huh Y S and Erickson D 2011 Large area flexible SERS active substrates using engineered nanostructures. *Nanoscale* **3** 2903–8

[145] Fierro-Mercado P M and Hernández-Rivera S P 2012 Highly Sensitive Filter Paper Substrate for SERS Trace Explosives Detection *Int. J. Spectrosc.* **2012** 1–7

[146] Qu L-L, Li D-W, Xue J-Q, Zhai W-L, Fossey J S and Yi-Tao Long 2012 Batch fabrication of disposable sreen printed SERS arrays *Lab Chip* **12** 876–81

[147] Cha R, Wang D, He Z and Ni Y 2012 Development of cellulose paper testing strips for quick measurement of glucose using chromogen agent *Carbohydr. Polym.* **88** 1414–9

[148] Veigas B, Jacob J M, Costa M N, Santos D S, Viveiros M, Inácio J, Martins R, Barquinha P, Fortunato E and Baptista P V 2012 Gold on paper-paper platform for Au-nanoprobe TB detection. *Lab Chip* **12** 4802–8

[149] Costa M N, Veigas B, Jacob J M, Santos D S, Gomes J, Baptista P V, Martins R, Inácio J and Fortunato E 2014 A low cost, safe, disposable, rapid and self-sustainable paper-based platform for diagnostic testing: lab-on-paper. *Nanotechnology* **25** 094006

[150] Sun Y and Rogers J a. 2007 Inorganic Semiconductors for Flexible Electronics *Adv. Mater.* **19** 1897–916

[151] Tobjork D and Osterbacka R 2011 Paper Electronics *Adv. Mater.* **23** 1935–61

[152] Robinson A M, Harroun S G, Bergman J and Brosseau C L 2012 Portable Electrochemical Surface-Enhanced Raman Spectroscopy System for Routine Spectroelectrochemical Analysis *Anal. Chem.* **84** 1760–4

[153] Hoppmann E P, Yu W W and White I M 2013 Highly sensitive and flexible inkjet printed SERS sensors on paper *Methods* **63** 219–24

[154] Yu W W and White I M 2013 Inkjet-printed paper-based SERS dipsticks and swabs for trace chemical detection *Analyst* **138** 1020–5

[155] Wu D and Fang Y 2003 The adsorption behavior of p-hydroxybenzoic acid on a silver-coated filter paper by surface enhanced Raman scattering *J. Colloid Interface Sci.* **265** 234–8

[156] Oliveira M J, Quaresma P and Almeida M P 2017 Office paper decorated with silver nanostars - an alternative cost effective platform for trace analyte detection by SERS *Sci. Rep.* **7** 1–14

[157] Yu W W and White I M 2012 A simple filter-based approach to surface enhanced Raman spectroscopy for trace chemical detection *Analyst* **137** 1168

[158] Sallum L F, Soares F L F, Ardila J A and Carneiro R L 2014 Optimization of SERS scattering by Ag-NPs-coated filter paper for quantification of nicotinamide in a cosmetic formulation *Talanta* **118** 353–8

[159] Berthod A, Laserna J J and Winefordner J D 1988 Analysis by surface enhanced Raman spectroscopy on silver hydrosols and silver coated filter papers *J. Pharm. Biomed. Anal.* **6** 599–608

[160] Cheng M L, Tsai B C and Yang J 2011 Silver nanoparticle-treated filter paper as a highly sensitive surface-enhanced Raman scattering (SERS) substrate for detection of tyrosine in aqueous solution *Anal. Chim. Acta* **708** 89–96

[161] Sallum L F, Soares F L F, Ardila J A and Carneiro R L 2014 Determination of acetylsalicylic acid in commercial tablets by SERS using silver nanoparticle-coated filter paper. *Spectrochim. Acta. A. Mol. Biomol. Spectrosc.* **133** 107–11

[162] Wu M, Su W, Han H and Chen L 2012 Eco-Friendly Plasmonic Sensors: Using the Photothermal Effect to Prepare Metal Nanoparticle-Containing Test Papers for Highly Sensitive Colorimetric Detection *Anal. Chem.* **84** 5140–5

[163] Polavarapu L and Liz-Marzán L M 2013 Towards low-cost flexible substrates for nanoplasmonic sensing. *Phys. Chem. Chem. Phys.* **15** 5288–300

[164] Castro K, Princi E, Proietti N, Manso M, Capitani D, Vicini S, Madariaga J M and De Carvalho M L 2011 Assessment of the weathering effects on cellulose based materials through a multianalytical approach *Nucl. Instruments Methods Phys. Res. Sect. B Beam Interact. with Mater. Atoms* **269** 1401–10

[165] Li Y, Zhang K, Zhao J, Ji J, Ji C and Liu B 2016 A three-dimensional silver nanoparticles decorated plasmonic paper strip for SERS detection of low-abundance molecules *Talanta* **147** 493–500

[166] Zhu Y, Zhang L and Yang L 2015 Designing of the functional paper-based surface-enhanced Raman spectroscopy substrates for colorants detection *Mater. Res. Bull.* **63** 199–204

[167] Cao W and Elsayed-Ali H E 2009 Stability of Ag nanoparticles fabricated by electron beam lithography *Mater. Lett.* **63** 2263–6

[168] Mohiddon M A, Sangani L D V and Krishna M G 2013 Scanning near field optical microscopy of gold nano-disc arrays fabricated by electron beam lithography and their application as surface enhanced Raman scattering substrates *Chem. Phys. Lett.* **588** 160–6

[169] Sánchez-Iglesias A, Aldeanueva-Potel P, Ni W, Pérez-Juste J, Pastoriza-Santos I, Alvarez-Puebla R A, Mbenkum B N and Liz-Marzán L M 2010 Chemical seeded growth of Ag nanoparticle arrays and their application as reproducible SERS substrates *Nano Today* **5** 21–7

[170] Hu J, Wang Z and Li J 2007 Gold Nanoparticles With Special Shapes: Controlled Synthesis, Surface-enhanced Raman Scattering, and The Application in Biodetection *Sensors* 7 3299–311

[171] Gaspar D, Pimentel A C, Mateus T, Leitão J P, Soares J, Falcão B P, Araújo A, Vicente A, Filonovich S a, Aguas H, Martins R and Ferreira I 2013 Influence of the layer thickness in plasmonic gold nanoparticles produced by thermal evaporation. *Sci. Rep.* **3** 1469–73

[172] Araújo A, Mendes M J, Mateus T, Nunes D, Calmeiro T, Fortunato E, Hugo A and Martins R 2016 Influence of the Substrate on the Morphology of Self-Assembled Silver Nanoparticles by Rapid Thermal Annealing *J. Phys. Chem. C* **120** 18235–42

[173] Araújo A, Caro C, Mendes M J and Nunes D 2014 Highly efficient nanoplasmonic SERS on cardboard packaging substrates *Nanotechnology* **25** 415202

[174] Mendes M J, Morawiec S, Mateus T, Lyubchyk A, Águas H, Ferreira I, Fortunato E, Martins R, Priolo F and Crupi I 2015 Broadband light trapping in thin film solar cells with self-organized plasmonic nano-colloids. *Nanotechnology* **26** 135202–10

[175] Thouti E, Chander N, Dutta V and Komarala V K 2013 Optical properties of Ag nanoparticle layers deposited on silicon substrates *J. Opt.* **15** 035005–11

[176] Nasser H, Saleh Z M, Özkol E, Günoven M, Bek A and Turan R 2013 Fabrication of Ag Nanoparticles Embedded in Al:ZnO as Potential Light-Trapping Plasmonic Interface for Thin Film Solar Cells *Plasmonics* **8** 1485–92

[177] Sun H, Yu M, Wang G, Sun X and Lian J 2012 Temperature-Dependent Morphology Evolution and Surface Plasmon Absorption of Ultrathin Gold Island Films *J. Phys. Chem. C* **116** 9000–8

[178] Abràmoff M D, Hospitals I, Magalhães P J and Abràmoff M 2004 Image Processing with ImageJ *Biophotonics* **11** 36–42

[179] Pereira L, Fortunato E Ã, Raniero L, Silva L, Gonc A, Pimentel A, Barquinha P, Gonc G, Ferreira I, Elangovan E and Martins R 2008 Highly stable transparent and conducting gallium-doped zinc oxide thin films for photovoltaic applications *Sol. Energy Mater. Sol. Cells* **92** 1605–10

[180] Gaspar D, Pereira L, Gehrke K, Galler B, Fortunato E and Martins R 2017 High mobility hydrogenated zinc oxide thin fi lms *Sol. Energy Mater. Sol. Cells* **163** 255–62

[181] Tao Q, Li S, Ma C, Liu K, Zhang Q-Y, Zhu D B, Fan H J, Yu H Y and Fan H J 2015 A highly sensitive and recyclable SERS substrate based on Ag-nanoparticle-decorated ZnO nanoflowers in ordered arrays *Dalt. Trans.* **44** 3447–53

[182] Lamberti A, Virga A, Chiadò A, Chiodoni A, Bejtka K, Rivolo P and Giorgis F 2015 Ultrasensitive Ag-coated TiO 2 nanotube arrays for flexible SERS-based optofluidic devices *J. Mater. Chem. C* **3** 6868–75

[183] Shaik U P, Hamad S, Ahamad Mohiddon M, Soma V R and Ghanashyam Krishna M 2016 Morphologically manipulated Ag/ZnO nanostructures as surface enhanced Raman scattering probes for explosives detection *J. Appl. Phys.* **119** 093103

[184] Santbergen R, Temple T L, Liang R, Smets a H M, Swaaij R a C M M Van and Zeman M 2012 Application of plasmonic silver island films in thin-film silicon solar cells *J. Opt.* **14** 024010–9

[185] Araújo A, Barros R, Mateus T, Gaspar D, Neves N, Vicente A, Filonovich S a, Barquinha P, Fortunato E, Ferraria A M, Botelho do Rego A M, Bicho A, Águas H and Martins R 2013 Role of a disperse carbon interlayer on the performances of tandem a-Si solar cells *Sci. Technol. Adv. Mater.* **14** 045009–17

[186] Wilken K, Smirnov V, Astakhov O and Finger F 2014 Thin-film silicon solar cells fabricated at low temperature: A versatile technology for application on transparent flexible plastic substrates and in integrated photoelectrochemical water splitting modules *2014 IEEE 40th Photovoltaic Specialist Conference (PVSC)* (IEEE) pp 3051–4

[187] Bai Y, Gao Z, Chen N, Liu H, Yao J, Ma S and Shi X 2014 Applied Surface Science Elimination of small-sized Ag nanoparticles via rapid thermal annealing for high efficiency light trapping structure *Appl. Surf. Sci.* **315** 1–7

[188] Hsieh J H, Li C, Wu Y Y and Jang S C 2011 Optical studies on sputter-deposited Ag–SiO2 nanoparticle composites *Thin Solid Films* **519** 7124–8

[189] Bai Y, Gao Z, Chen N, Liu H, Yao J, Ma S and Shi X 2014 Elimination of small-sized Ag nanoparticles via rapid thermal annealing for high efficiency light trapping structure *Appl. Surf. Sci.* **315** 1–7

[190] Sesuraj R S A, Temple T L and Bagnall D M 2013 Solar Energy Materials & Solar Cells Optical characterisation of a spectrally tunable plasmonic reflector for application in thin-film silicon solar cells *Sol. Energy Mater. Sol. Cells* **111** 23–30

[191] Mahan G D and Bartkowiak M 1999 Wiedemann–Franz law at boundaries *Appl. Phys. Lett.* **74** 953

[192] Bechelany M, Maeder X, Riesterer J, Hankache J, Lerose D, Christiansen S, Michler J and Philippe L 2010 Synthesis Mechanisms of Organized Gold Nanoparticles: Influence of Annealing Temperature and Atmosphere *Cryst. Growth Des.* **10** 587–96

[193] Kwon J-Y, Yoon T-S, Kim K-B and Min S-H 2003 Comparison of the agglomeration behavior of Au and Cu films sputter deposited on silicon dioxide *J. Appl. Phys.* **93** 3270–8

[194] Karapanagiotis I, Evans D F and Gerberich W W 2002 Dewetting dynamics of thin polystyrene films from sputtered silicon and gold surfaces *Colloids Surfaces A Physicochem. Eng. Asp.* **207** 59–67

[195] Henley S J, Carey J D and Silva S R P 2005 Pulsed-laser-induced nanoscale island formation in thin metal-on-oxide films *Phys. Rev. B* **72** 195408

[196] Choi H, Gong J, Lim Y, Im K H and Jeon M 2013 Effects of the electrical conductivity and orientation of silicon substrate on the synthesis of multi-walled carbon nanotubes by thermal chemical vapor deposition. *Nanoscale Res. Lett.* **8** 110

[197] Lyubchyk A, Vicente A, Alves P U, Catela B, Soule B, Mateus T, Mendes M J, Águas H, Fortunato E and Martins R 2016 Influence of post-deposition annealing on electrical and optical properties of ZnO-based TCOs deposited at room temperature *Phys. status solidi* **213** 2317–28

[198] Morawiec S, Holovský J, Mendes M J, Müller M, Ganzerová K, Vetushka A, Ledinský M, Priolo F, Fejfar A and Crupi I 2016 Experimental quantification of useful and parasitic absorption of light in plasmon-enhanced thin silicon films for solar cells application *Sci. Rep.* **6** 1–10

[199] Temple T L and Bagnall D M 2011 Optical properties of gold and aluminium nanoparticles for silicon solar cell applications *J. Appl. Phys.* **109** 084343

[200] Söderström T, Haug F-J, Terrazzoni-Daudrix V and Ballif C 2008 Optimization of amorphous silicon thin film solar cells for flexible photovoltaics *J. Appl. Phys.* **103** 114509

[201] Haes A J, Zou S, Zhao J, Schatz G C and Van Duyne R P 2006 Localized surface plasmon resonance spectroscopy near molecular resonances. *J. Am. Chem. Soc.* **128** 10905–14

[202] Robinson J W, Frame E M S and Frame II G M 2014 *A Practical Guide to Geometric Regulation for Distributed Parameter Systems* (New York: CRC Press, Taylor & Francis Group)

[203] Moskovits M 1978 Surface roughness and the enhanced intensity of Raman scattering by molecules adsorbed on metals *J. Chem. Phys.* **69** 4159–61

[204] Pallaoro A, Hoonejani M R, Braun G B, Meinhart C D and Moskovits M 2015 Rapid Identification by Surface-Enhanced Raman Spectroscopy of Cancer Cells at Low Concentrations Flowing in a Microfluidic Channel *ACS Nano* **9** 4328–36

[205] Kline N D, Tripathi A, Mirsafavi R, Pardoe I, Moskovits M, Meinhart C, Guicheteau J A, Christesen S D and Fountain A W 2016 Optimization of Surface-Enhanced Raman Spectroscopy Conditions for Implementation into a Microfluidic Device for Drug Detection *Anal. Chem.* **88** 10513–22

[206] Zaderenko P, Caro C and Carlos L 2008 Thiol-immobilized silver nanoparticle aggregate films for surface enhanced Raman scattering *J. Raman Spectrosc.* **39** 1162–9

[207] Merlen a, Gadenne V, Romann J, Chevallier V, Patrone L and Valmalette J C 2009 Surface enhanced Raman spectroscopy of organic molecules deposited on gold sputtered substrates. *Nanotechnology* **20** 215705

[208] Zhang R, Xu B-B, Liu X-Q, Zhang Y-L, Xu Y, Chen Q-D and Sun H-B 2012 Highly efficient SERS test strips. *Chem. Commun.* **48** 5913–5

[209] Costa M N, Veigas B, Jacob J M, Santos D S, Gomes J, Baptista P V, Martins R, Inácio J and Fortunato E 2014 A low cost, safe, disposable, rapid and self-sustainable paper-based platform for diagnostic testing: lab-on-paper. *Nanotechnology* **25** 094006

[210] Tobjörk D and Österbacka R 2011 Paper electronics. *Adv. Mater.* **23** 1935–61

[211] Li W, Guo Y and Zhang P 2010 SERS-active silver nanoparticles prepared by a simple and green method *J. Phys. Chem. C* **114** 6413–7

[212] Cho W J, Kim Y and Kim J K 2012 Ultrahigh-Density Array of Silver Nanoclusters for SERS Substrate with High Sensitivity and Excellent Reproducibility *ASC NANO* **6** 249–55

[213] Wang X, Li M, Meng L, Lin K, Feng J, Huang T, Yang Z and Ren B 2014 Probing the location of hot spots by surface-enhanced Raman spectroscopy: toward uniform substrates. *ACS Nano* **8** 528–36

[214] Nakayama K, Tanabe K and Atwater H A 2008 Plasmonic nanoparticle enhanced light absorption in GaAs solar cells *Appl. Phys. Lett.* **93** 121904–12196

[215] Wurtz G A, Evans P R, Hendren W, Atkinson R, Dickson W, Pollard R J, Zayats A V, Harrison W and Bower C 2007 Molecular plasmonics with tunable exciton-plasmon coupling strength in J-aggregate hybridized Au nanorod assemblies. *Nano Lett.* **7** 1297–303

[216] Zhao J, Dieringer J A, Zhang X, Schatz G C and Duyne R P Van 2008 Resonance Raman Excitation Spectroscopy Wavelength-Scanned Surface-Enhanced Resonance Raman Excitation Spectroscopy *J. Phys. Chem. C* **112** 19302–10

[217] Zhao J, Jensen L, Sung J, Zou S, Schatz G C and Duyne R P Van 2007 Interaction of plasmon and molecular resonances for rhodamine 6G adsorbed on silver nanoparticles. *J. Am. Chem. Soc.* **129** 7647–56

[218] Frontiera R R, Henry A-I, Gruenke N L and Van Duyne R P 2011 Surface-Enhanced Femtosecond Stimulated Raman Spectroscopy *J. Phys. Chem. Lett.* **2** 1199–203

[219] Tyler T P, Henry A-I, Van Duyne R P and Hersam M C 2011 Improved Monodispersity of Plasmonic Nanoantennas via Centrifugal Processing *J. Phys. Chem. Lett.* **2** 218–22

[220] Sharma B, Fernanda Cardinal M, Kleinman S L, Greeneltch N G, Frontiera R R, Blaber M G, Schatz G C and Van Duyne R P 2013 High-performance SERS substrates: Advances and challenges *MRS Bull.* **38** 615–24

[221] Shah J and Brown R M 2005 Towards electronic paper displays made from microbial cellulose. *Appl. Microbiol. Biotechnol.* **66** 352–5

[222] Gaspar D, Fernandes S N, de Oliveira a G, Fernandes J G, Grey P, Pontes R V, Pereira L, Martins R, Godinho M H and Fortunato E 2014 Nanocrystalline cellulose applied simultaneously as the gate dielectric and the substrate in flexible field effect transistors. *Nanotechnology* **25** 094008

[223] Nyholm L, Nyström G, Mihranyan A and Strømme M 2011 Toward flexible polymer and paper-based energy storage devices. *Adv. Mater.* **23** 3751–69

[224] Pimentel A, Nunes D, Duarte P, Rodrigues J, Costa F M, Monteiro T, Martins R and Fortunato E 2014 Synthesis of Long ZnO Nanorods under Microwave Irradiation or Conventional Heating *J. Phys. Chem. C* **118** 14629–39

[225] Marques a C, Santos L, Costa M N, Dantas J M, Duarte P, Gonçalves a, Martins R, Salgueiro C a and Fortunato E 2015 Office paper platform for bioelectrochromic detection of electrochemically active bacteria using tungsten trioxide nanoprobes. *Sci. Rep.* **5** 9910

[226] Fierro-mercado P M and Hern S P 2012 Highly Sensitive Filter Paper Substrate for SERS Trace Explosives Detection *Int. J. Spectrosc.*

[227] Kim K-H, Lee K Y, Seo J-S, Kumar B and Kim S-W 2011 Paper-based piezoelectric nanogenerators with high thermal stability. *Small* **7** 2577–80

[228] Kumar A, Gullapalli H, Balakrishnan K, Botello-Mendez A, Vajtai R, Terrones M and Ajayan P M 2011 Flexible ZnO-cellulose nanocomposite for multisource energy conversion. *Small* **7** 2173–8

[229] Ogata K, Koike K, Sasa S, Inoue M and Yano M 2013 ZnO nanorod growth from aqueous solution via microwave heating on paper substrates *Phys. Status Solidi* **10** 1314–6

[230] Qiu Y, Zhang H, Hu L, Yang D, Wang L, Wang B, Ji J, Liu G, Liu X, Lin J, Li F and Han S 2012 Flexible piezoelectric nanogenerators based on ZnO nanorods grown on common paper substrates. *Nanoscale* **4** 6568–73

[231] Gullapalli H, Vemuru V S M, Kumar A, Botello-Mendez A, Vajtai R, Terrones M, Nagarajaiah S and Ajayan P M 2010 Flexible piezoelectric ZnO-paper nanocomposite strain sensor. *Small* **6** 1641–6

[232] Cullity B D 1956 *Elements of X Ray Diffraction* vol 22

[233] Macias-Montero M, Peláez R J, Rico V J, Saghi Z, Midgley P, Afonso C N, González-Elipe A R and Borras A 2015 Laser treatment of Ag@ZnO nanorods as long-life-span SERS surfaces. *ACS Appl. Mater. Interfaces* **7** 2331–9

[234] Tao Q, Li S, Ma C, Liu K and Zhang Q-Y 2015 A highly sensitive and recyclable SERS substrate based on Ag-nanoparticle-decorated ZnO nanoflowers in ordered arrays. *Dalton Trans.* **44** 3447–53

[235] Su L, Qin N, Xie W, Fu J and Bao D 2014 The surface-plasmon-resonance and band bending effects on the photoluminescence enhancement of Ag-decorated ZnO nanorods *J. Appl. Phys.* **116** 063108

[236] Yang L, Ruan W, Jiang X, Zhao B, Xu W and Lombardi J R 2009 Contribution of ZnO to Charge-Transfer Induced Surface-Enhanced Raman Scattering in Au/ZnO/PATP Assembly *J. Phys. Chem. C* **113** 117–20

[237] Zhang M-L, Fan X, Zhou H-W, Shao M-W, Zapien J A, Wong N-B and Lee S-T 2010 A High-Efficiency Surface-Enhanced Raman Scattering Substrate Based on Silicon Nanowires Array Decorated with Silver Nanoparticles *J. Phys. Chem. C* **114** 1969–75

[238] Pimentel A, Ferreira S, Nunes D, Calmeiro T, Martins R and Fortunato E 2016 Microwave Synthesized ZnO Nanorods Arrays for UV Sensors : a Seed Layer Annealing Temperature Study *Materials (Basel).* **9** 1–15

[239] Pimentel a., Rodrigues J, Duarte P, Nunes D, Costa F M, Monteiro T, Martins R and Fortunato E 2015 Effect of solvents on ZnO nanostructures synthesized by solvothermal

method assisted by microwave radiation: a photocatalytic study *J. Mater. Sci.* **50** 5777–87

[240] Jayram N D, Sonia S, Poongodi S, Kumar P S, Masuda Y, Mangalaraj D, Ponpandian N and Viswanathan C 2015 Superhydrophobic Ag decorated ZnO nanostructured thin film as effective surface enhanced Raman scattering substrates *Appl. Surf. Sci.* **355** 969–77

[241] Xu F, Zhang Y, Sun Y, Shi Y, Wen Z and Li Z 2011 Silver Nanoparticles Coated Zinc Oxide Nanorods Array as Superhydrophobic Substrate for the Amplified SERS Effect *J. Phys. Chem. C* **115** 9977–83

[242] Baruah S and Dutta J 2016 Hydrothermal growth of ZnO nanostructures *Sci. Technol. Adv. Mater.* **10** 013001

[243] Vivekanandhan S, Christensen L, Misra M and Mohanty A K 2012 Green Process for Impregnation of Silver Nanoparticles into Microcrystalline Cellulose and Their Antimicrobial Bionanocomposite Films **2012** 371–6

[244] Hadis Morkoç Ü Ö 2009 *Zinc Oxide: Fundamentals, Materials and Device Technology*

[245] Ghayour H, Rezaie H R, Mirdamadi S and Nourbakhsh a. a. 2011 The effect of seed layer thickness on alignment and morphology of ZnO nanorods *Vacuum* **86** 101–5

[246] Kim K H, Utashiro K, Abe Y and Kawamura M 2014 Growth of Zinc Oxide Nanorods Using Various Seed Layer Annealing Temperatures and Substrate Materials **9** 2080–9

[247] Kar S, Dev A and Chaudhuri S 2010 Simple Solvothermal Route To Synthesize ZnO Nanosheets , Nanonails , and Well-Aligned Nanorod Arrays **110** 17848–53

[248] Liu B and Zeng H C 2003 Hydrothermal synthesis of ZnO nanorods in the diameter regime of 50 nm. *J. Am. Chem. Soc.* **125** 4430–1

[249] Attanayake T, Premaratne M and Agrawal G P 2015 Characterizing the Optical Response of Symmetric Hemispherical Nano-dimers *Plasmonics* **10** 1453–66

[250] Le Ru E C, Etchegoin P G and Meyer M 2006 Enhancement factor distribution around a single surface-enhanced Raman scattering hot spot and its relation to single molecule detection. *J. Chem. Phys.* **125** 204701

[251] Tang H, Meng G, Huang Q, Zhang Z, Huang Z and Zhu C 2012 Arrays of Cone-Shaped ZnO Nanorods Decorated with Ag Nanoparticles as 3D Surface-Enhanced Raman Scattering Substrates for Rapid Detection of Trace Polychlorinated Biphenyls *Adv. Funct. Mater.* **22** 218–24

[252] Wang L, Kang Y, Liu X, Zhang S, Huang W and Wang S 2012 ZnO nanorod gas sensor for ethanol detection *Sensors Actuators B Chem.* **162** 237–43

[253] Wei H, Hao F, Huang Y, Wang W and Nordlander P 2008 Polarization Dependence of Surface-Enhanced Raman Scattering in Gold Nanoparticle - Nanowire Systems 2008 **8** 2497–502

[254] Hen Z H E S, Ei L S U, Hen Y A O C S, Science M, Mary Q and London E 2016 Vertically-oriented nanoparticle dimer based on focused plasmonic trapping **24** 357–66

[255] Zhao X, Zhang B, Ai K, Zhang G, Cao L, Liu X, Sun H, Wang H and Lu L 2009 Monitoring catalytic degradation of dye molecules on silver-coated ZnO nanowire arrays by surface-enhanced Raman spectroscopy *J. Mater. Chem.* **19** 5547

[256] Polsongkram D, Chamninok P, Pukird S, Chow L, Lupan O, Chai G, Khallaf H, Park S and Schulte A 2008 Effect of synthesis conditions on the growth of ZnO nanorods via hydrothermal method *Phys. B Condens. Matter* **403** 3713–7

[257] Hayes B L 2002 *Microwave synthesis: chemistry at the speed of light* (CEM Publishing)

[258] Guo M, Diao P, Wang X and Cai S 2005 The effect of hydrothermal growth temperature on preparation and photoelectrochemical performance of ZnO nanorod array films *J. Solid State Chem.* **178** 3210–5

[259] Li W-J, Shi E-W, Zhong W-Z and Yin Z-W 1999 Growth mechanism and growth habit of oxide crystals *J. Cryst. Growth* **203** 186–96

[260] Tong Y, Liu Y, Dong L, Zhao D, Zhang J, Lu Y, Shen D and Fan X 2006 Growth of ZnO nanostructures with different morphologies by using hydrothermal technique. *J. Phys. Chem. B* **110** 20263–7

[261] Morkoc H and Ozgur Ü 2009 Zinc Oxide: Fundamentals, Materials and Device Technology *Wiley* 488

[262] Malevu T D and Ocaya R O 2015 Effect of Annealing Temperature on Structural, Morphology and Optical Properties of ZnO Nano-Needles Prepared by Zinc- Air Cell System Method *Int. J. Electrochem. Sci* **10** 1752–61

[263] Pankove J I 1971 *Optical Processes in Semiconductors* (New Jersey: Dover Publications, Inc.)

[264] Prathap P, Revathi N, Venkata Subbaiah Y P and Ramakrishna Reddy K T 2008 Thickness effect on the microstructure, morphology and optoelectronic properties of ZnS films *J. Phys. Condens. Matter* **20** 035205

[265] Mendes M J, Morawiec S, Crupi I, Simone F and Priolo F 2014 Colloidal self-assembled nanosphere arrays for plasmon-enhanced light trapping in thin film silicon solar cells *Energy Procedia* **44** 184–91

[266] Sanchez-Sobrado O, Mendes M J, Haque S, Mateus T, Araujo A, Aguas H, Fortunato E and Martins R 2017 Colloidal-lithographed TiO2 photonic nanostructures for solar cell light trapping *J. Mater. Chem. C* **5** 6852–61

[267] Mendes M J, Araújo A, Vicente A, Águas H, Ferreira I, Fortunato E and Martins R 2016 Design of optimized wave-optical spheroidal nanostructures for photonic-enhanced solar cells *Nano Energy* **26** 286–96